

Image Analysis for Guidance in Minimally Invasive Liver Interventions

Beeldanalyse voor beeldgeleiding bij minimaal invasieve lever
interventies

Thesis

to obtain the degree of Doctor from the
Erasmus University Rotterdam
by command of the
Rector Magnificus

Prof.dr. H.A.P. Pols

and in accordance with the decision of the Doctorate Board.

The public defense shall be held on
Wednesday, May 17, 2017 at 09:30 hours

by

Luu Manh Ha
born in Hanoi, Vietnam

Doctoral committee

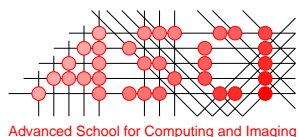
Supervisor:	Prof.dr. W.J. Niessen
Other members:	Prof.dr. B.J.M. Heijmen Prof.dr. J.P.W. Pluim Prof.dr. O.M. van Delden
Cosupervisors:	Dr.ir. T. van Walsum Dr. A. Moelker

Image Analysis for Guidance in Minimally Invasive Liver Interventions

Luu Manh Ha

Colophon

This book was typeset by the author using $\text{\LaTeX}2_{\epsilon}$. The main body of the text was set using a 10-points Computer Modern Roman font. All graphics and images were included formatted as Encapsulated PostScript (TMAdobe Systems Incorporated).



The research described in this thesis was carried out at the Erasmus MC – University Medical Center Rotterdam (Rotterdam, the Netherlands), under the auspices of the Advanced School for Computing and Imaging (ASCI): dissertation series number 369.

This research is supported by the Vietnamese Ministry of Education and Training (MOET), and partly funded by Information Technology for European Advancement (ITEA) (project Benefit, number 13031).

Financial support for publication of this thesis was kindly provided by the Department of Radiology of Erasmus MC University Medical Center Rotterdam, and the ASCI graduate school.

Copyright © 2017 by Luu Manh Ha. All rights reserved. No part of this publication may be reproduced or transmitted in any form or by any means, electronic or mechanical, including photocopy, recording, or any information storage and retrieval system, without permission in writing from the author.

ISBN: 978-94-6332-176-1

Printed by GVO Drukkers en Vormgevers BV.

Contents

Colophon	iv
1 Introduction	1
1.1 The liver and liver cancer	1
1.2 Liver cancer imaging	2
1.3 Liver cancer treatments	5
1.4 Purpose and contents of this thesis	7
2 Quantitative evaluation of noise reduction and vesselness filters	9
2.1 Introduction	10
2.2 Methods	11
2.3 Experiments and Results	18
2.4 Discussion	24
2.5 Conclusion	27
3 Non-rigid registration of liver CT images for CT-guided ablation of liver tumors	31
3.1 Introduction	32
3.2 Method	34
3.3 Experiments and Results	37
3.4 Discussion	42
3.5 Conclusion	46
4 Semi-automated registration of pre- and intra-operative liver CT for image-guided interventions	47
4.1 Introduction	48
4.2 Method	48
4.3 Experiment and results	50
4.4 Discussion and conclusion	52
5 Quantification of non-rigid liver deformation	55
5.1 Introduction	56
5.2 Method	57
5.3 Experiments and results	61
5.4 Discussion	64
5.5 Conclusion	67

6	An automatic registration method for pre- and post-interventional CT images for assessing treatment success in liver RFA treatment	69
6.1	Introduction	70
6.2	Methods	71
6.3	Experiments and results	75
6.4	Discussion	82
6.5	Conclusion	83
7	Summary and Future Perspectives	85
7.1	Summary	85
7.2	Future Perspectives	86
	Bibliography	89
	Samenvatting en toekomstperspectief	99
	PhD Portfolio	103
	Publications	105
	Acknowledgments	107
	Curriculum Vitae	109

General introduction

1.1 The liver and liver cancer

The liver is the largest internal organ of the human body, weighs about 1.5 kg and is located in the upper-right side of the abdomen covered by the rib cage. The liver anatomy is typically divided into two main sections, the right and the left lobe, or into eight segments according to the Couinaud classification system [1] (see Fig 1.1). In contrast to others organ, the liver has two types of veins: the portal vein and the hepatic vein [2,3]. The hepatic artery provides 30% of the total liver blood flow, while 70% comes from the portal vein [2–4]. The main task of the liver is to filter the blood coming from the digestive system via the portal vein, before passing it to the rest of the body. In addition, together with the gallbladder, the pancreas and intestines, the liver is involved in digesting and processing food in the digestive system. The liver also has other functions such as producing proteins that regulate blood clotting, getting rid of alcohol and storing glucose, some vital vitamins and iron [5].

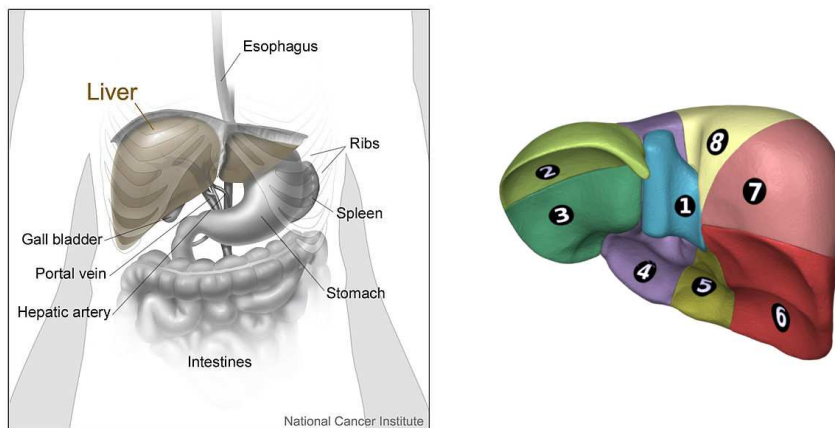


Figure 1.1. Human liver position and Couinaud classification system [6, 7].

Liver tumors can be divided in primary or secondary tumors. Secondary liver tumors are far more frequent than primary liver tumors and concern cancer cells that

originate from other organs, i.e. cancer cells that have migrated from organs such as the lung, colon, breast to the liver; these are called liver metastases. Primary liver tumors, called hepatocellular carcinoma (HCC), arise in the liver itself, and are mainly caused by cirrhosis due to either hepatitis virus or alcohol, and fatty liver [8].

Primary liver cancer is the second common cancer in the world and the five-year survival rate of liver cancer without treatment is lower than 15% [9]. Liver cancer is more common in developing countries in sub-Saharan Africa and Southeast Asia than in the US and developed countries in Europe. Worldwide, more than 800,000 people are diagnosed with liver cancer each year. This cancer also causes around 700,000 deaths each year [10]. Per WHO data published in 2014, liver cancer accounts for around 20,000 deaths of 75,000 deaths of cancer in Vietnam or 4.29% of total deaths annually [11].

1.2 Liver cancer imaging

Liver cancer can be diagnosed using various imaging modalities, such as US, multi-phase CT, MRI, PET (see Fig 1.2 for an example of a CT machine).



Figure 1.2. A typical CT machine of Siemens [12].

Ultrasound: Ultrasound imaging, also called sonography, is a medical imaging modality which uses high-frequency sound waves to produce pictures of the inside of the body (see Fig 1.3). Ultrasound imaging uses a transducer, which is placed directly on the skin. Ultrasound waves are transmitted from the transducer into the body. At interfaces between different structures the waves are bounced back to the transducer. The transducer collects these waves to create an image. Ultrasound imaging does not use ionizing radiation, and is principally harmless [13]. Depending on probe type, ultrasound imaging can be 2D or 3D and can be acquired in real-time. Therefore, this modality can show not only structure but also movement of the internal organs of the body. Beside the normal mode, called B mode, Doppler mode is a special ultrasound technique that permits clinicians to investigate and evaluate blood flow through vessels of the liver as well as other body organs such as the kidneys and the heart. Compared

to other imaging modalities, ultrasound is low-cost and mobile, and hence frequently used in liver disease diagnosis and treatment. However, image interpretation remains difficult among others because of the speckled nature of these images. Additionally, not all tumors can be well visualized in ultrasound images [14]. This can partly be improved by using ultrasound specific contrast agents (microbubbles) [15]. However, side effects of the contrast agents, such as capillary rupture, hemorrhage, and dye extravasation, limit the use of them in practice [16].



Figure 1.3. A US image of a necrotic liver tumor (arrow). Image is adopted from [17].

Computed tomography: Computed tomography, or CT, is an imaging modality which combines multiple X-ray projections taken from different orientations around a z-axis to generate a cross-sectional image of the body. Series of cross-sectional images can be stacked together to obtain a 3D image. Computed tomography can image the structure of internal organs such as the liver [18]. However, computed tomography is not a real-time imaging modality such as ultrasound. In addition, it uses ionizing radiation. Lowering the dose leads to reduction of the image quality.

Multiphase CT can be used for investigating blood vessels and tumor enhancement (see Fig 1.4): contrast agent is used to highlight vessels and tumors. Once contrast agent is injected into the bloodstream (generally the antecubital vein in the forearm), it flows through the heart via the arteries to the liver, and via the intestines to the portal vein [19]. Depending on the timing, enhanced CT images are acquired in the arterial phase, the portal venous phase or a delayed phase, which highlights respectively the liver arteries, the liver veins, or late enhancement (relevant for tumor imaging). Contrast enhanced CT is frequently used in diagnosis of liver cancer as well as for image guidance during liver interventions [14, 18]. However, as the contrast agent is harmful to the kidney (nephrotoxic), the use of contrast agent should be limited, which has consequences for the use in the interventions [20].

Magnetic resonance imaging (MRI) is a medical imaging modality which uses a strong magnetic field, radio frequency (RF) pulses, and field gradients to produce images of the inside of the body. Similar to CT, MRI generally produces a 2D image

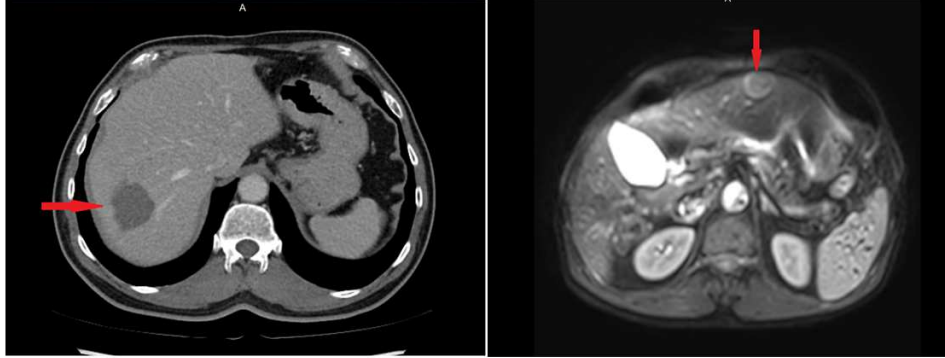


Figure 1.4. A contrast enhanced CT image - portal venous phase of the liver with a tumor (left) and a large tumor in the liver in a contrast enhanced MRI image (right).

of a cross-sectional slice of the body (see Fig 1.4), which can be stacked to obtain 3D volumes. Direct 3D imaging is possible as well. Unlike CT, MRI does not involve ionizing radiation but side effects from exposure under high magnetic field, though rare, have also been reported [21]. MRI is more sensitive to soft tissue than CT but acquiring an image takes more time. Because of these properties, MRI is also used in diagnostics of the liver disease as well as other anatomical structures. It is not necessary for MRI to use contrast agents to image vessels as the varying properties of blood, e.g. flow, and the tissues contain natural contrasts. However, specific types of MRI imaging commonly use intravenous contrast agents [14, 22].

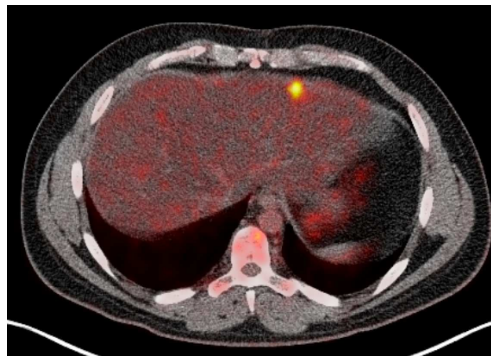


Figure 1.5. PET-CT image pair depicting liver cancer.

Positron emission tomography (PET) is a functional imaging modality which is able to capture metabolic processes in the body. A short-lived radionuclide (tracer), which decays by emitting a positron, penetrates the body via chemical injection of a

metabolically active molecule (most commonly fluorodeoxyglucose (FDG), a type of glucose). An hour after the injection, the metabolically active molecule concentrates in tissues of interest, in case of FDG in energy consuming tissues such as tumors. 3D images of the tracer concentration within the body are then generated by computer analysis, which are used to determine the presence of cancer metastasis [23,24]. Since PET images do not provide detailed anatomical information, it is usually combined with MRI or CT [14,18]. In a PET-CT scanner, PET and CT acquisition is achieved in the same session (see Fig 1.5). One of the limitations of PET-CT scanners is the high operating cost.

1.3 Liver cancer treatments

There are many different treatments for liver cancer patients. The Barcelona clinic liver cancer (BCLC) staging classification is widely used in HCC treatment [25–27], and there are similar schemes developed by other groups as well. For metastatic tumors, there is not such a specific scheme, so clinicians decide based on their experience / knowledge. The best treatment for HCC is surgery (resection of liver part that contains the tumor); a healthy liver is able to regrow the resected section, up to 75% of the total liver, in just a few months [28]. Unfortunately, not all patients are suitable for surgery, either because of their health status, the liver condition as being cirrhotic and/or multi tumor spread out through the liver or even to other organs.

In those cases, minimally invasive approaches may be used. There are many minimally invasive approaches, all focusing on destroying the tumor while sparing as much as possible healthy liver tissue. A common minimally invasive approach is Radiofrequency Ablation (RFA), in which an ablator is inserted into the tumor, after which radio frequency is applied to locally heat, and irreversibly destroy the tumor [29]. Microwave Ablation (MWA) is similar to RFA, but uses microwaves instead of radiofrequency to heat the tumor. Microwaves deposit more energy than radio waves, thus this technique is more difficult to control [30]. Cryoablation is similar to RFA. The difference is that tumors are treated by freezing instead of heating [31]. Transcatheter Arterial Chemo Embolization (TACE) and radiotherapy, also minimal invasive approaches, involve chemical toxic or radiation to either embolize the vessel feeding the tumors or directly destroy the tumor [26].

Each of the minimally invasive approaches has advantages and disadvantages [33]. In ablation approaches, nearby vessels may cause cooling (heatsink effect), thereby leading to incomplete ablation. Also, in ablation, the heating cannot be steered, and may therefore not be an option if the tumor is close to critical structures. For all of the minimally invasive approaches, the challenge is to get the instrument (ablation needle, catheter, radiation beam) into the target lesion [34,35]. Therefore, image guidance during these interventions is critical (see Fig 1.6).

For ablations, ultrasound and CT are mostly used for image guidance during insertion of the needle (see Fig 1.7). Ultrasound imaging is real-time and harmless, so it is the first choice for image guidance. However, the tumor is not always visible in ultrasound images, and in those cases CT-guidance may be used. If the intra-operative CT image is non-contrast enhanced, the clinicians need to mentally map



Figure 1.6. A setup of an interventional angiography room with a C-arm and a CT machine [32].

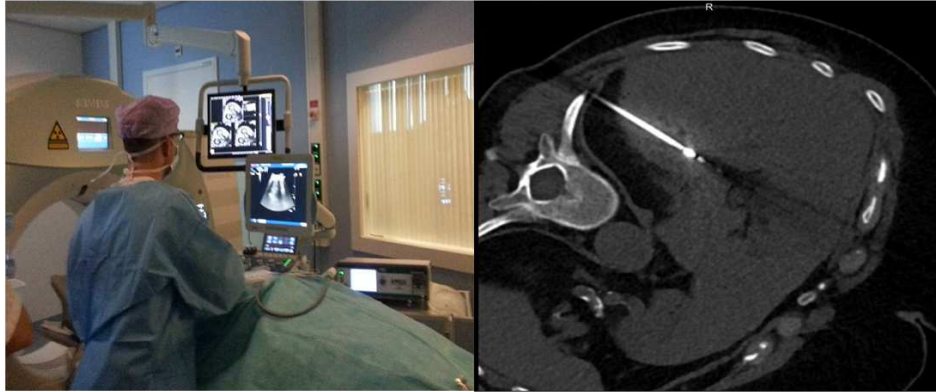


Figure 1.7. A typical liver RFA intervention under guidance of US/CT (left) and the interventional reformatted CT image of the liver with the ablator (right).

the tumor location from the pre-operative image to the intra-operative image, which may be complex, because of differences in the patient orientation, respiratory state, etc. [34, 36, 37].

In TACE, therapeutic agents are brought to the tumor with a catheter via the liver arteries. During the intervention, the interventional radiologist makes angiograms (Fig. 1.8) to visualize the catheter in the vessels and to identify the main branch of the hepatic arteries which feed the tumor(s). Once the artery feeding the tumor has been reached with the catheter, chemotherapy loaded beads are injected through the catheter [39].

Image-guided radiation therapy (IGRT) is a procedure where the tumor is irradiated with a high dose of radiation. The challenge in this procedure is to get a high



Figure 1.8. An interventional X-ray machine and an angiogram of the liver in TACE procedure [38].

dose at the tumor site, while limiting the dose to healthy surrounding tissues. At the start of the treatment, imaging is used to position the patient in the radiotherapy device. For this, computed tomography (CT), cone beam computed tomography (CBCT) or X-ray images are used [40].

1.4 Purpose and contents of this thesis

Purpose of this thesis is to develop and evaluate image analysis techniques to support minimally invasive treatment of liver cancer, focusing on image fusion. Most of the work focuses on CT imaging, but also some work towards inter-modality analysis is performed. The thesis consists of the following contributions:

Chapter 2 describes an evaluation of several well-known diffusion filters and vesselness filters by comparing their impact on liver vessel segmentation in abdominal contrast enhanced CT data. This is relevant for registration of CT-US, in which vessels can be used as a feature for the registration, as well as for the planning of ablation procedures, where vessel information is relevant for the therapeutic decision making.

An automated registration method for improved image guidance of RFA in liver interventions is presented in chapter 3. Diagnostic images (contrast enhanced CT image with tumor segmentation) are non-rigidly aligned to the intra-intervention images in which the tumors are often invisible without contrast agent. In this work, a rigidity term is used to eliminate unrealistic deformation in the registration.

In chapter 4, a semi-automated registration method is proposed to improve the pre-intra interventional image registration introduced in the previous chapter. The method uses a user-defined set of points in the intra-operative images and a liver segmentation in the pre-operative image, and uses a point-to-surface term based on these annotations to maximize the surface alignment between the pre-operative images

and the intra-operative images.

Assessment of liver deformation in the pre-operative images and the intra-operative images is introduced in chapter 5. In this work we quantify the non-rigid component of deformation of the liver, for the complete liver as well as sub-xiphoidal and intra-costal region as would be imaged with a 3D US transducer. These quantifications are relevant for rigid registration based image fusion approaches, such as e.g. used in current US-CT fusion in image guidance for ablation.

Chapter 6 introduces a registration framework for RFA treatment evaluation. In this work, we non-rigidly register the pre-interventional images and the post-intervention images. After the registration, the margin between the tumor and the ablation zone can be quantified, which may enable better assessment of the intervention success.

In chapter 7, we discuss the achievements of our study and future research directions.

Quantitative evaluation of noise reduction and vesselness filters for liver vessel segmentation on abdominal CTA images

Abstract — Liver vessel segmentation in CTA images is a challenging task, especially in case of noisy images. This chapter investigates whether pre-filtering improves liver vessel segmentation in 3D CTA images. We introduce a quantitative evaluation of several well-known filters based on a proposed liver vessels segmentation method on CTA images. We compare the effect of different diffusion techniques i.e. Regularized Perona-Malik, Hybrid Diffusion with Continuous Switch and Vessel Enhancing Diffusion as well as vesselness approaches proposed by Sato, Frangi and Erdt. Liver vessel segmentation of the pre-processed images is performed using a histogram-based region growing with local maxima as seed points. Quantitative measurements (sensitivity, specificity and accuracy) are determined based on manual landmarks inside and outside the vessels, following by T-tests for statistic comparisons on 51 clinical CTA images. The evaluation demonstrates that all the filters make liver vessel segmentation to get significantly better accuracy than without using a filter ($p < 0.05$); with Hybrid Diffusion with Continuous Switch achieves the best performance. Comparing to the diffusion filters, vesselness filters have better sensitivity but less specificity. In addition, the proposed liver vessel segmentation method with pre-filtering is shown to perform robustly on clinical dataset having low contrast-to-noise up to 3 (dB). The results indicate that pre-filtering step significantly improves liver vessel segmentation on 3D CTA images.

2.1 Introduction

Analysis of liver vasculature plays an important role in several clinical applications [41,42]. It is relevant for endovascular interventions, such as Transjugular Intrahepatic Portosystemic Shunt placement (TIPS) [43] and Transcatheter Arterial ChemoEmbolization (TACE) [44]. In a TIPS procedure, a shunt is created between the hepatic vein and the portal vein to remedy high pressure in the portal vein. In a TACE procedure, a tumor is embolized by occluding its feeding arteries with small particles. Finding these arteries can prove to be quite challenging. Additionally, analysis of liver vasculature is an essential step in the planning of other liver interventions such as tumor resection and treatment. In Radiofrequency Ablation (RFA) of liver tumors, knowing the tumor position with respect to the vasculature may determine treatment success [45,46]. Furthermore, liver vessel segmentation is an important step in image fusion techniques [47].

3D diagnostic images of the liver are often acquired by Computed Tomography Angiography(CTA). Quality of the liver CTA images, however, varies considerably and can be characterized by contrast-to-noise ratio (CNR) [48]. Three major factors determine the CNR of CTA images: (i) tube-potential and tube-current, (ii) amount of contrast agent and (iii) timing of data acquisition with respect to dose injection [49]. In the clinical range, radiation dose is related to both tube-potential and tube-current. Recently, radiation dose awareness has been growing, leading to reduced dose and images with lower CNR. In addition, the quality of the CTA images also depends on patient mass and liver disease. Especially in case of cirrhotic livers, quality of the CTA image decreases because of the more heterogeneous liver tissue density (Fig. 2.1). Analysis of the images, in particular analysis of the liver vessels, may be supported by automated segmentation of these images. This is a challenging task in low CNR CTA images. The purpose of this work therefore is to investigate to what extent various popular vessel-enhancing and noise-reduction filters may improve liver vessel segmentation. Focus is on portal-venous phase CTA images of the liver.

There have been several liver vessel segmentation methods reported in literature. Makowski and Sergio (2008) [50] presented a review of liver vessel segmentation, and a review on vessel segmentation was published by Lesage *et al.* (2009) [51]. These vessel segmentation methods can be classified into different groups, based on the algorithm applied:

1. Region growing and thresholding approaches [52–58].
2. Level-set and active-contour based methods [48,59].
3. Graph-cuts [60–64].
4. Other methods such as morphology-based segmentation and Gaussian mixture model approach [65–73].

Most methods for liver vessel segmentation in 3D CTA use a filter to reduce the noise and enhance the vessel structure. Mainly, multiscale Hessian-based filters and diffusion filters [48,58,61] have been used in these studies. These studies, however, lack an evaluation on to what extent preprocessing improves the segmentation results.

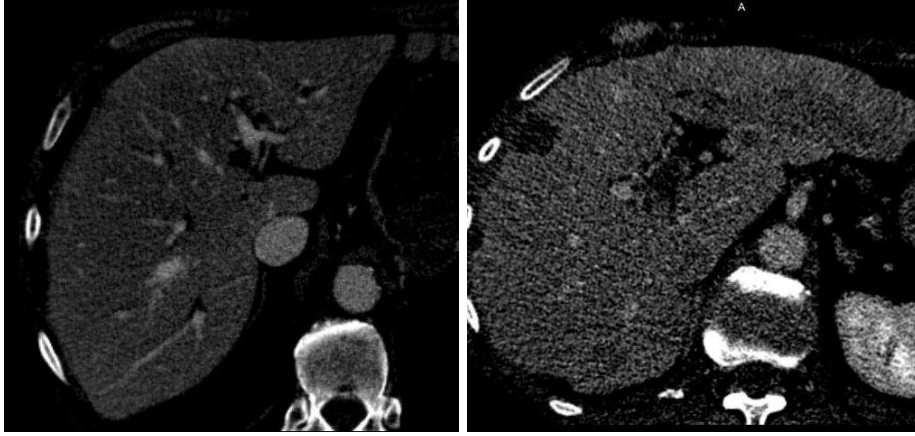


Figure 2.1. (Left) CTA image of a normal liver (120kV-310 mAs), CNR = 16.2 dB; (right) noisy CTA image of a cirrhotic liver (100kV-140 mAs): CNR = 2.8 dB.

Also, the effect of these filters on the final output is often not investigated. A non-quantitative comparison of multiscale Hessian-based filters can be found in [74]. In a previous study, we quantitatively evaluated the effect of diffusion filters on signal-to-noise ratio (SNR) of liver images [75].

The main contributions of this paper are threefold. First, an evaluation framework for comparing pre-filtering approaches for automated liver vessel segmentation is proposed (including datasets and annotations). Second, a quantitative comparison of various vessel-enhancing and noise-reduction filters on venous phase CTA images is performed using our evaluation setup, and an evaluation of the effects of these filters on subsequent vessel segmentation. Third, we propose an automatic liver vessel segmentation method on CTA images, which is used as part of the evaluation framework. In the evaluation, we include three well-known diffusion filters: Regularized Perona-Malik [76], Vessel Enhancing Diffusion [77] and Hybrid Diffusion with Continuous Switch [78], and three multiscale Hessian-based filters: Frangi [79], Sato [80] and Erdt [60].

The chapter is organized as follows: in the next section, we briefly describe the filters applied and the vessel segmentation approach. Section Experiments and Results 2.3 presents our experimental setup and the evaluation framework, as well as the results of our experiments. In section Discussion 2.4, these results are discussed, and conclusions are drawn in section Conclusion 2.5.

2.2 Methods

Many approaches have been published to enhance medical images. We chose to implement three vesselness filters, namely Hessian-based filters introduced by Frangi, Sato and Erdt. The methods by Frangi and Sato are the most frequently cited, and Erdt was demonstrated to perform well in comparison with these [74]. Additionally, we

implemented three diffusion approaches: the standard inhomogeneous isotropic Regularized Perona-Malik diffusion (RPM), Vesselness-enhancing diffusion (VED) and Hybrid Diffusion with Continuous Switch (HDCS), which is a relatively new approach that combines both Edge Enhancing Diffusion (EED) and Coherence Enhancing Diffusion (CED) [81]. These filters are described in more detail in the next subsection. This description is followed by a description of the liver vessel segmentation approach.

2.2.1 Vesselness filters

Assuming that a vessel can be viewed as a bright circular region in the cross-sectional plane, and as a bright line along the vessel direction, most vesselness filters are based on 2nd order filters. The considered filters determine the Hessian matrix, and subsequently combine the eigenvalues of Hessian matrix into a vesselness measure. They all intend to enhance tube-like structures (vessels) and suppress other (plate-like and blob-like) structures, but do it in different ways.

The Hessian matrix is conventionally obtained via Gaussian derivatives, and generally a multi-scale approach is adopted to capture the varying sizes of the vessels by combining the maximum response of each scale.

1. **Frangi:** One of the most well-known vesselness filters was introduced by Frangi *et al.* (1998) [79]. This vesselness filter can enhance either dark vessels on a bright background or bright vessels on a dark background. In 3D liver CTA datasets, vessels are brighter than the background because of the contrast agent. After performing eigenvalue decomposition of the Hessian matrix, the eigenvalues are sorted as: $|\lambda_1| < |\lambda_2| < |\lambda_3|$. The smallest (in absolute magnitude) eigenvalue corresponds to the direction of the vessel, whereas the other two eigenvalues correspond to directions orthogonal to the vessel. Based on these eigenvalues, Frangis vesselness discriminates tubular structures from blob-like or plate-like structures and background. Its formulation is given as:

$$V_F(\sigma) = \begin{cases} 0 & \text{if } \lambda_2 > 0 \text{ or } \lambda_3 > 0 \\ (1 - e^{-\frac{R_A^2}{2\alpha}})e^{-\frac{R_B^2}{2\beta}}(1 - e^{-\frac{R_S^2}{2\gamma}}) & \text{else} \end{cases}, \quad (2.1)$$

where α , β , and γ are parameters which control the sensitivity of $R_A = |\lambda_2/\lambda_3|$, $R_B = |\lambda_1|/\sqrt{|\lambda_2\lambda_3|}$ and, $R_S = \sqrt{\sum_j \lambda_j^2}$. The term R_A , the ratio of the two biggest eigenvalues, describes whether the local structure is more plate-like or tube-like, the term R_B accounts for blob-like structures and the term R_S deals with the difference between vessel and background areas.

2. **Sato:** The vesselness filter proposed by Sato *et al.* (1998) [80] was designed for bright-vessel datasets but may be adapted for dark-vessel datasets. The filter is based on only two eigenvalues of the Hessian matrix. First, the eigenvalues are sorted as $\lambda_1 > \lambda_2 > \lambda_3$. Second, $\lambda_c = \min(-\lambda_2, -\lambda_3)$ is the smaller value of the two sign-inverse smallest eigenvalues λ_2 and λ_3 . The response is formulated as:

$$V_S(\sigma) = \begin{cases} \exp(\frac{-\lambda_1^2}{2(\alpha_1 \lambda_c)^2}) \lambda_c & \text{if } \lambda_1 \leq 0, \lambda_c \neq 0 \\ \exp(\frac{-\lambda_1^2}{2(\alpha_2 \lambda_c)^2}) \lambda_c & \text{if } \lambda_1 > 0, \lambda_c \neq 0 \end{cases}, \quad (2.2)$$

where $\alpha_1 < \alpha_2$ are two parameters which modulate the ratio between λ_1 and λ_c . In the ideal case of a bright vessel, the eigenvalues are all negative and $\lambda_1 \approx 0$ and $\lambda_2 \approx \lambda_3 \ll 0$, and consequently, the response is high. If λ_1 is positive and $\lambda_2 \approx \lambda_3 \ll 0$, in which case the vessel is corrupted because of signal loss (intensities of voxels at the corrupted part are lower than they should be), the response is slightly higher to compensate the corrupted part. In case of sphere-like structure, where $\lambda_1 \approx \lambda_2 \approx \lambda_3$, the filter response is close to 0.

3. **Erdt**: Erdt *et al.* (2008) [60] defined a vesselness filter in a different way but also using Hessian eigenvalues. The eigenvalues are sorted as $\lambda_1 > \lambda_2 > \lambda_3$. Then the vesselness function is given by:

$$V_E(\sigma) = K \left(\frac{2}{3} \lambda_1 - \lambda_2 - \lambda_3 \right), \quad (2.3)$$

where $K = 1 - \frac{\|\lambda_2 - \lambda_3\|}{|\lambda_2| + |\lambda_3|}$. In case of vessel structures, where $\lambda_1 \approx 0$ and $\lambda_2 \approx \lambda_3 \ll 0$, $V_E(\sigma)$ gives a high response. Otherwise, it gives a low response. The K factor acts as modulator which approaches 1 when $\lambda_2 \approx \lambda_3$, in the case of a vessel-like structure, and goes to 0 if the difference between λ_2 and λ_3 becomes large. This helps in reducing very bright, non-tube-like structures. This filter only has the scale of the Gaussian as input parameter.

2.2.2 Diffusion Methods

Diffusion filters solve the partial differential equation $u_t = \text{div}(D \cdot \nabla u)$ where ∇u is the gradient of the image and D is the diffusion tensor, which steers the diffusion. If the diffusion tensor D is replaced by a scalar-valued diffusivity g , the diffusion will be isotropic. In case D is an anisotropic tensor, it can model anisotropic diffusion. RPM thus is an isotropic diffusion method, as it varies only the amount of smoothing based on local gradient magnitude, whereas VED and HDCS are anisotropic diffusion methods, that not only locally change the magnitude but also the direction of smoothing by adapting the diffusion tensor D . Each of the diffusion methods is described in more detail below.

1. **RPM**: Perona and Malik (1990) [76] introduced an isotropic nonlinear diffusion described by $u_t = \text{div}(g(|\nabla u|) \cdot \nabla u)$. The scalar-valued diffusivity $g(|\nabla u|)$ is a function of the gradient magnitude $|\nabla u|$, causing filtering in homogenous areas while retaining edges with high gradient. Catte *et al.* (1992) [82] proposed the following scalar-valued diffusivity function for the non-linear diffusion using Gaussian derivative at scale σ :

$$g(|\nabla u_\sigma|) = 1 - e^{\frac{-C}{(|\nabla u_\sigma|^2 / \lambda^2)^4}}, \quad (2.4)$$

where $C = 3.1488$ and λ is the contrast parameter. The contrast parameter λ acts as a threshold scale for the gradient magnitude $|\nabla u_\sigma|$. If the gradient is large, compared to the contrast parameter, i.e $|\nabla u_\sigma|^2 \gg \lambda^2$, this results in $g(|\nabla u_\sigma|) \approx 0$, reducing the amount of diffusion. Therefore strong edges, where $|\nabla u_\sigma|$ is large, are preserved. Parameter σ denotes the scale of the Gaussian used to calculate the gradient. The value of σ should be chosen based on variance of the noise and the size of the small structures we want to retain.

2. **HDCS:** Mendrik *et al.* [78] introduced HDCS as a combination of two other diffusion filters: CED and EED [81]. Both CED and EED use the structure tensor to derive a diffusion tensor. While CED is suitable for filtering tube-like structures, EED works well with flat areas and edges. The main idea of HDCS is to use a voting criterion to decide whether local structure is tubular or non-tubular. The structure classifier is defined as:

$$\xi = \frac{\mu_1}{\alpha + \mu_2} - \frac{\mu_2}{\alpha + \mu_3} \quad , \quad (2.5)$$

where $\alpha = 0.001$ and $\mu_1 > \mu_2 > \mu_3$ are eigenvalues of tensor product $J_\rho(\nabla u_\sigma) = K_\rho * (\nabla u_\sigma \nabla u_\sigma^T)$, and K_ρ is a Gaussian convolution kernel which acts as smoothing factor in the tensor product J_ρ . The classifier $\xi \ll 0$ when the structure is tubular, $\xi \approx 0$ when structure is sphere-like (noise), and $\xi \gg 0$ when structure is plate-like (background). The HDCS diffusion tensor D_H is then given by $D_H = Q \Lambda Q^T$, where Q is the matrix of eigenvectors, and Λ , a diagonal matrix with λ_{h_i} on the diagonal ($i = 1, 2, 3$ in case of 3D data), is a combination of the eigenvalues of EED (λ_{e_i}) and CED (λ_{c_i}):

$$\lambda_{h_i} = (1 - \varepsilon) \lambda_{c_i} + \varepsilon \lambda_{e_i} \quad , \quad (2.6)$$

$$\varepsilon = \exp\left(\frac{\mu_2((\lambda_h^2 \xi - |\xi|) - 2\mu_3)}{2\lambda_h^4}\right) \quad , \quad (2.7)$$

where λ_h is a contrast parameter. When the local structure is tubular, $\varepsilon \rightarrow 0$ and the diffusion is CED-like, for other structures $\varepsilon \rightarrow 1$, and the diffusion is EED-like.

3. **VED:** Manniesing *et al.* (2006) [77] used the multi-scale Hessian filter response to drive the diffusion. The main idea is that by using eigenvalues of the Hessian matrix, we can define a diffusion tensor D_V that depends on the local curvature. Let $V \in [0, 1]$ be the output of a multiscale scale vesselness filter. V should be around 1 inside tubular structures and 0 elsewhere. If $|\lambda_1| < |\lambda_2| < |\lambda_3|$ are eigenvalues of Hessian matrix H , corresponding to eigenvectors Q_1, Q_2 and Q_3 . i.e. $H = Q \Lambda Q^T$, then Q_1 is the direction of the least curvature (along vessel in case of vessel structure). The diffusion tensor is defined as $D_V = Q \Lambda' Q^T$. Diagonal elements of matrix Λ' can be defined as:

$$\begin{cases} \lambda'_1 = 1 + (\omega - 1)V^{1/S} \\ \lambda'_2 = \lambda'_3 = 1 + (\varepsilon - 1)V^{1/S} \end{cases} \quad , \quad (2.8)$$

where S is a sensitivity parameter which controls the impact of V on λ'_1 ; ω is a parameter larger than 1, which ensures that Q_1 is always the direction of the largest diffusion; ε is relative small, compared to ω , to allow high isotropic diffusion when $V \approx 0$ (non-vessel structure).

2.2.3 Liver vessel segmentation method

Here, we present the liver vessel segmentation method that we used to investigate the effect of different pre-processing sttiff (see Fig. 2.2 for an overview). The method comprises an automated approach for selecting seed points and a threshold interval, followed by a region growing process from these seed points, using the estimated threshold. As a prior step, a liver mask is determined.

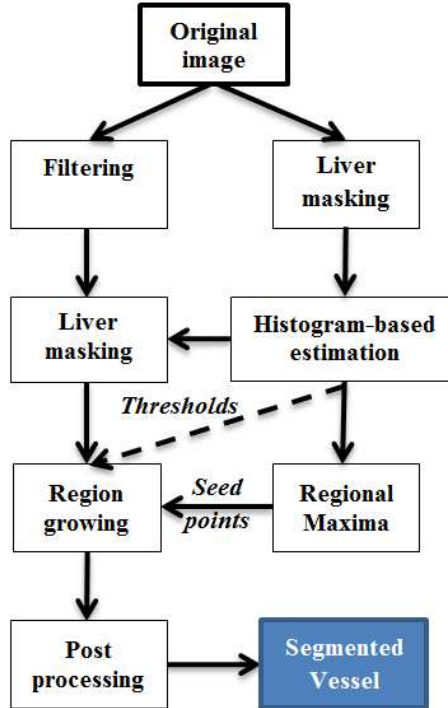


Figure 2.2. Flow diagram of the liver vessel segmentation method.

Step 1 *Masking the liver*

First, a liver mask is created. The liver mask does not need to be highly accurate. The requirement is that it contains the liver vessels and the liver parenchyma (Fig. 2.3). In our case we manually draw contours around the liver on around ten slices and then interpolate these contours. This manual step also could easily be replaced by an automatic liver segmentation method, e.g. [83]. Note

that the liver mask is also applied on the filtered images and the original image to ensure the same region of interest.

Step 2 *Histogram-based threshold estimation*

In the second step, we determine parameters used to calculate thresholds for both seed point extraction in Step 3 and region growing in Step 4 using histogram estimation. We determine a smoothed intensity histogram of the masked liver by using 1024 bins over the complete intensity range, convolved with a low pass filter (kernel [0.25 0.5 0.25]). Based on this histogram, we estimate the background intensity distribution. To this end, we fit a Gaussian distribution to the histogram [58, 66]. From Figure 2.3b, it can be observed that the vessel voxels, that are on the right side of histogram, overlap with the tail of the distribution of the background. If the variance of the background intensities is too large and vessel brightness is not sufficiently high, vessel and noisy liver parenchyma voxels may have similar intensity values. If the liver contains a tumor, which generally is darker than the other tissue, the low intensity part of the histogram may be slightly elevated. We use the following criterion to determine a threshold for separating vessel and liver parenchyma, which is used in region growing method:

$$T_L = p + \frac{1.75}{2\sqrt{2\log(2)}}(h_r + h_l) + \alpha(h_r - h_l) \quad , \quad (2.9)$$

where p is the position of the highest peak of the histogram, h_r and h_l are half width at half maximum to the right side and the left side, and α is a parameter that accounts for asymmetry in the histogram. The parameter α depends on the quality of dataset. In all our experiments, we used $\alpha = 2$. In case of a perfect Gaussian fit, $h_r = h_l$, the threshold $T_L = \mu + 1.75\sigma$, where $\mu = p$ and $\sigma = (h_r + h_l)/(2\sqrt{2\log(2)})$ are mean and standard deviation of the Gaussian. The position of 1.75σ from the mean is approximately at 95% of the cumulative density function of a Gaussian distribution. This procedure guarantees that at least 95% of the liver parenchyma voxels will not be part of the liver vessel segmentation (see Step 4). Note that this is a 95% threshold of the noisy background intensity distribution around the vessels (inside the liver mask), not 95% of cdf of the whole volume.

Step 3 *Seed points from regional maxima*

The region growing method requires seed points to initiate the process. As liver vessels are brighter than liver parenchyma in contrast-enhanced CTs, we use maxima in small regions as seed points for region growing. The original dataset masked by a liver mask is used to extract the seed points (see Fig.2.4a). We employ two strategies to prevent selecting too many maxima and to prevent selection of maxima from the background. First, the masked liver volume is divided into multiple sub-regions. The size of a sub-region is chosen sufficiently small to not contain two or more different vessels inside it, and sufficiently large to achieve a limited number of sub-regions. We choose 5x5x3 mm as the size of

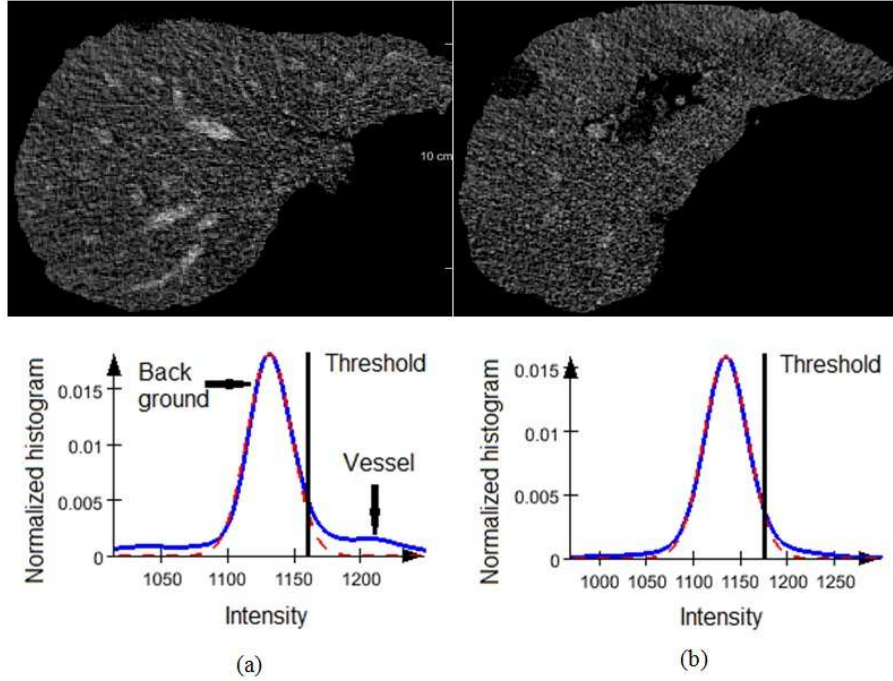


Figure 2.3. (a) A high contrast-to-noise liver image (12.4 dB) and its histogram; smoothed liver histogram (continuous curve) with estimated noise distribution (dashed curve). The vessel peak is separated from background areas. (b) A low contrast-to-noise image (2.8 dB) and its histogram.

a sub-region because of vessel size and asymmetric of spatial vessel distribution. Because of varying resolution of datasets, $5 \times 5 \times 3$ mm volume is approximated to be a cubic volume of voxels. In each sub-region, we search for the global maximum. Subsequently, all maxima lower than the threshold $T_M = p + 3\sigma$, where p and σ are the highest peak position of the histogram and the noise standard derivations in Step 2, are ignored (see Fig.2.4b). In general, there are around 30 to 200 seed points per dataset extracted in this stage. These seed points are determined using the original dataset, and they are used as inputs for the six filters. Thus the segmentations for the various filters all use the same set of seed points.

Step 4 *Region Growing*

The traditional seeded region growing method [84] is applied to segment the entire vessel tree using the seed points and thresholds described above. Region growing has been used in several previous approaches to liver vessel segmentation. Region growing is suitable for liver vessel segmentation with the pre-filtering techniques because this method is based on intensity distribution and connectivity of the vessels. With proper settings, all the six filters either

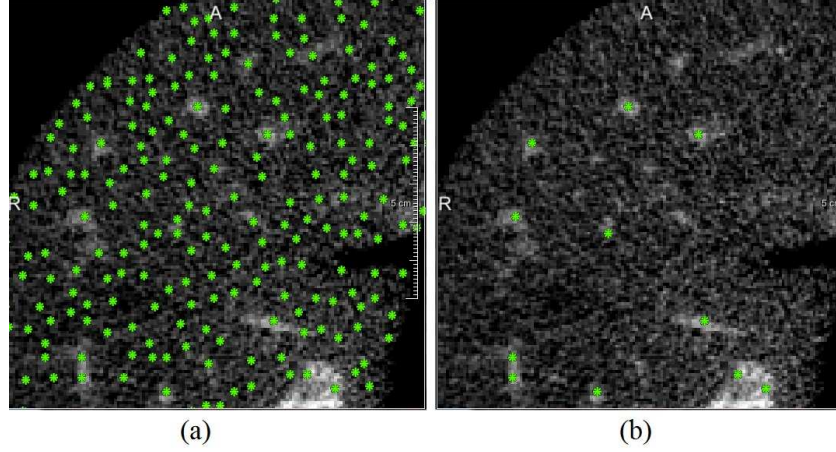


Figure 2.4. Seed points using the threshold to eliminate number of points: (a) without using the threshold, (b) using the threshold.

enhance vessels or reduce noise while guaranteeing vessel connectivity and differences between vessel intensity and background intensity (in general, vessels intensity is higher than background intensity see Fig. 2.8a and 2.9a).

Step 5 *Post-processing*

Owing to noise, the vessel segmentation may contain isolated parts, holes inside the vessel and a non-smooth surface. Therefore, a morphological closing operator with kernel $5 \times 5 \times 3$ voxels is applied as a post-processing step and subsequently all isolated segmentation parts consisting of less than 10 voxels are removed.

2.3 Experiments and Results

CTA Data and preprocessing: 51 abdominal CTA datasets were retrospectively obtained from the Erasmus MC, University Medical Center Rotterdam and anonymized. The images were acquired on a Siemens CT Scanner. We selected images in the portal-venous phase from the multiphase abdominal CT-scans. The images have an in-plane pixel size of $0.74 \text{ mm} \times 0.74 \text{ mm}$ or $0.54 \text{ mm} \times 0.54 \text{ mm}$, 1-1.5 mm slice spacing, 1-2 mm slice thickness, 72-180 axial slices, 512×512 pixels per slice. Image acquisitions were performed 60 seconds after the injection of 100 cc intravenous contrast agent with a tube-current of 110 - 320 mAs, and tube-voltage of 80 - 120 kV. In 15 cases, the livers are cirrhotic, 29 cases contain tumors, cysts, metastases in different shapes and sizes, and there are 3 cases including metal artifacts. 51 datasets are divided into 3 groups: group A, group B and group C. Group A is for training stage which contains 10 dataset randomly selected from all 51 datasets; Group B contains 22 datasets and group C contains 19 datasets.

The field of view of the original 3D CTA images is generally larger than the liver. Therefore, to remove the organs not relevant for our study, and to facilitate further processing, we manually cropped the datasets to fit the liver.

Implementation details: All filter programs in this study were written in CPP and run on a Linux cluster. The filters were implemented based on available classes and programs in the Insight Segmentation and Registration Toolkit. The RPM diffusion filter was coded using the `itkAnisotropicDiffusionImageFilter` class. We used the VED source code from [85]. The HDCS, CED and EED source codes were taken from [86]. Frangi’s filter and Sato’s filter implementations were taken from [87]. The liver vessel segmentation algorithm was implemented based on `itkConnectedThresholdImageFilter` class. We implemented Erdts filter based on some introductions from the author. The implementations of the filters are publicly available at BGR liver CT database website.

2.3.1 Evaluation framework

The evaluation of vessel segmentation algorithms is a notoriously difficult problem. The complex vessel topology, the blurring of the vessel boundary and non-uniform vessel contrast in CTA images makes a manual segmentation and a direct evaluation on a gold standard an infeasible approach. Indeed, recent challenges including vessel segmentation only evaluated a single bifurcation [88] or small parts of the vessel tree [89]. Therefore, we propose a quantitative evaluation approach utilizing landmarks. For each CTA dataset, initially 5 axial slices are randomly selected. These contain vessels of various size and contrast, and in each selected slice, markers are manually placed inside all visible vessels and corresponding background markers are placed nearby vessels. For datasets in group A and B, each vessel in a slice contains 1 vessel landmark and 1 background landmarks. For datasets in group C, each vessel contains 1 vessel landmark and 4 background landmark. Thus, for each dataset in group C, around 300 to 700 vessel landmarks and 1200 to 2100 background landmarks are annotated (Fig. 2.5). If the first five slices have less than 300 landmarks, we repeatedly add one random slice to place landmarks until the number of vessel landmarks is higher than 300. The datasets in group C are also annotated by the second observer in order to determine inter-observer variation. Using these landmarks, we define:

- True Positives: vessel markers inside the segmentation
- False Positives: background markers inside the segmentation
- True Negatives: background markers outside the segmentation
- False Negatives: vessel markers outside the segmentation

Then sensitivity, specificity and accuracy are defined in the common way:

- Sensitivity = $TP / (TP + FN)$
- Specificity = $TN / (TN + FP)$
- Accuracy = $(TP + TN) / (TP + FN + TN + FP)$

These metrics are used in the evaluation.

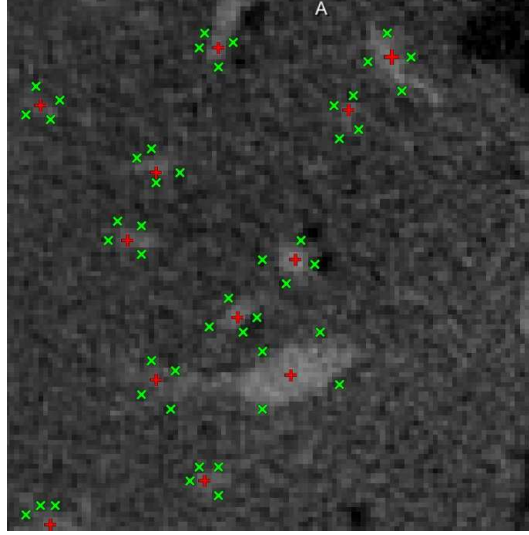


Figure 2.5. Reference marker: red + markers are inside vessels and green x markers are nearby vessels.

2.3.2 Training

Purpose of the training stage is to determine the optimal parameter values for each filter from section Methods 2.2. 10 datasets in group A are used for determining optimal parameter values. We apply the filters with varying parameter settings to each of the training images, and evaluate the segmentation result. The parameter settings that yielded the highest average accuracy over all datasets were used in the testing stage. In the optimization, we first selected reasonable parameter ranges based on common knowledge (such as vessel sizes and CNR) and pilot experiments. Within these ranges, we discretized the parameter values and evaluated all possible combinations, which results in the optimal value within the pre-determined ranges. In this way, we are certain that we covered the complete range of relevant parameter values. Finally, we inspected the optimization results, and looked at the plots of the metric w.r.t. changing parameters. These plots were smooth, which suggests that the optimal values found are the correct ones. Additionally, the metric only slight changes over several parameter settings, which indicates that the algorithm outcome does not strongly depend on the exact values of the parameters. Fig. 2.6a is an example of diffusion filters with respect to number of iterations while the other parameters are selected at the optimal parameter, which demonstrates the latter effect. Fig. 2.6b and Fig. 2.6c demonstrate an effect of optimal and non-optimal settings. All parameter combinations evaluated are listed in Table 2.8, and the optimal parameter values are listed in Table 2.1.

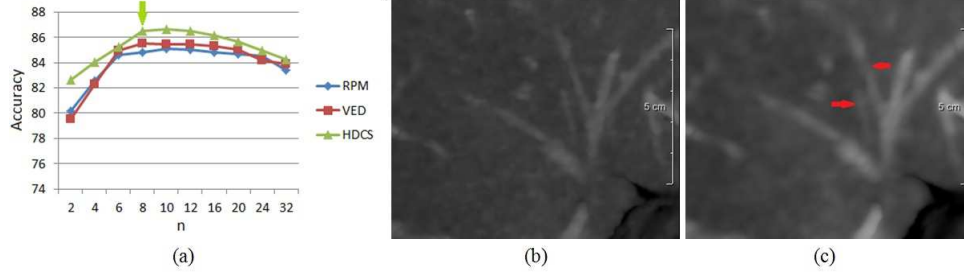


Figure 2.6. An example of parameter optimization: (a) accuracy (in %) of the diffusion filters with respect to number of iterations; (b) VED at iteration $\eta = 8$ (the optimal parameter); (c) VED at iteration $\eta = 32$: The effect that small vessels are blurred out in case of too much diffusion.

Table 2.1. The optimal parameters settings for the filters

Filters	Abbr	Optimal Parameters
Frangi's vesselness	Frangi	$\alpha=0.5$; $\beta=0.5$; $\gamma=30$; $\sigma_{min}=1$; $\sigma_{max}=4$; $v=5$
Sato's vesselness	Sato	$\alpha_1=0.3$; $\alpha_2=1$; $\sigma_{min}=1$; $\sigma_{max}=4$; $v=5$
Erdt's vesselness	Erdt	$\sigma_{min}=1$; $\sigma_{max}=4$; $v=5$
Regularized Perona-Malik	RPM	$\tau=0.0625$; $\eta=12$; $\lambda=10$; $\sigma=1$
Hybrid Diffusion filter with Continuous Switch	HDCS	$\tau=0.0625$; $\eta=8$; $\lambda_c=15$; $\lambda_e=10$; $\lambda_h=10$; $\alpha=0.001$; $\sigma=1$; $\rho=1$
Vessel Enhancing Diffusion	VED	$\tau=0.0625$; $\eta=12$; $\omega=25$; $s=1$; $\varepsilon=0.01$; $\sigma_{min}=1$; $\sigma_{max}=4$; $v=5$; $\alpha=0.5$; $\beta=0.5$; $\gamma=30$

2.3.3 Testing and Results

We applied the filters on the remaining 41 test datasets with the optimal parameters listed in Table 2.1. The results of the overall performance are summarized in Fig. 2.7.

Paired T-tests were used to determine whether the differences in performance between the filters were statistically significant. The tests between the segmentations with and without filtering are one-tailed, because we expect the accuracy to improve after filtering. When comparing the accuracies of two filters, we used two-tailed paired T-tests. The test results are shown in Table 2.2.

From Table 2.2 we can see that all of the six filters statistically significantly improved accuracy of the segmentation. In addition, it also shows that HDCS performed slightly better than the other filters.

We also investigated whether there is a relation between the noise level of the dataset and segmentation result where we use contrast-to-noise (CNR) as quantifica-

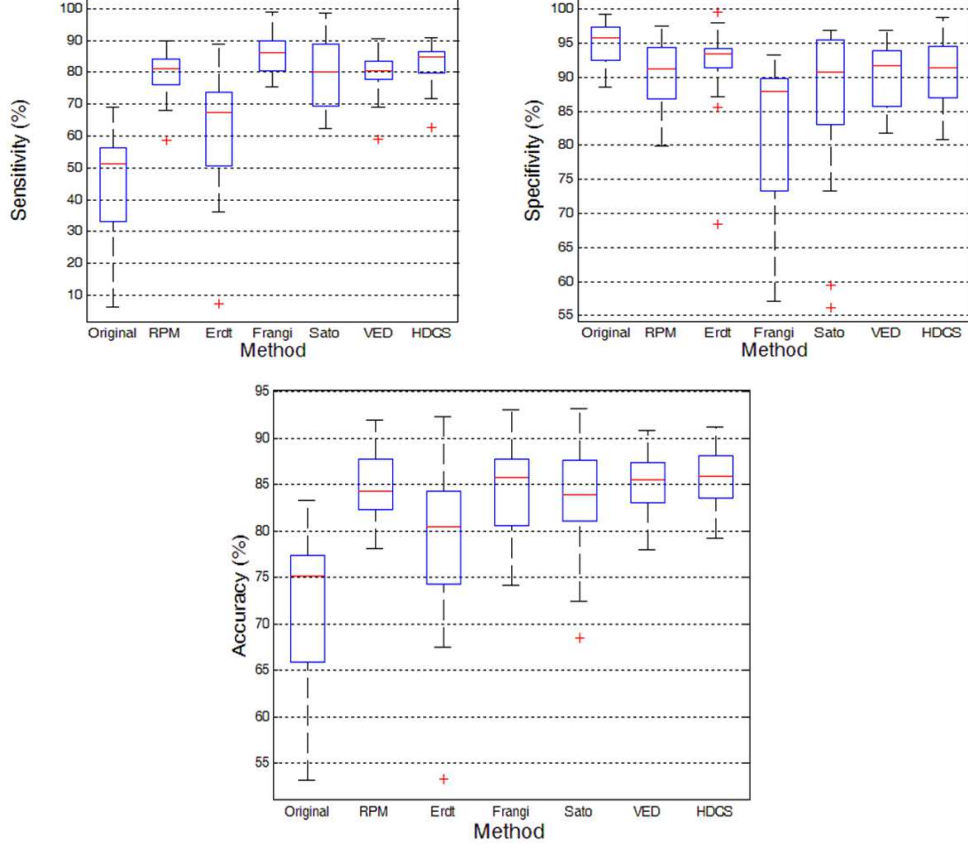


Figure 2.7. Box plot shows segmentation evaluation of the filters on the test datasets: top left visualizes the sensitivity; top right shows the specificity and bottom shows the accuracy score.

tion for the noise level. The CNR of each dataset is determined as follows:

$$CNR = 20 * \log \frac{\mu_v - \mu_b}{\sigma_b}, \quad (2.10)$$

where μ_v and μ_b are averages of voxel intensities at the vessel markers and the background markers respectively, and σ_b is standard derivation of voxel intensities at the background markers.

The original dataset is divided into two groups, based on CNR. We used the threshold of 4 dB, resulting in a low CNR group (< 4 dB) and a high CNR group (> 4 dB). Table 2.3 lists the segmentation scores of all filters, grouped on CNR level. Statistical significance of the difference in performance for low and high noise levels is evaluated with a two-group T-test. The segmentations on the original datasets and the Erdt filtered datasets are statistically significantly different for the low and the high CNR groups.

Table 2.2. Paired T-test filter’s segmentation accuracy. The bold p-values indicate that differences are statistically significant ($p < 0.05$).

Filters	RPM	Erdt	Frangi	Sato	VED	HDCS
Original	1.4E-08	1.3E-06	2.6E-10	2.3E-09	2.9E-09	1.5E-09
RPM		9.1E-05	0.657	0.268	0.740	0.011
Erdt			4.6E-05	7.1E-04	7.2E-04	1.8E-04
Frangi				0.317	0.571	0.178
Sato					0.243	0.058
VED						0.033

From Table 2.3, we conclude that the performance of all filters (except one filter on low CNR datasets) is similar to the performance on high CNR datasets. The exception is the Erdt filter. We also conclude that the segmentation algorithm is sensitive to CNR, as the performance on the unfiltered datasets is different for the two groups.

Additionally, we investigated how the methods perform on the large vessels. As for most clinical applications, up to the third order branches vessel information is sufficient, we performed an evaluation for markers only in those branches which is around 30% of all landmarks. Statistical significance testing was again performed using paired T-tests. The results are in Table 2.3 and Table 2.4.

Table 2.3. Average accuracies and standard deviations for the vessel segmentation. The bold p-values indicate that differences are statistically significant ($p < 0.05$).

Filters	All vessel	Large vessel	Low-CNR	High-CNR	p -value
			3±1.4(dB)	6±1.3(dB)	1.0E-05
Original	73±7.0	74±10.1	70±6.8	76±5.8	0.019
RPM	85±3.4	95±4.3	84±3.8	86±2.9	0.233
Erdt	79±8.3	80±8.7	76±8.7	82±6.7	0.038
Frangi	85±4.8	92±4.0	83±4.2	86±5.0	0.094
Sato	84±5.8	89±6.2	84±4.2	84±6.8	0.443
VED	85±2.9	96±4.1	84±4.5	86±2.6	0.064
HDCS	86±2.8	96±4.8	86±3.2	87±2.3	0.325

From Table 2.3 (evaluation on all vessels and evaluation only on larger vessels), we can infer that all filters work better for larger vessels than for smaller vessels. Moreover, Table 2.4 indicates that, with larger vessel, diffusion filters work better than vesselness filters.

For the datasets in group C, we evaluate all vessels accuracy score and paired

Table 2.4. Paired T-test of accuracy score for large vessel segmentation evaluation. The bold p-values indicate that differences are statistically significant ($p < 0.05$).

Filters	RPM	Erdt	Frangi	Sato	VED	HDCS
Original	3.1E-05	0.020	3.6E-05	0.004	2.0E-05	6.1E-06
RPM		7.8E-04	0.024	0.002	0.075	0.64
Erdt			0.005	0.035	6.1E-04	4.1E-04
Frangi				0.001	6.4E-03	0.02
Sato					6.5E-04	0.004
VED						0.869

T-test between the two observers.

Table 2.5. Average accuracies and standard deviations for the vessel segmentation of the two observers

Filters	Observer 1	Observer 2	<i>p</i> -value
Original	75±4.4	74±4.6	0.789
RPM	84±3.5	85±3.7	0.771
Erdt	80±3.2	81±3.1	0.463
Frangi	82±2.5	84±4.0	0.298
Sato	82±3.4	83±3.6	0.643
VED	84±2.7	84±2.3	0.761
HDCS	84±2.6	85±2.9	0.765

From Table 2.5, we can conclude that HDCS has the highest accuracy score and the differences between both observers are not significant ($p > 0.05$). For each observer, we also use paired T-test to determine differences between each pair of results.

From both Table 2.6 and Table 2.7, we can conclude that diffusion filters perform better than vesselness filters. And there is not significant difference between the two observers.

2.4 Discussion

In this work, we investigated the effect of various vesselness enhancing filters and noise reducing filters on the segmentation of liver vessels in CTA images. The increasing awareness of radiation dose and efforts to reduce dose gives rise to more noisy images. Purpose of our work was to investigate the effect of image quality (CNR) on subsequent segmentation, and also to investigate to what extent filtering may improve segmentation results.

Table 2.6. Paired T-test of accuracy score of observer 1.

Filters	RPM	Erdt	Frangi	Sato	VED	HDCS
Original	3E-04	4E-03	5E-04	1E-03	2E-03	2E-04
RPM		2.6E-02	0.0567	2.7E-03	0.702	0.33
Erdt			3.8E-02	4.1E-02	2E-03	2E-03
Frangi				0.304	1.2E-02	5E-03
Sato					0.052	1.1E-02
VED						0.229

Table 2.7. Paired T-test of accuracy score of observer 2.

Filters	RPM	Erdt	Frangi	Sato	VED	HDCS
Original	4E-05	1E-03	7E-04	1E-04	3E-03	6E-04
RPM		3E-02	4.51E-02	4E-03	0.831	0.512
Erdt			0.073	0.283	1E-02	6E-03
Frangi				0.658	3.1E-02	1.3E-02
Sato					0.023	5.6E-03
VED						0.547

To this end, we implemented several well-known vessel filters. Examples of filtered images of one of our datasets are shown in Fig. 2.9. We can see that vesselness filters detect small vessels better than diffusion filters (see Fig 2.8). Vesselness filters give better contrast between vessels and background. However they are sensitive to strong edges, and thus enlarge liver boundaries and vessel boundaries which causes false positive segmentation. Also, they have reduced output at bifurcations which causes false negative segmentation. The liver boundary enhancement by vesselness filters also is stated in [54]. To reduce this artifact, in our experiment, we used a maximum scale of 4 mm as larger Gaussian kernel scales enhance the liver boundary more.

RPM reduces noise while suppressing low contrast vessels, which causes the segmentation result for this filter to lose some small vessels. VED and HDCS perform slightly better than RPM because they blur noise along the vessel rather than across the vessel surface. However, when increasing the number of diffusion iterations too much, all of these diffusion filters blur small vessels (see Fig. 2.6).

From the numerical results, we see that the filters based on diffusion perform slightly better than the vesselness filters for this task but the difference is not statistically significant. This may be caused by the fact that diffusion filters work better than vesselness filters with large vessels that have high contrast and clear boundaries. Furthermore, diffusion filters have better responses at bifurcations. Additionally, vesselness filters may be sensitive to noise when the noise has tube-like structures. However, this property also enables these filters to enhance low contrast vessels, which

is also demonstrated by the superior sensitivity of these filters (and the accompanying lower specificity). Diffusion filters are based on smoothing which cause low contrast vessels to disappear. Thus, vesselness filters are more suitable for low contrast, less noisy images and diffusion filters seem to be more suitable for high contrast range images, with high noise level.

In this study, we employed region growing as the core for liver vessel segmentation because it is not only simple to implement but also commonly used in the relevant studies as state-of-the-art (see section Introduction 2.1). Another advantage of this method is that it does not require good initialization. As in this study, we determine seed points inside liver vessels, then the segmentation is propagated based on the chosen threshold (see section Segmentation 2.2.3). The segmentation is evaluated based on landmarks (see Fig. 2.5). The distance of the outside markers to boundary of the vessels affects the accuracy score. However, in our protocol we place markers as close as possible to the vessel, and the inter-observer validation shows that there is no significant difference between the two observers.

Liver vessel segmentations for each of the different filters are illustrated in the third column in Fig. 2.8 and Fig. 2.9. Compared to segmentation of the original image, the segmentation results of the filtered images are better, not only in the number of segmented small vessels, but also in the smoothness of the vessel boundary. The final accuracy of the liver vessel segmentation using the HDGS filter in our study is $86 \pm 2.8\%$ (see Table 2.3). This is comparable to e.g. results by Alhonnoro *et al.* (2010) [90], who reported a hit rate of 87%. Note that their evaluation is based on only hit rate (sensitivity) and does not take false hit rate (specificity) into account. The Erdt vesselness filter performs differently from the other vesselness filters in terms of sensitivity and specificity. The explanation may be that this filter gives lower vessel response and large enhancement in areas near liver boundaries than the other filters. As a result, this filter segments fewer vessels and has a smaller true hit rate.

From the experiments with the CNR, it follows that liver vessel segmentation results on low and high CNR images are significantly different. This means that without filtering the liver vessel segmentation accuracy is sensitive to CNR. In contrast, liver vessel segmentation on the images filtered with diffusion filters do perform similarly for low and high CNR images. Numerically, with HDGS filtering, datasets in the CNR range of 3 ± 1.4 dB have a segmentation accuracy of $86 \pm 3.2\%$, while datasets in the CNR range of 6 ± 1.3 dB have a segmentation accuracy of $87 \pm 2.3\%$ (see Table 2.3). This demonstrates that, when combining with appropriate filtering, vessel segmentation on low CNR images performs similarly to vessel segmentation on high CNR images.

Depending on the specific application, either diffusion or vesselness filtering is recommended. For example in TIPS and RFA, surgery or liver transplantation, and in multi-modality image registration, where the larger vessels are more important than the small vessels, diffusion is preferred. In TACE, however, the small, low contrast vessels are more relevant; and then vesselness would be an appropriate choice.

A limitation of our study is that evaluation was carried out on datasets from a single center. However, as Hounsfield units are calibrated, we expect that similar results can be obtained with CT images acquired on scanners from other vendors. Another drawback of the study is that we only use the proposal segmentation method

for evaluating the six well-known filters. Evaluation using other liver segmentation methods such as graph cut, level-set which use intensity feature as region growing uses, may show similar results.

2.5 Conclusion

This paper introduced a quantitative evaluation of several well-known filters for liver vessels in CTA images. The evaluation of segmentation accuracy using the proposed segmentation method demonstrated that diffusion-based filters overall gave slightly better segmentation results than vesselness filters. In general, the Sato and Frangi vesselness filters have a higher sensitivity, but lower specificity than the Erdt vesselness and the diffusion-based filters. HDCS performed the best, but the differences with the other diffusion-based filters were not statistically significant. The experiments also demonstrated that the results of all filters except the Erdt vesselness were not sensitive to the noise level. Finally, to support future evaluations, the implementations of the filters, as well as the training images with ground truth, are publicly available at BGR liver CT database website.

Parameters design

The parameters settings are summarized in Table 2.8.

Table 2.8. The parameter settings for the filters

Filters	Abbr	Parameters
Frangis vesselness	Frangi	$\alpha=0.3, 0.5, 0.7$; $\beta=0.3, 0.5$; $\gamma=5, 10, 20, 30, 50, 80, 120, 160, 200$; $\sigma_{min}=1$; $\sigma_{max}=4$; $v=5$
Satos vesselness	Sato	$\alpha_1=0.3, 0.5, 1$; $\alpha_2=1, 1.5, 3$; $\sigma_{min}=1$; $\sigma_{max}=4$; $v=5$
Erdts vesselness	Erdt	$\sigma_{min}=1$; $\sigma_{max}=4$; $v=5$
Regularized Perona-Malik	RPM	$\tau=0.0625$; $\eta=2, 4, 8, 10, 12, 16, 20, 24, 32$; $\lambda=5, 10, 12, 14, 16, 18, 20, 25, 30, 80, 150$; $\sigma=0.5, 1$
Hybrid Diffusion filter with Continuous Switch	HDCS	$\tau=0.0625$; $\eta=2, 4, 8, 10, 12, 16, 20, 24, 32$; $\lambda_c=5, 10, 15, 20, 30$; $\lambda_e=5, 10, 15, 20, 30$; $\lambda_h=5, 10, 15, 20, 30$; $\alpha=0.001$; $\sigma=1$; $\rho=1$
Vessel Enhancing Diffusion	VED	$\tau=0.0625$; $\eta=2, 4, 8, 10, 12, 16, 20, 24, 32$; $\omega=8, 25, 32$; $s=0.5, 1, 2, 5$; $\varepsilon=0.01$; $\sigma_{min}=1$; $\sigma_{max}=4$; $v=5$; $\alpha=0.5$; $\beta=0.5$; $\gamma=10, 20, 30, 40, 80, 120, 160, 280$

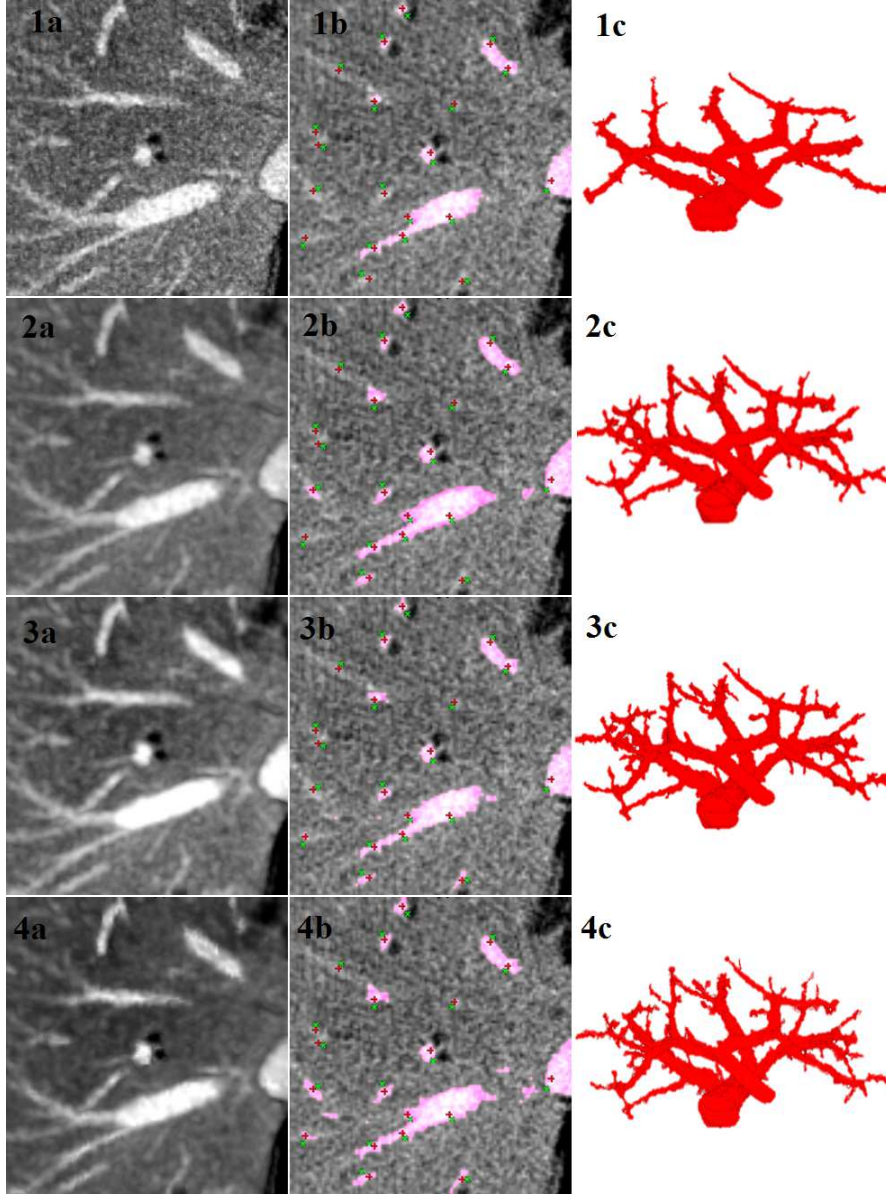


Figure 2.8. Filter responses and segmentations of the diffusion filters in column. Order from top to bottom are Original, RPM, VED, HDCS. The first column visualizes responses in 7 slice-slab maximum projection view; the second column shows projected 2D segmentations on one slice of the original image; the third column shows 3D segmentations. Numerical result of these datasets with sensitivity and specificity respectively: Original (65.4, 98.1), RPM (85.2, 92.6), VED (86.8, 93.4), HDCS (88.8, 92.7).

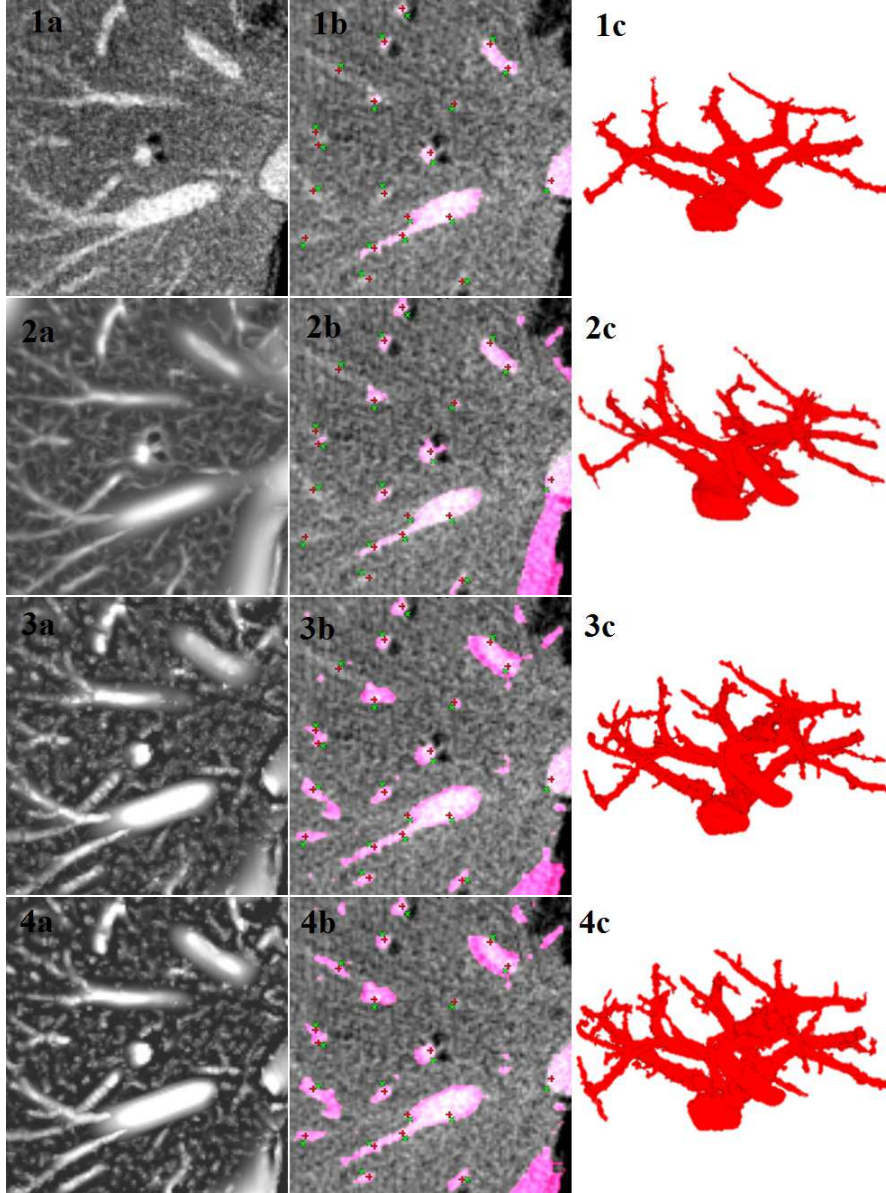


Figure 2.9. Filter responses and segmentations of the diffusion filters in column. Order from top to bottom are Original, Erdt, Sato, Frangi. The first column visualizes responses in 7 slice-slab maximum projection view; the second column shows projected 2D segmentations on one slice of the original image; the third column shows 3D segmentations. Numerical result of these datasets with sensitivity and specificity respectively: Original (65.4, 98.1), Erdt (82.4, 96.5), Sato (90.3, 88.5), Frangi (91.8, 87.6).

Non-rigid registration of liver CT images for CT-guided ablation of liver tumors

Abstract — CT-guided percutaneous ablation for liver cancer treatment is a relevant technique for patients not eligible for surgery and with tumors that are inconspicuous on US imaging. The lack of real-time imaging and the use of a limited amount of CT contrast agent make targeting the tumor with the needle challenging. In this study, we evaluate a registration framework that allows the integration of diagnostic pre-operative contrast enhanced CT images and intra-operative non-contrast enhanced CT images to improve image guidance in the intervention. The liver and tumor are segmented in the pre-operative contrast enhanced CT images. Next, the contrast enhanced image is registered to the intra-operative CT images in a two-stage approach. First, the contrast-enhanced diagnostic image is non-rigidly registered to a non-contrast enhanced image that is conventionally acquired at the start of the intervention. In case the initial registration is not sufficiently accurate, a refinement step is applied using non-rigid registration method with a local rigidity term. In the second stage, the intra-operative CT-images that are used to check the needle position, which often consist of only a few slices, are registered rigidly to the intra-operative image that was acquired at the start of the intervention. Subsequently, the diagnostic image is registered to the current intra-operative image, using both transformations, this allows the visualization of the tumor region extracted from pre-operative data in the intra-operative CT images containing needle. The method is evaluated on imaging data of 19 patients at the Erasmus MC. Quantitative evaluation is performed using the Dice metric, mean surface distance of the liver border and corresponding landmarks in the diagnostic and the intra-operative images. The results show that this is promising tool for liver image registration in interventional radiology.

3.1 Introduction

Primary liver cancer is one of the most fatal cancers. The 5-year survival rate of patients without treatment is 15 % [25,91,92]. So far, the preferred treatment is liver surgery. However, not all the patients are eligible for such an invasive procedure. Minimally invasive approaches such as radiofrequency ablation (RFA), microwave ablation, radiotherapy, chemoembolization, and high-intensity focused ultrasound are alternatives in case surgery is not an option [25,93]. In chemoembolization drugs are brought to the tumor via a catheter in the arterial system, and in case of ablation, a needle is introduced percutaneously into the tumor. Such treatments, being minimally invasive, require image-guidance during the intervention. These techniques are suitable for patients with tumors detected in early stages (< 3 cm in diameter) [93,94].



Figure 3.1. An example of intra-operative image, note the rotation of the patient required for safe needle insertion from the left side.

Contrast enhanced MRI or contrast enhanced CT is performed in the diagnostic phase, to assess the liver cancer stage [93,95] and to extract information such as tumor location and size. CT and US are commonly used during the ablations to guide the needle to the target tumor. Unfortunately, the tumor is not always visible using these imaging modalities. As a consequence, the interventional radiologist mentally maps the location of the tumor from the diagnostic (contrast-enhanced) images to the intra-operative images. This procedure is inconvenient, time-consuming and potentially inaccurate, as the human ability to mentally map a 3D object into a 3D space is limited [96,97]. Furthermore, after initial needle insertions, CT scans with a limited number of slices are acquired, to check the needle position that is advanced to the tumor step-wisely. The limited field-of-view (FOV) hampers accurate mentally mapping of the diagnostic information. Therefore, the purpose of our work is to improve image guidance by projection of the liver tumor during the intervention. This is achieved by semi-automatically spatially aligning the pre-operative contrast-enhanced CT image with the intra-operative CT images, such that the tumor can be visualized in the intra-operative CT images (see Fig. 3.1).

The challenges of spatially aligning (registering) diagnostic and intra-operative CT images are:

1. Deformations of the liver because of difference in patient pose
2. Change in position of the liver w.r.t. other organs because of respiration
3. Change of tissue surrounding the liver, e.g. changes in gallbladder filling or air in the intestines
4. Limited number of slices in the scans that are taken during needle insertion

Additionally, for our application, the registration should be sufficiently fast to be used in an interventional setting.

Some studies already reported on approaches to improve image guidance during ablations. Rieder et al. (2010) [98] developed a tool to segment the tumor in the intra-operative images. This method requires a contrast-enhanced acquisition to highlight the tumor and vessel. No quantitative evaluation results have been reported in their study and the use of contrast agent for imaging at the start of the intervention is generally not preferred, instead the contrast-enhanced acquisition is used to check the ablation or even cancelled in case of renal insufficiency. Archip et al. (2007) [99] introduced a registration framework using a finite element based method (FEM) to fuse diagnostic MRI to intra-operative CT of the liver for RFA. Elhawary et al. (2010) [95] used a non-rigid registration method with a B-spline based non-rigid transformation model to align diagnostic MRI image to intra-operative CT in cryoablation of liver tumors. To the best of our knowledge, there has been no study addressing the problem of registering diagnostic and intra-operative image data for the purpose of guiding needle insertion in ablation procedures using CT imaging only.

Our contribution thus is the development and evaluation of a method for improving image guidance in CT-guided ablation procedures by aligning pre-interventional diagnostic images with intra-operative images. This approach enables the integration of the tumor annotation from the diagnostic images in the intervention. To this end, we propose a two-stage non-rigid registration approach. The first stage is an initial registration, the purpose of which is to compute large deformations, including an optional user-guided refinement to locally improve the alignment. This registration approach allows for overlaying the tumor information in the initial CT scan made at the start of the intervention. In the second stage, the limited field-of-view intra-operative image with the needle in place is registered to the initial intra-operative CT image. Combination of the results of both stages enables tumor site integration in the limited field-of-view intra-operative images. The method is quantitatively evaluated on 19 datasets.

Organization of this chapter is as follows: in the next section, we introduce our method. Section 3.3 presents our experimental setup and the evaluation framework, as well as the results of our experiments. In Section 3.4, these results are discussed, and conclusions are drawn in Section 3.5.

3.2 Method

The data was anonymized and de-identified prior to analysis by Erasmus MC Institutional Data Access. All patients gave written informed consent. This retrospective study was approved by Erasmus MC Ethics Committee.

3.2.1 Image registration

Image registration is a powerful technique in medical image processing, and there are many publications on registration approaches and their application to specific medical imaging problems [100–104]. In image registration, a spatial transformation between two images, the fixed (target) image and a moving (source) image is determined [105, 106]. Mathematically, it is commonly written as an optimization process which finds the transformation $\mathbf{T}(\mathbf{x}) = \mathbf{x} + \mathbf{u}(\mathbf{x})$ that relates the two images such that the transformed moving image $I_M(\mathbf{T}(\mathbf{x}))$ spatially matches the fixed image $I_F(\mathbf{x})$ at every position of \mathbf{x} , where a metric $M(I_F(\mathbf{x}), I_M(\mathbf{T}(\mathbf{x})))$ is used to quantify the quality of the match. Several transformation models can be used for the transformation $\mathbf{T}(\mathbf{x})$, ranging from simple translation via rigid and affine to high-dimensional non-rigid transformation models. For 3D non rigid registration, a common representation of the deformation field $\mathbf{u}(\mathbf{x})$ is a cubic B-spline [101, 105] which is parameterized by parameter vector $\boldsymbol{\mu}$.

The metric M is often a similarity metric; Mutual information (MI) and normalized cross correlation (NCC) are typical metrics used in a cost function. In most cases, metrics are negated to obtain a dissimilarity metric, and the registration is turned into a minimization problem. Registration thus can be viewed as finding the set of the parameter $\hat{\boldsymbol{\mu}} = \arg \min_{\boldsymbol{\mu}} C(\boldsymbol{\mu}; I_F, I_M)$ where $C(\boldsymbol{\mu}; I_F, I_M)$ is the cost function related to the similarity metrics [105].

3.2.2 Two-stage registration approach

In clinical practice of CT-guided percutaneous ablation, the interventional radiologist acquires a CT scan of the complete liver at the start of the intervention to determine the target location, and to determine the entrance point of the needle on the patients skin. Subsequently, during needle introduction, CT-images with a limited number of slices are acquired to assess the position and orientation of the needle. Based on this workflow, we propose to register the diagnostic image to the CT image with needle in situ in two stages: first the diagnostic image (D) is registered to the first complete liver operative image (F), which enables integration of the tumor in the planning CT image, and subsequently the initial operative image is registered to the limited field-of-view image with the needle (N), (see Fig. 3.2). The main reason for this two-step approach is that achieving a direct registration of the image with needle to the diagnostic image is infeasible: differences in patient positioning and breathing state require a non-rigid registration, and the limited field of view hampers an accurate direct registration directly to the diagnostic image. However, during the intervention, the patient is sedated and kept in a stable position, and breathing is shallow. So a rigid registration is sufficient to compensate the drift motion of the liver caused by

shallow breathing of patient during intervention. Pilot experiments showed that the CT image with the needle can be registered to the first operative CT image relatively easily. Non-rigid registration of image D to image N (NR: D-N) is performed by initializing with the combined result of a rigid registration of image F and image N (R: F-N) and a non-rigid registration of image D to image F (NR: D-F). In our study, we used MI as the metric to measure the image alignment, and also include a regularizer for the deformation field:

$$C(\boldsymbol{\mu}; I_F, I_M) = -MI(\boldsymbol{\mu}; I_F, I_M) + \alpha R(\boldsymbol{\mu}) \quad , \quad (3.1)$$

where $R(\boldsymbol{\mu})$ is a regularization term which constrains the non-rigid deformation and α is a weight term which balances the similarity metric $MI(\boldsymbol{\mu}; I_F, I_M)$ and the regularization term $R(\boldsymbol{\mu})$ [101, 107].

In practice, because the histogram is binned, the mutual information is defined as:

$$MI(\boldsymbol{\mu}; I_F, I_M) = \sum_{m \in L_M} \sum_{f \in L_F} p(\boldsymbol{\mu}; f, m) \frac{p(\boldsymbol{\mu}; f, m)}{p_F(f)p_M(\boldsymbol{\mu}; m)} \quad , \quad (3.2)$$

where L_F and L_M are sets of regularly spaced intensity bins of histograms of the fixed image and the moving image correspondingly; p is the discrete joint probability of the image intensities of the two images; p_F and p_M are the marginal discrete probabilities of the fixed image and the moving image intensities correspondingly.

Stage one: initial registration

The major challenge in this procedure is to accurately register the diagnostic image D with the initial intra-operative image F. Therefore, we propose a registration approach that permits user interaction to correct the registration. Initially, a non-rigid registration is applied to obtain alignment. The registration method uses a liver mask which covers the liver and excludes unrelated neighbouring organs such as the heart, the lungs, etc. from the registration. Incorrect registrations, with unrealistic deformation, may occur in this registration because of the large pose changes and changes in breathing state between the diagnostic and intra-operative images, especially near the liver boundary (see Fig. 3.3).

For the registration, we used the framework of a previous study, where pre- and post-interventional images were registered for therapy assessment [108]. The framework performs registration in a multi-resolution strategy; however, in contrast to our previous work, we now choose MI as similarity metric because the intra-operative images are often non-contrast enhanced.

3.2.3 Stage one: user-guided refinement

An optional user-guided registration step may be applied next to further improve the registration. The user may annotate the region of incorrect registration by clicking one or more points in the region in the diagnostic image where the incorrect deformation occurs. In practice, these regions have a large non-rigid deformation component, and the refinement method is focused on reducing this erroneous non-rigid deformation. The annotated points serve as seed points for a subsequent dilation (1x1x1 cm kernel).

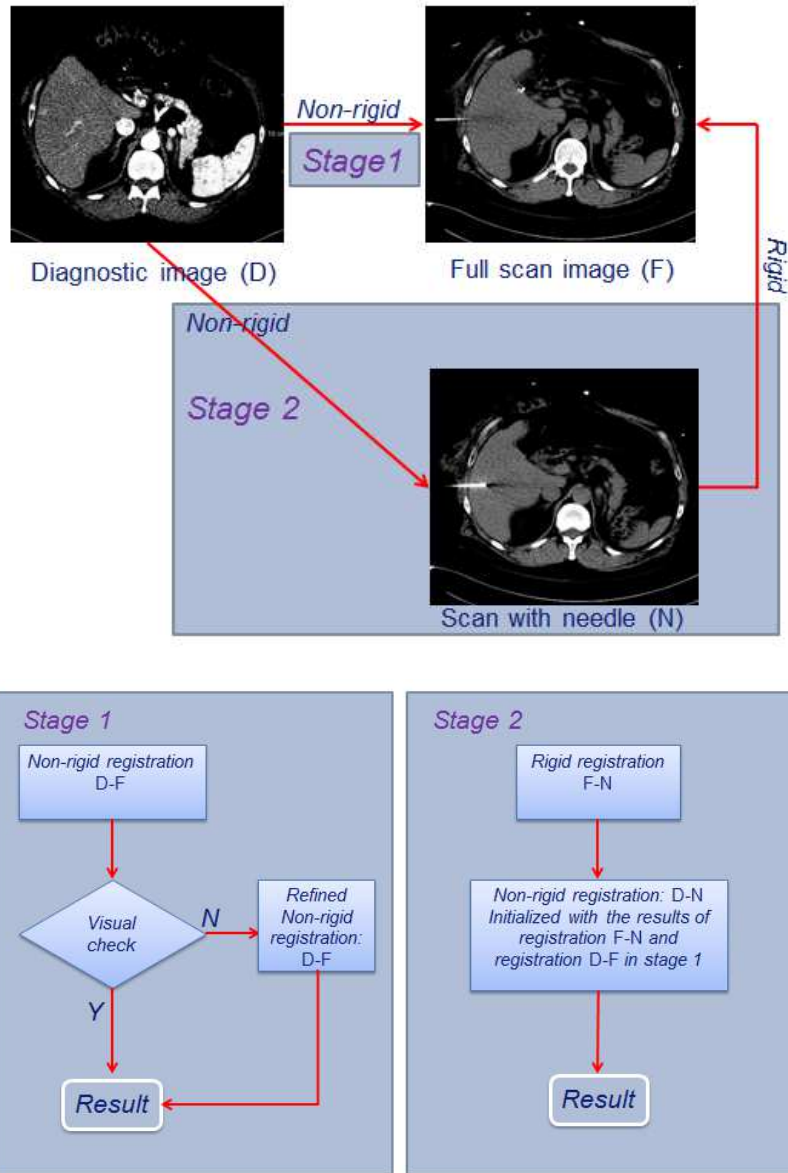


Figure 3.2. Registration scheme of the diagnostic contrast enhanced CT image D and the intra-operative CT images: stage 1 is registration between the image D and the full operative image F; and stage 2 is the registration between the image D and the operative image N.

The combined dilated regions form the area C , which is used as a coefficient mask in the registration, i.e. non-rigid components in the transformation inside the area C are penalized by using the local rigidity term introduced by Staring et al. (2007) [107], and also recently adapted in previous work [108] to improve the smoothness of the transition areas between local rigidity areas and non-rigid transformation areas. Specifically, the regularization term $R(\boldsymbol{\mu})$ in equation 3.1 is replaced by the following term, which is defined locally by coefficient mask C :

$$\mathcal{P}^{rigid}(\mathbf{T}_{\boldsymbol{\mu}}; I_M) = \frac{1}{\sum_{\mathbf{x}} c(\mathbf{T}_{\boldsymbol{\mu}}(\mathbf{x}))} \times \sum_{\mathbf{x}} c(\mathbf{T}_{\boldsymbol{\mu}}(\mathbf{x})) \times \left\{ c_{AC} \sum_{k,i,j} AC_{kij}(\mathbf{x})^2 + c_{OC} \sum_{i,j} OC_{kij}(\mathbf{x})^2 + c_{PC} PC(\mathbf{x})^2 \right\}, \quad (3.3)$$

where the weights c_{AC} , c_{OC} and c_{PC} balance the three terms: affine term $AC_{kij}(\mathbf{x})$, orthonormality term $OC_{kij}(\mathbf{x})$ and properness term $PC(\mathbf{x})$; and $c(\mathbf{x}) \in [0, 1]$ is a user-predefined coefficient of mask C at location \mathbf{x} .

3.2.4 Stage two: non-rigid intra-operative image registration

In stage two, the intra-operative image with the needle N is rigidly registered to the full intra-operative image F. Both the diagnostic image and the limited field-of-view image are registered to the full intra-operative image. In order to avoid an accumulation of registration errors, a non-rigid registration is subsequently applied to register the diagnostic image to the intra-operative image with the needle. Note that, after initial alignment using transformation from the registrations, the diagnostic image and the intra-operative image with the needle are already relatively well spatially aligned, and thus a subsequent non-rigid registration is feasible. In case that the initial registration of image D and F needs a refinement registration, the annotated mask is also applied to the registration in stage two. The tumor annotated by using the diagnostic images is transformed to the intra-operative image with the needle by using transformation of the new registration, enabling an integrated visualization of the needle and the tumor area.

3.3 Experiments and Results

3.3.1 Image data

Abdominal diagnostic and intra-operative anonymized CT scans of 24 patients were randomly selected and from patients that underwent abdominal CT scanning and CT-guided RF ablation in the Erasmus MC in 2014 and 2015. All of the data were acquired by Siemen CT scan, 64-row multidetector, pitch 0.8, rotation time 0.5s. From the diagnostic scans, the contrast enhanced images were selected for the study. The images have a resolution of 0.56 mm x 0.56 mm to 0.89 mm x 0.89 mm, 1-10 mm slice spacing, 1-2 mm slice thickness, 512x512 pixel in plain resolution. Image acquisitions

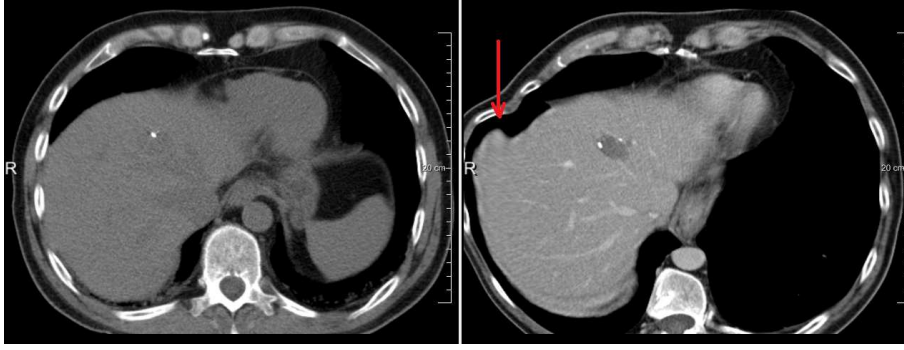


Figure 3.3. Example of incorrect deformation at the edges of the liver in case the liver boundary in the intra-operative image (left) is unclear. The arrow points to the region with incorrect deformation in the transformed pre-operative image (right).

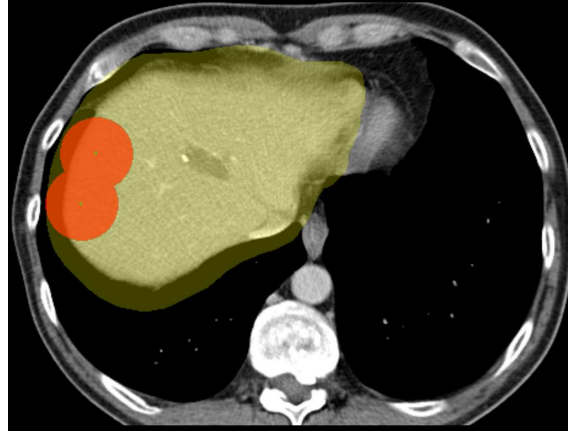


Figure 3.4. The coefficient mask (in red) is used to penalize the rigid deformation of the liver inside the liver mask (in yellow).

were performed according to the standard clinical protocol: 60 seconds after the injection of 120 cc intravenous contrast agent. The intra-operative images were acquired with a tube voltage of 100-120 KV and a tube current of 172 - 288 mAs. Of these images, 13 are non-contrast enhanced images; 11 are with contrast enhanced with 80-120 cc intravenous contrast agent; and slice spacing is 2.5-5 mm. The main reason for the contrast enhanced images is the inability to mentally match tumor location on non-contrast CT with previous contrast enhanced diagnostic CT. Furthermore, in 12 out of the 24 cases, the patient was rotated (30-50 degrees) w.r.t. a supine position on the CT table, to provide access to the appropriate needle introduction site, see e.g. Fig 3.5. In general, the field of view of the 3D abdominal images is larger than the region of interest i.e. the liver. Hence, to reduce processing time for image registration, in a pre-processing step, we manually cropped the images to the

liver. We randomly picked five cases for pilot experiments, leaving 19 cases for the final analysis.

3.3.2 Manual segmentation of the tumor and liver mask

The liver tumor was manually segmented in the diagnostic image by initials of radiologist in brackets. The liver masks of the diagnostic image and the intra-operative image, which are used in the registration to limit the computation of the similarity metric to the liver region only, were annotated by drawing approximately 10 smooth contours slightly larger than the liver (see Fig 3.4). Note that the liver masks do not need to be accurate liver segmentations; automated liver segmentation methods [83] could be used as a substitute. Additionally, the liver was accurately segmented manually for evaluation purposes (see Section evaluation metric 3.3.4); this segmentation was not used in the method.

3.3.3 Registration software and parameter settings

In this study, we used Elastix, a open source registration software developed by Klein and Staring [105] which is available at elastix.isi.uu.nl. The parameter file of the registration can be found at the elastix database of parameter setting which contains the relevant parameter settings. The important settings are as following: If the patient on the CT table was rotated during the intervention, the images were manually rotated (along the z-axis) such that the spines on both images have approximately the same orientation. A multi-resolution approach was utilized to handle the variation in the size of the patients liver as well as image resolution. The initial alignment of registration is based on center of mass of the liver mask. The four resolutions of the B-spline grid are set to [80 40 20 10] mm. The weight parameters for rigidity are set as (RigidityPenaltyWeight 0.1 0.1 0.1 4.0), (LinearityConditionWeight 100.0), (OrthonormalityConditionWeight 1.0), (PropernessConditionWeight 2.0). The number of iterations for each resolution is set to 500 to ensure sufficient number of iterations for convergence. At each iteration, 2000 samples are randomly selected to compute the MI of the fixed and the moving image. A stochastic gradient descent optimizer is used to find the optimal parameter $\hat{\mu}$ of the B-spline transformation field, which defines the best transformation of the moving image (the diagnostic image) to the fixed image (the intra-operative images). The registration is performed on an AMD Opteron core, 2.8GHz, 64 GB RAM on a Linux cluster.

3.3.4 Evaluation metrics

Three quantitative metrics were used to evaluate the accuracy of registration method. The first metric is the Dice coefficient which measures the overlap between a segmentation of the liver in the diagnostic image and that in the intra-operative image after the registration. The segmentation of the liver in the diagnostic image is transformed to the intra-operative image using the transformation result of the registration. The

Dice similarity coefficient (DSC) is computed as follows:

$$\text{DSC}(X, Y) = 2 \frac{|X \cap Y|}{|X| + |Y|} \quad , \quad (3.4)$$

where X and Y present the two segmentations, and $|\cdot|$ denotes the number of voxels inside the segmentation. Secondly, we use the mean surface distance in 3D (MSD) to evaluate the distance between the surfaces of the liver segmentations after registration. The MSD is defined as follows:

$$\text{MSD}(X, Y) = \frac{1}{(n_X + n_Y)} \left(\sum_{i=1}^{n_X} d_i + \sum_{j=1}^{n_Y} d_j \right) \quad , \quad (3.5)$$

where n_X and n_Y represent the number of voxels on the two segmentation surfaces correspondingly, and d_i , d_j are the closest distances from each voxel on the surface to the other surface. In practice, the surface is determined by eroding with a kernel of one voxel.

In order to measure the accuracy of the registration inside the liver, corresponding landmarks are used as the third evaluation metric. 10-15 pairs of anatomical landmarks at the corresponding liver vessels (in case the intra-operative image has contrast agent) and surgical clips are annotated by two experts (radiologists). After registration, the mean corresponding distance (MCD) between the transformed points and the corresponding points is calculated as follows:

$$\text{MCD}(A, B) = \frac{1}{n} \left(\sum_{i=1}^n |a_i - T(b_i)| \right) \quad , \quad (3.6)$$

where n is number of pairs of landmarks; a_i and b_i denote landmarks in diagnostic image A and intra-operative image B correspondingly; and T is the transformation from image B to image A .

The first stage (non-rigid) registration is the most challenging in our approach; all three metrics are used to evaluate this registration. Additionally, the DSC and MSD metrics are used for the limited field-of-view intra-operative images; MCD was not possible for these images, because of a lack of suitable landmarks.

3.3.5 Registration results

In a first experiment, we evaluate the registration performance of the first stage, i.e. the diagnostic CT image to the initial intra-operative image (the method described in section II) using the parameters described in section III.C. A pilot experiment was performed on the 5 random data sets with visual evaluation; and subsequently, we ran the software with fixed parameter settings on the 19 remaining data sets. In 13 of 19 cases the first stage registration was sufficiently accurate (determined by visual inspection with the $\text{DSC} > 80\%$ and $\text{MCD} < 10$ mm). The mean accuracy of registration of the successfully registered 13 cases is summarized in Table 3.1. The refinement step was applied on the remaining 6 cases. A user annotated 2 - 3 points to define the mask C (see Fig. 3.4), which took around 1-2 minutes on average. Using

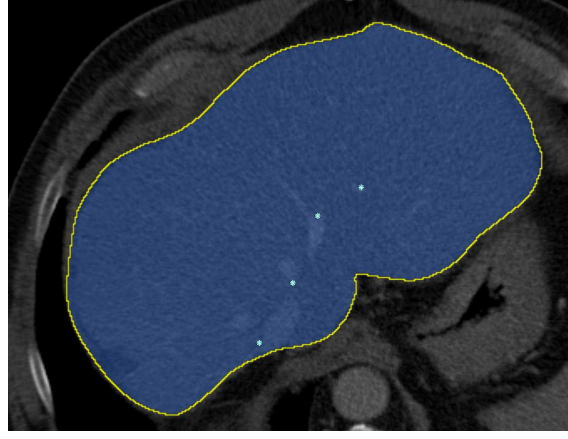


Figure 3.5. The manual liver segmentation and the landmarks inside the liver.

this user input, an additional three cases were successfully registered. The evaluation result of these 3 cases using the metrics in section Evaluation metric 3.3.4 (DSC, MSD, and MCD) is shown in Table 3.1. The remaining three cases remain with the DSC are lower than 80% are unsuccessfully registered. All of the three cases have large rotation (> 50 degree). Two examples of successful registrations in the first step are shown in Fig. 3.6; an example of successful registration in the second step is shown in Fig. 3.7; and an example of unsuccessful registration is shown in Fig. 3.8.

A t-test between the registration accuracies in the two groups, non-contrast enhanced group (9 cases) and contrast enhanced group (7 cases), using DSC and MSD gave p-values 0.16 and 0.22 correspondingly, showing that there are no statistically significant differences between the two groups. A t-test on the registration accuracy between the rotation group (6 cases) and non-rotation group (10 cases) 0.002 For DSC, 0.0018 for MSD, demonstrating that rotation has significant influence on the registration accuracy. Next, we ran the second stage, i.e. the rigid registration between image F and image N followed by a non-rigid registration between image D and image N, which as initialized with the combined results of the registrations of image D to image F and image F to image N. This was only performed on the 16 datasets that successfully registered in the first stage. The results of this second stage registration are in Table 3.2, as well as the results if the second stage was left out, i.e. if image F and image N were concatenated, without a subsequent registration and. An example of registration of the diagnostic image to a sequence of intra-operative images is shown in Fig. 3.9.

3.3.6 Intra-observer variation

We also investigated the intra-observer variation in manually annotating the landmarks. This was done on the 11 datasets with contrast agent. To this end, the observers were asked to repeat their annotation in the interventional image, after presenting them the annotated landmark in the diagnostic image. The average distance

Table 3.1. Registration evaluation 16 cases in the first stage.

	13 cases	3 cases		All 16 cases
Metric	Non-rigid	Non-rigid only	Refined Non-rigid	Non-rigid
DSC (%)	91 \pm 2.8	71.6 \pm 14	90 \pm 2.1	90 \pm 2.9
MSD (mm)	4.4 \pm 1.5	11.3 \pm 4.2	5.1 \pm 2.4	4.6 \pm 1.8
MCD (mm)	4.7 \pm 1.9	10.2 \pm 4.6	6.4 \pm 3.8	5.3 \pm 2.5
Running time (min)	10-15	10-13	20-25	10-25

Table 3.2. Registration evaluation of 16 cases in the second stage.

Metric	Concatenated only	Non-rigid
DSC (%)	83.9 \pm 7.5	90.1 \pm 3.6
MSD (mm)	6.8 \pm 4.2	5.2 \pm 2.6
Running time (min)	7-15	12-21

between the original and repeated landmark annotations were 1.9 mm and 2.1 mm for both observers respectively.

3.4 Discussion

In this study, we investigated a non-rigid registration framework to align diagnostic CT images to intra-operative CT images for CT-guided RFA of liver tumors. To be able to deal with intra-operative images with only a few slices, the registration was performed in two stages: a first stage in which the full diagnostic image was non-rigidly registered to the first intra-operative CT image, and a second stage where this registration, and a rigid registration between the first and current intra-operative image, were used to initialize a non-rigid registration between the diagnostic and current intra-operative image. The method also allows for manual interaction in case the non-rigid registration in the first stage did not give a good alignment. The approach was evaluated on 19 clinical datasets using three different metrics: DCS, MCD and MCD and compared with rigid registration method (see Table 3.1 and Table 3.2). The results show that the proposed method achieved better registration accuracy than rigid registration. 13 of 19 cases were successfully registered (68%) without any correction, and another 3 were successfully registered using the user-defined local rigid areas, which improved the successful rate of registration to 84%. After correction, DSC was 90%, and MSD 5.1 mm and MCD were 6.5 mm. The 3 remaining cases, where the registration method failed to accurately register the images, are the cases with large liver deformation, caused by large rotation. The DSC of these three cases are 48%, 76% and 79%. The following intra-operative image registration resulted in a DSC of 90% and MSC of 5.2 mm, which shows that the largest registration errors are made in stage 1, and that no large errors are introduced in the second stage.

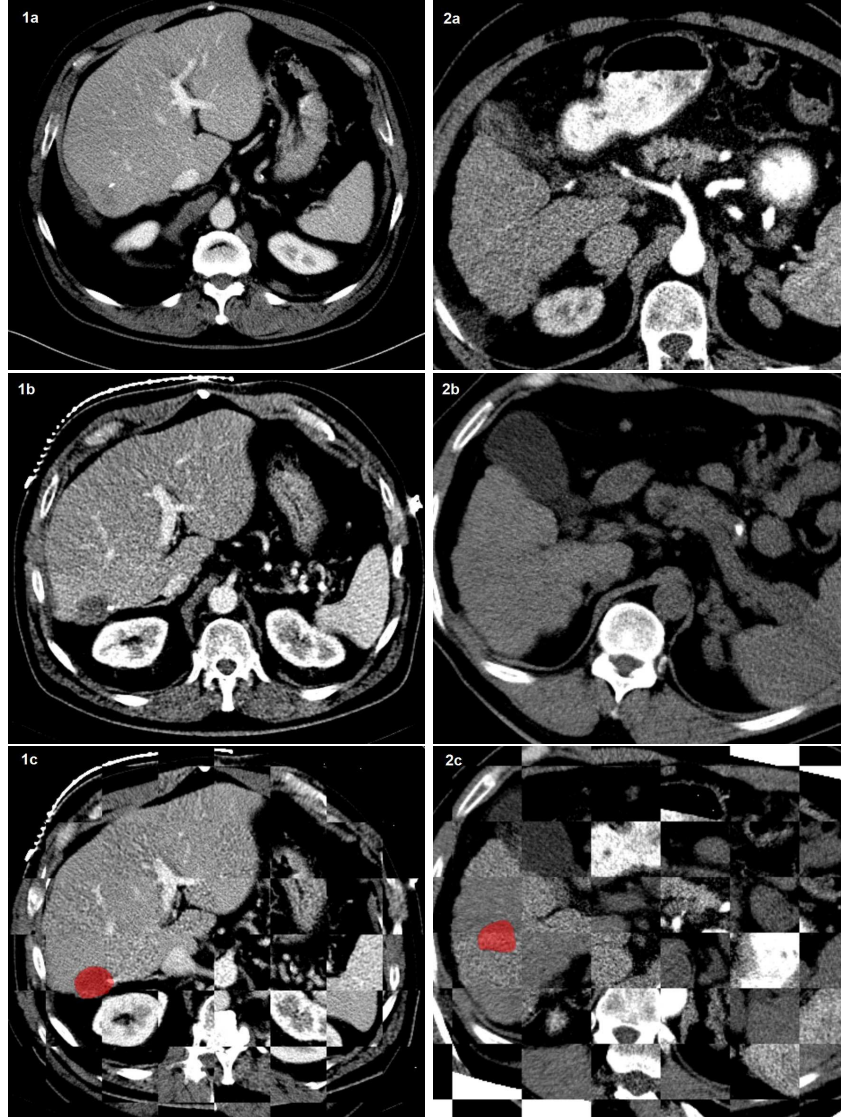


Figure 3.6. Two examples of successful registrations between diagnostic image and intra-operative image with the tumor (in red): The top row shows the diagnostic images; the second row shows the intra-operative images; the third row shows the fused images. The left column is an example of a contrast enhanced intra-operative image and the right column is an example of a non-contrast enhanced intra-operative image with 30 degree-rotation. The registration method only computes the metric within the liver, thus the images do not match outside the liver.

When only the rigid registration from stage 2 is used, the DSC is 84% and MSC is 6.8 mm, which indicates that the non-rigid registration is required. The T-tests

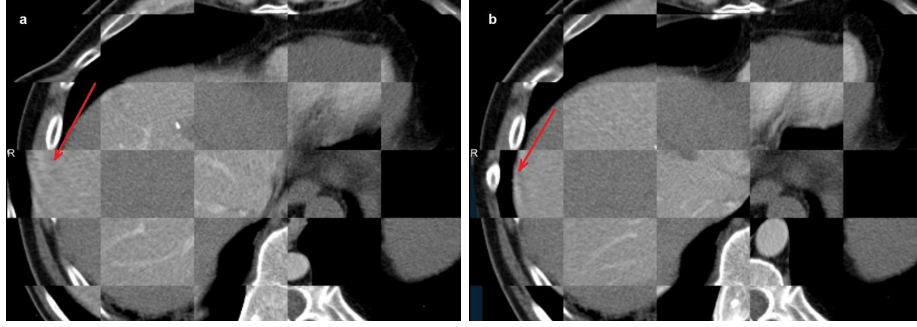


Figure 3.7. The effect of the rigidity term (from Eq.3.1) a) Registration without rigidity constrain, yielding large incorrect deformation (red arrow). b) Registration with rigidity constrain in the refined stage.



Figure 3.8. Example of an unsuccessful registration.

in section 3.3.5 indicate that rotation affects the registration accuracy significantly and the contrast agent does not have a significant impact on the registration result in other words, contrast agent might be omitted with this technique. Note that the clinical motivation for rotating the patient is to have sufficient access for e.g. ultrasound imaging, when using CT only, rotation is much less frequently required. For prospective evaluation of the proposed method, the number of cases with rotation can be decreased, and thus the success rate may be increased.

Interpretation of the error metrics should be done with care. First, the relatively large slice thickness of the CT datasets will lead to discretization effects in the error of the landmark annotation. Additionally, the intra-observer variation of approximately 1.9 mm and 2.1 mm demonstrates the difficulty in pinpointing landmarks for the evaluation, and is also a quantification of the in-plane error of the annotations. Both the in-between slice discretization error and the intra-observer error will be part of the registration error quantification, which is also confirmed by the visual inspection, which shows well aligned livers. Therefore, also taking into account the

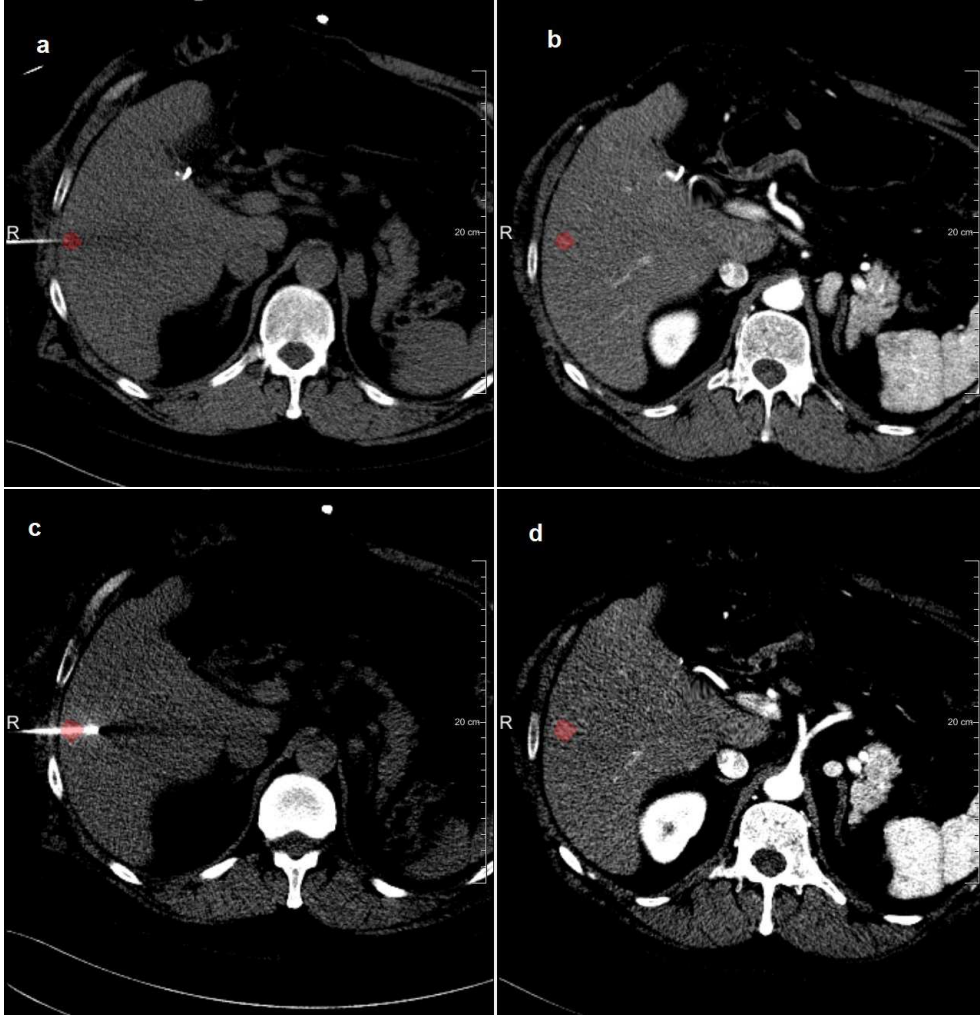


Figure 3.9. Example of tumor visualization in the intra-operative image after registration to the diagnostic image with the tumor (in red): a) the initial intra-operative image; b) the transformed diagnostic image to the initial intra-operative image; c) the next frame of intra-operative image; d) the transformed diagnostic image to the current intra-operative image.

commonly used ablation margin of 10 mm in clinical practice, we are convinced that the registration-based integration of the diagnostic information in the intervention is a valuable add-on to the current practice of CT-guided RFA. Compared to other studies on registration of liver images our study has comparable results. Elhawary et al (2010) registered diagnostic contrast-enhanced MRI to intra-procedural CT of the liver in cryoablation. A TRE accuracy of 4.1 mm and a DSC of 97% were reported. Our TRE of corresponding landmarks is 5.3 ± 2.5 mm, and our DSC is $91 \pm 2.9\%$.

Note that our intra-operative images were acquired with lower tube current and tube voltage. Comparing these results to our previous study using the same framework with the pre-operative RFA image and the post intra-operative RFA image, which has a DSC of 92.2%, a mean distance between the liver segmentation boundaries of 2.51 mm and a MCD of 2.91 mm, we conclude that registration to the intra-operative images is more difficult. The less protocolized imaging (no breath-hold), lack of contrast agent and patient rotation may be the cause of these differences.

Our study has some limitations. First, we only use data from a single center with limited number of CT scanners. We are, however, confident that similar results will be obtained using imaging data from other CT system vendors, as image acquisitions are protocolized, and Hounsfield units present physical properties. Second, because of limited size of the intra-operative images with the needle in place, we were not able to annotate landmarks to be used for the evaluation. However, based on the visual alignment of the liver boundary (see Fig 3.9 for an example), we expect that the accuracy of the registration is similar to the accuracy of registration between diagnostic image and the initial intra-operative image.

Finally, the registration running time is from 7 to 20 minutes which is insufficiently fast for direct use in clinical practice. This problem can be solved by using multi-threaded programs and/or using GPU. In the future, we intend to investigate more semi-automatic approaches that may be used to address the unsuccessful registration, and also we intend to evaluate the registration framework in a prospective interventional setting.

3.5 Conclusion

In conclusion, we have developed and evaluated a two stage registration approach to align diagnostic CT images to intra-operative CT images for CT guided liver cancer RFA treatment. The method had a success rate of 84%, a registration accuracy of 91% in terms of DSC, 4.6 mm in MSD and 5.3 mm in MCD. These results show that the registration approach is a promising tool for improving RFA needle positioning in minimally invasive treatment of liver cancer.

Semi-automated registration of pre- and intra-operative liver CT for image-guided interventions

Abstract — Percutaneous radio frequency ablation is a method for liver tumor treatment when conventional surgery is not an option. It is a minimally invasive treatment and may be performed under CT image guidance if the tumor does not give sufficient contrast on ultrasound images. For optimal guidance, registration of the pre-operative contrast-enhanced CT image to the intra-operative CT image is hypothesized to improve guidance. This is a highly challenging registration task due to large differences in pose and image quality. In this study, we introduce a semi-automated registration algorithm to address this problem. The method is based on a conventional nonrigid intensity-based registration framework, extended with a novel point-to-surface constraint. The point-to-surface constraint serves to improve the alignment of the liver boundary, while requiring minimal user interaction during the operation. The method assumes that a liver segmentation of the pre-operative CT is available. After an initial nonrigid registration without the point-to-surface constraint, the operator clicks a few points on the liver surface at those regions where the nonrigid registration seems inaccurate. In a subsequent registration step, these points on the intra-operative image are driven towards the liver surface on the pre-operative image, using a penalty term added to the registration cost function. The method is evaluated on five clinical datasets and it is shown to improve registration compared with conventional rigid and nonrigid registrations in all cases.

4.1 Introduction

Percutaneous radio frequency ablation (RFA) is a treatment method for non-resectable hepatic tumors [109]. RFA is a minimally invasive treatment that is often performed under CT image guidance if the tumor is not visible with ultrasound imaging [110]. In the diagnostic phase, a pre-operative contrast-enhanced liver CT images (PRE), which visualize the liver anatomy and tumor location/size well, is acquired. Intra-operative CT (INTRA) has typically different image quality, due to practical/logistical reasons, but provides an up-to-date image of the liver and needle position. INTRA imaging done prior to and during needle insertion is often not contrast-enhanced, since it is preferred to use contrast imaging for visualization of the ablation zone after the ablation to assess treatment success [110, 111]. The tumor is therefore not well visible in the INTRA images.

It is hypothesized that an accurate registration of the PRE image to the INTRA image may improve image guidance, as it enables the localization of the tumor in the registered contrast-enhanced PRE images. Such a registration is highly challenging because the liver is a mobile organ and its location and shape are affected by the patients breathing and pose. Note that in our hospital patients are sedated during these interventions, thus breath-hold imaging intra-operatively, as it is commonly done for the diagnostic images, is not feasible. Additionally, during RFA, the patient might lie on his/her side in a rotated position, to facilitate needle insertion, whereas the PRE CT is acquired in supine position (patient lying on the back), causing large deformations between the PRE and INTRA images. The purpose of this work is, therefore, to develop and evaluate a robust method for registration of PRE and INTRA liver CT images that could be used during RFA interventions. Initial experiments on representative data suggested that a conventional fully automated nonrigid registration approach (based on B-spline deformations and maximization of mutual information or normalized correlation coefficient) [105, 108, 112] does not provide satisfactory results in all cases, even after extensive parameter tuning. Therefore, we decided to pursue a semi-automated approach. A large amount of user interaction during the intervention is highly undesirable. However, in the PRE stage, there is sufficient time for elaborate pre-processing. Based on these requirements, we have designed a semi-automated registration method with limited user-interaction during the intervention.

4.2 Method

The proposed method is meant to be used when a conventional nonrigid registration does not generate satisfactory results. The proposed registration workflow is as follows. As a first step, a rigid registration is done. Following that, a conventional non-rigid B-spline registration is performed. Using the resulting transformation, the PRE image liver segmentation obtained before the intervention is deformed to the INTRA image domain and shown along with the INTRA image. Based on this visualization, the operator inspects the registration quality and identifies regional registration failures. If the registration result is found to be satisfactory, no further improvement is needed and the intervention can proceed with the current registration. In cases the

registration result of this first stage is deemed not sufficiently accurate, for example due to large deformation of the liver between the PRE and INTRA image [108], a semi-automated approach, presented in what follows, is pursued.

The proposed method is based on a conventional automated intensity-based registration framework [105, 112], which we extended with a novel point-to-surface constraint. The point-to-surface constraint aims at obtaining an accurate match between the liver organ boundaries on INTRA and PRE images. A full PRE image liver segmentation is assumed to be available. It can be obtained prior to the intervention and thus does not inflict a burden during the intervention. For the INTRA image, there is insufficient time during the intervention to manually perform a full liver segmentation. We therefore only require the human operator to annotate a few points on the liver boundary near the regions where nonrigid registration appears to not give satisfactory result after the visual evaluation. Then, after initialization with the previous unconstrained rigid registration, the proposed nonrigid registration with point-to-surface constraint is executed.

In the registration, INTRA and PRE images are used as fixed and moving images, respectively, since the PRE image needs to be transformed to the INTRA image domain. Let us define the fixed INTRA image, the moving PRE image and a parameterized coordinate transformation that maps points from the fixed to the moving image domain as $F(\mathbf{x}) : \Omega_F \subset \mathbb{R}^D \rightarrow \mathbb{R}$, $M(\mathbf{x}') : \Omega_M \subset \mathbb{R}^D \rightarrow \mathbb{R}$ and $T_{\boldsymbol{\mu}}(\mathbf{x}) : \Omega_F \rightarrow \Omega_M$ respectively. Here $\boldsymbol{\mu} \in \mathbb{R}^Q$ represents the Q -dimensional vector of transformation parameters, e.g. Euler angles and translations in case of rigid transformation and B-spline coefficients in case of nonrigid transformation. In the method, we represent the PRE image liver segmentation by a distance transform, $D(\mathbf{x}') : \Omega_M \subset \mathbb{R}^D \rightarrow \mathbb{R}^+$, which equals 0 at the segmentation boundary [113]. On the INTRA image, we have a set of K points, $p_k \in \Omega_F, k = 1, 2, \dots, K$, manually annotated by an operator and these points are driven towards the zero level set of the distance transform $D(\mathbf{x})$. The proposed registration method is mathematically formulated as the following optimization problem:

$$\hat{\boldsymbol{\mu}} = \arg \min_{\boldsymbol{\mu}} (C(\boldsymbol{\mu}; F(\mathbf{x}), M(T_{\boldsymbol{\mu}}(\mathbf{x}))) + \frac{\lambda}{K} \sum_{k=1}^K D(T_{\boldsymbol{\mu}}(p_k)))^2, \quad (4.1)$$

where C is a cost function that measures the dissimilarity between the fixed image $F(\mathbf{x})$ and the transformed moving image $M(T_{\boldsymbol{\mu}}(\mathbf{x}))$, and the second term is the proposed point-to-surface penalty term, which is minimal when the transformed points $T_{\boldsymbol{\mu}}(p_k)$ are at the zero-level set of D . The two terms are balanced by a user-defined weighting factor λ . Computation of the derivative of the terms in 4.1 with respect to $\boldsymbol{\mu}$ is required for minimization of 4.1 with gradient-based optimization methods. Therefore, to make the point-to-surface term continuously differentiable, we chose to use the square of the distance transform as a penalty. Compared to a standard automated registration (i.e. 4.1 without the second term), the added computational cost is negligible since the penalty involves only a few annotation points.

4.3 Experiment and results

4.3.1 Dataset and evaluation measures

In experiments, we used CT images acquired during RFA interventions to assess the performance of the method. The images are five pairs of PRE/INTRA images from different patients and were acquired at Erasmus University Medical Center in 2014. All image data was anonymized prior to processing. Image resolutions vary from 0.71 mm x 0.71 mm to 0.84 mm x 0.84 mm (501x492 to 512x512 in-plane resolution), 3-5 mm slice spacing and 1-2 mm slice thickness (16 to 70 slices).

Both in PRE and INTRA images, the liver was segmented manually. The proposed method only uses the liver segmentation of the PRE image. The liver segmentation of the INTRA image was used for evaluation purposes. To perform quantitative evaluation of registration performance, Dice overlap and average surface distance (ASD) of the INTRA image liver segmentations and the transformed PRE image liver segmentations are computed.

4.3.2 Implementation and experimental settings

The method was implemented as a part of the open-source registration toolbox *Elastix* [105, 114]. Registrations are done according to the method described in section 4.2. A multiresolution strategy [105, 115] with 5 resolution levels was used both for rigid and nonrigid registrations. For nonrigid registration, a cubic B-spline transformation is used [101], with control point spacing of 10 x 10 x 10 mm in the final resolution. An adaptive stochastic gradient descent optimization method [116] is used to minimize the objective function 4.1, using 400 iterations in each resolution and 2048 randomly drawn image samples in every iteration for computing the derivative of C . A cubic B-spline interpolator [117] is used for image interpolations. To study the performance of the point-to-surface penalty term in combination with different dissimilarity metrics, both normalized correlation coefficient (NCC) and mutual information (MI) [112] are used as a dissimilarity measure C in equation 4.1. Since the different dissimilarity measures may lead to registration failures in different regions of the images, distinct point sets to be used by the proposed penalty are selected for NCC and MI. Experiments were repeated for a wide range of weighting values λ , to investigate the sensitivity to this user-defined parameter. We evaluated values from $\lambda = 2^{-9}$ to $\lambda = 1$ according to $\lambda = 2^{i-10}$, $i = 1, 2, \dots, 10$.

4.3.3 Results

After the visual performance evaluation of the unconstrained nonrigid registration result in the first stage, $K \approx 15$ points, on average, were manually annotated on each INTRA image. These points were selected more or less uniformly over the 3D liver surface, at locations suffering from inaccurate registration.

In Figure 4.1, example results on one patient are shown. We show the INTRA image with ground truth liver segmentation overlaid (A), the transformed PRE image liver segmentation superimposed on the INTRA image after rigid registration

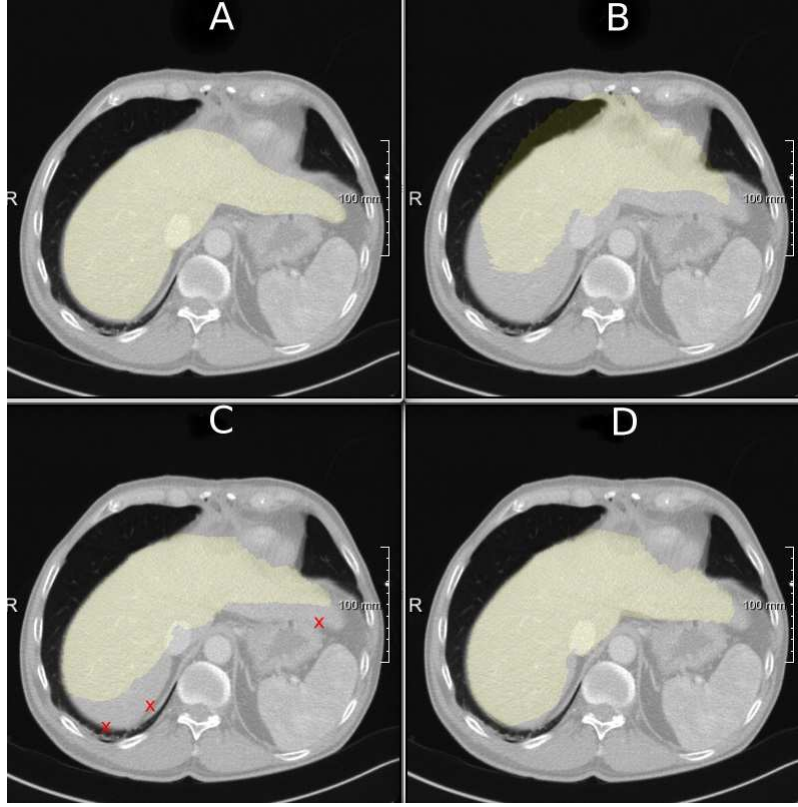


Figure 4.1. Example results for patient 5; INTRA image with ground truth liver segmentation overlaid (A), transformed PRE image liver segmentation superimposed on the INTRA image after rigid registration (B), conventional nonrigid registration (C) and proposed nonrigid registration with point-to-surface constraint and $\lambda=1$ (D). Registrations were done using NCC as a dissimilarity measure in this example.

(B), conventional nonrigid registration (C) and proposed nonrigid registration with point-to-surface constraint and $\lambda = 1$ (D). Registrations were done using NCC as a dissimilarity measure in this example. In the figure, we see that in some regions on (C), the nonrigid registration fails and does not match the entire liver well. These regions are the target for the proposed method. The points highlighted by red crosses were annotated nearby these regions on the liver boundary. Using the proposed method, we expect better registration in these regions, which indeed is observed in panel (D). The images illustrate that the proposed registration method with point-to-surface constraint may improve conventional nonrigid registration. The deformed liver segmentation of the PRE image (D) matches the ground truth liver segmentation of the INTRA image (A) better.

Figures 4.2 and 4.3 show, using NCC and MI respectively, the Dice overlap obtained by rigid registration, conventional nonrigid registration ($\lambda = 0$), and the pro-

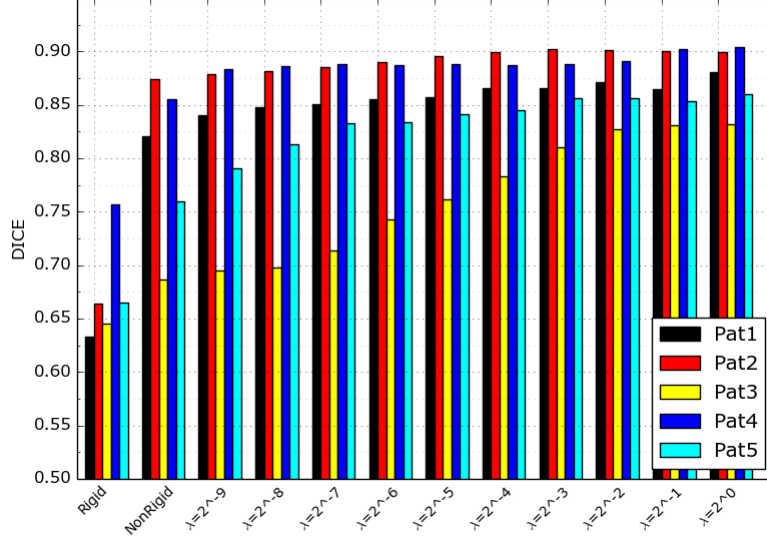


Figure 4.2. Dice overlap values for rigid registration (Rigid), for conventional unconstrained nonrigid registration (NonRigid), and for the proposed algorithm as a function of the weighting parameter λ , using NCC as a dissimilarity measure.

posed method for a range of values for λ . As expected, rigid registration gives the lowest overlap and it is outperformed by the nonrigid registration methods with both dissimilarity metrics. With increasing values of λ , we observe improvement in the performance of the registration. The improvement is somewhat more pronounced when using NCC, because the conventional nonrigid registration results in lower overlap using NCC than using MI. However, for both dissimilarity measures, the overlap gradually improves with increasing λ . From $\lambda = 2^{-2}$ the result seems to stabilize.

In Figures 4.4 and 4.5, the quantitative evaluation results are shown in terms of ASD (millimeter scale). An accurate registration requires that the surface distance of the liver segmentations is small. From the figures, we see that the proposed method outperforms the rigid and conventional nonrigid registration. The method causes the surfaces to be close to each other, generates better alignment of the liver after registration, and thus lower ASD.

4.4 Discussion and conclusion

In this study, we propose a semi-automated nonrigid registration algorithm for robust alignment of pre- and intra-operative CT images of the liver, for use during image-guided interventions. The algorithm tries to match user-selected points on the fixed (INTRA) image liver surface to the surface of the liver on the moving (PRE) image. In this manner, better liver alignment in a registration can be obtained. The method may thus enable the use of pre-operative CT during CT-guided interventions, even in case of large deformations of the liver in between the diagnostic image and

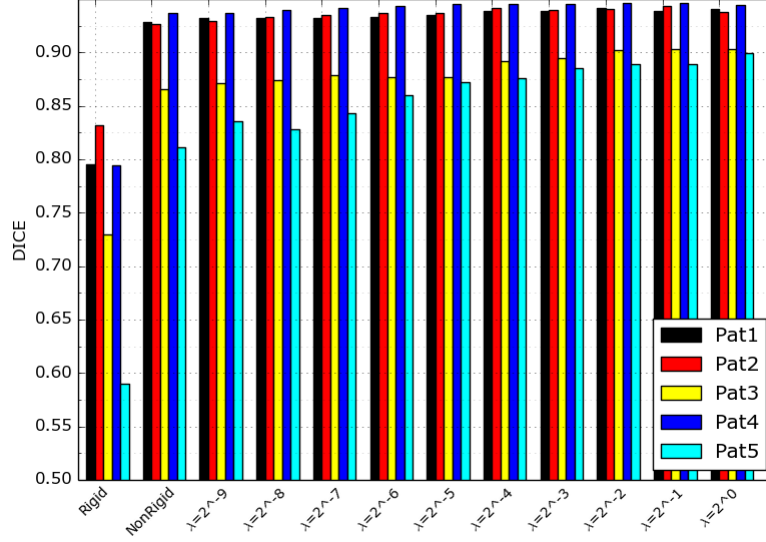


Figure 4.3. Dice overlap values for rigid registration (Rigid), for conventional unconstrained nonrigid registration (NonRigid), and for the proposed algorithm as a function of the weighting parameter λ , using MI as a dissimilarity measure.

the interventional images. Registration experiments on five clinical datasets demonstrate that the method outperforms conventional unconstrained nonrigid registration. The results gradually improve with increasing values of the weighting parameter λ , and stabilize when $\lambda \geq 2^{-2}$. The method requires minimal user interaction during an intervention, since only a few points on the liver surface need to be annotated manually.

In the experiments, we considered Dice overlap and average surface distance between liver segmentations as evaluation measures. However, these measures are mostly reflecting the registration accuracy near the surface of the liver, and may not be entirely representative for registration accuracy within the liver. Further, the influence of the number of annotation points on the results has not been examined. Future work will address these points, by considering the distance between manually annotated corresponding points within the liver and by evaluating the effect of the number of points on the registration accuracy. Moreover, we will extend our experiments to include more datasets. As a conclusion, we developed a semi-automatic registration approach that permits users to improve registration by annotating a few points on the liver border. The method was evaluated on 5 datasets, and demonstrated to improve registration accuracy.

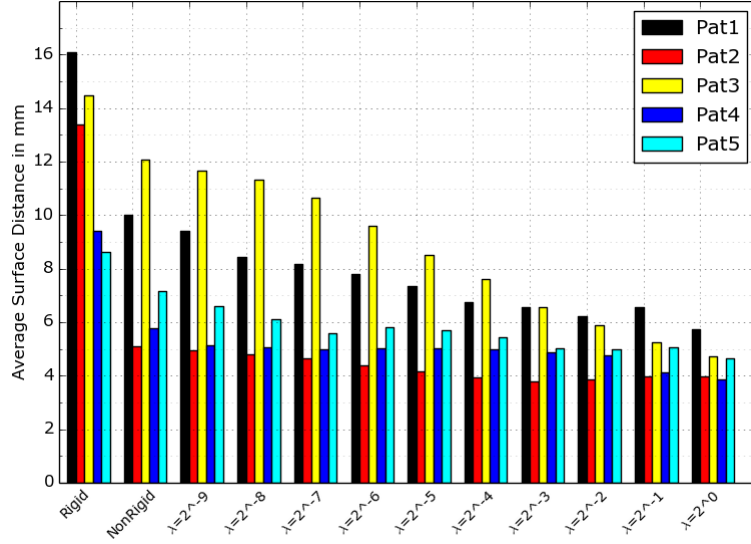


Figure 4.4. Average surface distances for rigid registration (Rigid), for conventional unconstrained nonrigid registration (NonRigid), and for the proposed algorithm as a function of the weighting parameter λ , using NCC as dissimilarity measure.

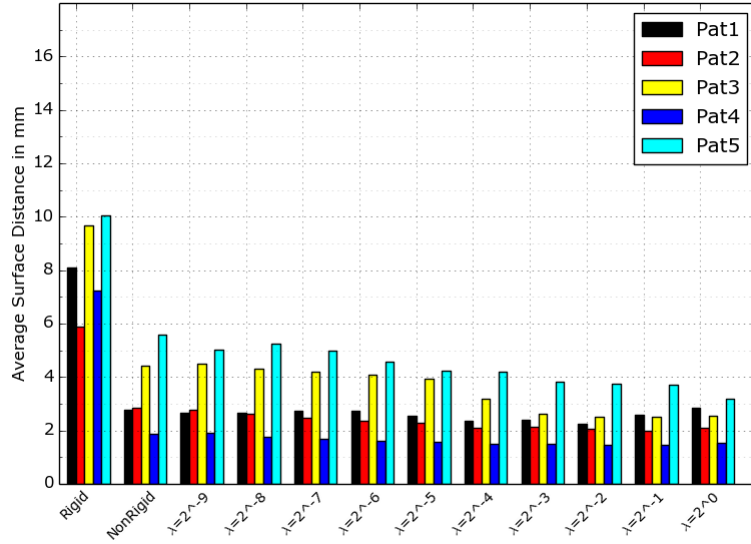


Figure 4.5. Average surface distances for rigid registration (Rigid), for conventional unconstrained nonrigid registration (NonRigid), and for the proposed algorithm as a function of the weighting parameter λ , using MI as a dissimilarity measure.

Quantification of non-rigid liver deformation in radiofrequency ablation interventions using image registration

Abstract — Multi-modal image fusion for image guidance in minimally invasive interventions generally requires a registration of pre-operatively acquired images to interventional images of the patient. Whereas rigid registration approaches are fast, and can be used in an interventional setting, the actual liver deformation may be non-rigid. The purpose of this chapter is to assess the magnitude of non-rigid deformation of the liver between pre-operative and interventional CT images in case of tumor ablations, over the full liver and over parts of the liver that match a 3D ultrasound transducer volumes. We acquired 3D abdominal CT scans of 39 patients that underwent radiofrequency ablation of liver tumors, pre-operative CT images as well as intra-operative CT images. To determine the magnitude of liver deformation due to pose changes and respiration, we non-rigidly registered the pre-operative CT scan to the intra-operative CT scan. By fitting this deformation to a rigid transformation in a region of interest and computing the residual displacements, the non-rigid deformation part can be quantified. We performed quantifications over the complete liver, as well as for two representative 3D ultrasound volumes, where the US acquisition was simulated to be sub-xiphoidal or inter-costal. The results showed that a substantial amount of non-rigid deformation was found, and rotation of patient's pose and deep inhalation caused significant liver deformation. Hence we concluded that non-rigid motion correction in the intervention should be taken into account.

5.1 Introduction

Liver cancer is the second leading cause of cancer death in the world [118, 119]. Whereas surgery is generally considered the preferred treatment option, it is not always feasible to operate the patient, either because of the spread of the disease, or because of the patient's health state. In cases where surgery is not feasible, typical alternative treatments for patients with one or multiple small tumors are minimally invasive interventions such as radiofrequency ablation (RFA), microwave ablation, radiotherapy, chemoembolization, and high-intensity focused ultrasound [25, 27].

Minimally invasive percutaneous ablation treatments are performed under image-guidance using ultrasound or CT. Ultrasound is relatively cheap, does not use ionizing radiation and provides real-time soft tissue imaging, and thus is the ideal candidate for image guidance in minimally invasive ablative liver tumor therapies. However, ultrasound images do not always provide adequate tumor contrast, whereas the pre-interventional image, generally multiphase CT, contains information on the tumor and vessels of the liver [120]. Therefore, approaches using multi-modal image fusion have been proposed and implemented to improve guidance in such procedures. Whereas initial systems have used external trackers to enable the fusion [121, 122], modern transducers and image-based tracking approaches permit tracker-less systems [36, 47, 123–125]. Most of these approaches use rigid/affine transformations to model the relation between the pre-operative image and the patient, because of their easy integration in a real-time guidance system. However, it is well known that the liver is a deformable organ, and shape of the liver may change as a function of the patients pose, internal organ filling and respiration. Purpose of this study is to investigate the magnitude of non-rigid liver deformation when aligning a pre-operative liver to the liver of the same patient during the intervention.

In the literature, several related studies which either register pre-operative images to the intra-operative images or intra-operative images to intra-operative images have been reported. These methods are either feature-based registration method or intensity based registration method. Osorio *et. al* [126] developed a non-rigid registration method to align breath-hold MR images in diagnostic phase with abdominal-compressed CT images which focused on the liver. The registration method used liver vessels from 3 patients for registration. By comparing manual landmarks at vessel bifurcations after rigid registration and non-rigid registration, the extent of liver deformation was estimated. The landmark-based evaluation showed a registration accuracy of 2 mm and the liver deformation ranged from 3 mm to 10 mm. Vijayan *et. al* [127] presented a study on quantifying the shift and deformation of pig livers caused by respiration and pneumoperitoneum in vivo. The study was carried out on one liver using 3D cone beam CT images. Centerlines of the vessels were extracted semi-automatically and were used as features to register between two different images. The result showed that the accuracy of the registration, based on landmark evaluation, was 3 mm. The non-rigid component caused by respiration and pneumoperitoneum could be indicated by comparing the mean distance landmarks after rigid registration and non-rigid registration; however no quantitative result of these was reported. Siebenthal *et. al* [128] studied the respiratory motion and deformation

of the liver. Several free breathing MRI scans of the liver of 12 volunteers were acquired during an hour and registered with the image at the first time point using an intensity-based non-rigid registration method. An average liver deformation of 5 mm was reported, and the registration accuracy of their registration method was 2 mm. Rohlfing *et. al* [129] described a study on quantification of liver deformation caused by respiratory motion. An intensity-based registration method was applied to register several intra-operative images, from the first time point image to each incoming image. The distance between the liver surfaces after rigid registration and non-rigid registration were compared, a mean surface distance of 10 mm was evaluated. Heizmann *et. al* [130] introduced a tool to register a pre-operative image to an intra-operative image in liver surgery. The results showed that at the local segments of the liver, the non-rigid deformation did not exceed 5 mm. However, the details of the method were not mentioned. To the best of our knowledge, there has been no study investigating non-rigid liver deformation occurring when registering pre-operative to intra-operative images, where patient's pose may differ and breathing can not be controlled.

Our contribution is to quantify the magnitude of the non-rigid deformation that needs to be accounted for when aligning intra-patient pre-operative liver images to intra-operative images. This not only encompasses respiratory induced liver deformation, but also liver deformation caused by the time in between the scans and by different patient's poses (patients are sometimes positioned on their side during treatment, to get better access to the lesion). Using the pre-operative and the intra-operative imaging data, we accurately align these non-rigidly, and quantify the non-rigid components in these deformations, for the whole liver as well as for virtual 3D ultrasound volumes (sub-xiphoidal as well as inter-costal), to assess the impact on e.g. 3D ultrasound-guided image-fusion systems. In addition, the accuracy of registration method is also verified in this study.

Organization of this chapter is as follows: in the next section, we introduce our method. Section 5.3 presents our experimental setup, as well as the results of our experiments. In section 5.4, these results are discussed, and conclusions are drawn in section 5.5.

5.2 Method

In this section, we present the method that we used in the study. First, an intensity-based non-rigid registration is applied to align the pre-operative liver image onto the intra-operative image. Because the intra-operative images are often not contrast enhanced, feature or landmark extraction (such as vessels, tumors etc.) is infeasible; therefore, an intensity-based registration method is chosen for this purpose. The registration method is based on a previous study [131]. A quantitative landmark-based evaluation of the registration method was reported for contrast enhanced CT images with an average accuracy of 4.6 mm (including annotation error). The registration method was also evaluated using the Dice overlap metric between a manual segmentation of the liver in the intra-operative image and a transformed manual segmentation of the liver in the pre-operative image (see section 5.2.2). Our previous study showed that 18 out of 24 datasets have a Dice larger than 90% after registration using the

method. In this work, we use an additional 15 datasets and further investigate cases where the Dice is below 90%. For those cases, an additional refined registration step is applied to improve the registration accuracy. In this step, the *kappa* metric [132], which enhances the fit between manual liver segmentations of the two images, is added to the energy function that is minimized during registration. To quantify the non-rigid liver deformation components we compute the rigid transformation that best fits the non-rigid deformation, using a point-based rigid registration approach. Subsequently, we compute the average residual displacement, i.e., the average difference between non-rigid and rigid transformation. This is done for the full liver as well as for sub-volumes representing 3D ultrasound field of views. Each of the steps is discussed in more detail below.

5.2.1 Intensity-based non-rigid registration

In general, image registration spatially aligns images from different modalities or different time points by optimizing a cost function that reflects how well the two images match. Typically, the cost function contains a dissimilarity metric, which is generally based on the image intensities, and additional terms, e.g. containing constraints on the deformation. In this work we use mutual information [112, 133, 134] as similarity metric because the pre-operative images are always contrast (iodine contrast agent) enhanced while intra-operative images are either contrast enhanced or non-contrast enhanced. The transformation is modelled with B-splines [101], and the registration is performed in a multi-resolution scheme [115]. The final transformation is given as a combination of the transformations at each resolution.

In the registration process, we use the (D -dimensional) intra-operative image as the fixed image $F(\mathbf{x}) : \Omega_F \subset \mathbb{R}^D \rightarrow \mathbb{R}$, and the pre-operative image as the moving image $M(\mathbf{x}) : \Omega_M \subset \mathbb{R}^D \rightarrow \mathbb{R}$. The transformation which maps points from the fixed to the moving image domain is defined as $T_\mu(\mathbf{x}) : \Omega_F \rightarrow \Omega_M$, where $\mu \in \mathbb{R}^Q$ is the parameter which represents the Q -dimensional vector of transformation parameters of the B-spline deformation model. The registration now is then modeled by the following optimization problem:

$$\hat{\mu} = \arg \min_{\mu} (-S(\mu; F(\mathbf{x}), M(T_\mu(\mathbf{x}))) + \lambda R(T_\mu(\mathbf{x}))) \quad , \quad (5.1)$$

where $R(T_\mu)$ is a regularization term which constrains non-rigid deformation and λ is a weight which balances the similarity metric $S(\mu; F, M)$ and the regularization term [107, 135, 136]. In our study, because the pre-operative images are contrast enhanced CT while the intra-operative images contain non-contrast enhanced CT images, we chose mutual information $MI(\mu; F, M)$ as the similarity metric:

$$\begin{aligned} S(\mu; F, M) &= MI(\mu; F, M) \\ &= \sum_m \sum_f p(\mu; f, m) \frac{p(\mu; f, m)}{p_F(f)p_M(\mu; m)} \quad , \end{aligned} \quad (5.2)$$

where p is the discrete joint probability of the image intensities of the two images; p_M and p_F denote the discrete marginal intensities probabilities of the moving image

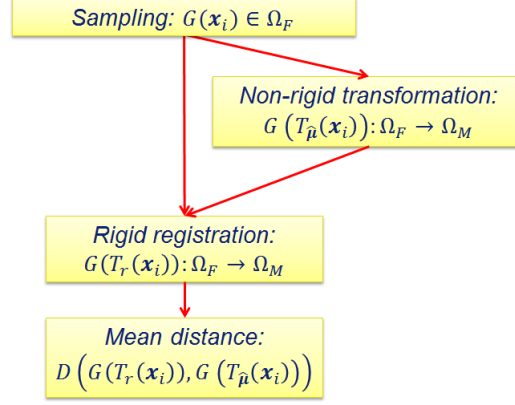


Figure 5.1. Flowing chart of the method to quantify the non-rigid component of the liver deformation.

$M(T_{\mu}(\mathbf{x}))$ and the fix image $F(\mathbf{x})$.

In the first step, we use a conventional registration with only a bending energy regularization term to constrain the deformation inside the liver. Liver masks are created for both the pre-operative image and intra-operative image by interpolating ten manually drawing contours around the livers at every 3-4 slices. The liver masks act as region of interest for the cost function computation, thus they are not necessary to be accurate liver segmentations. Because of large differences in patient's pose (orientation) and breathing state, some cases may have poor registration accuracy. Therefore, we quantitatively check all the registration using DICE metric described in section 5.3.3. In case that the registration quality is not sufficient (i.e. DICE smaller than 90%), we use the manual liver segmentation as an additional information for the second registration. In this manner, an additional term, *kappa* metric $K(\mu; F, M)$ is used to maximize the match between the two livers based on the liver segmentation [105, 132]. In this stage, the cost function in equation 5.1 can be rewritten as:

$$S(\mu; F, M) = \frac{1}{1 + \omega} (\text{MI}(\mu; F, M) + \omega K(\mu; F, M)) \quad , \quad (5.3)$$

$$K(\mu; F, M) = \frac{2 \sum_{\mathbf{x} \in \Omega_F} I_{F(\mathbf{x})=f, M(T_{\mu}(\mathbf{x}))=f}}{\sum_{\mathbf{x} \in \Omega_F} I_{F(\mathbf{x})=f} + \sum_{\mathbf{x} \in \Omega_F} I_{M(T_{\mu}(\mathbf{x}))=f}} \quad , \quad (5.4)$$

where I is the indicator function and f is the value of the segmentation (default to 1).

After this second registration, the result is checked again using metric described in section 5.3.3. Cases with Dice less than 90% are not included in the quantification section 5.2.2.

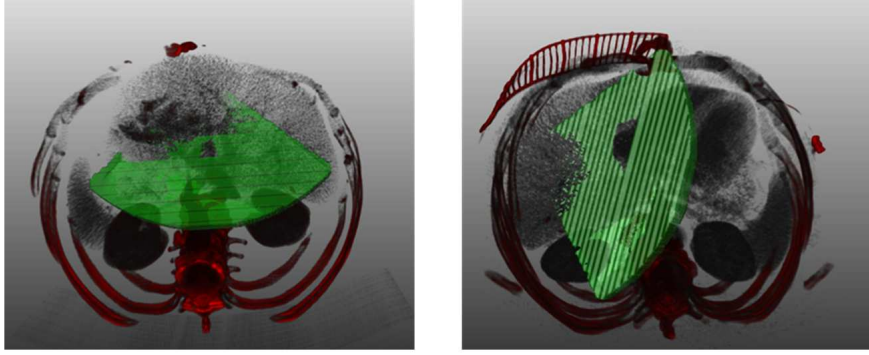


Figure 5.2. Simulation of visual ultrasound volumes in CT images: the left is 3D ultrasound volume at sub-xiphoidal position; the right is 3D ultrasound volume at inter-costal position.

5.2.2 Liver deformation quantification

In this section, we propose a method to quantify liver deformation by using the non-rigid transformation result of the optimal non-rigid registration in section 5.2.1 combined with a point-based rigid registration method. First, a grid (equidistantly sampled with spacing of $d = 1$ cm) $G(\mathbf{x}_i)$ is created within the liver segmentation L^{SF} in the intervention image space Ω_F . Next, grid $G(\mathbf{x}_i)$ is transformed to the pre-operative image space Ω_M by using the non-rigid transformation $\mathbf{T}_{\hat{\mu}}(\mathbf{x})$. By rigidly registering the original points $G(\mathbf{x}_i)$ in the intra-operative image space Ω_F to the points in the pre-operative space Ω_M using a point-based registration [137], the rigid component of the liver deformation can be estimated. Subsequently, the non-rigid component of the whole liver deformation can be quantified by measuring the mean distances between the two set of points (see Figure 5.1). Mathematically, the mean magnitude of the non-rigid liver deformation is estimated as:

$$D(G(\mathbf{T}_{\hat{\mu}}(\mathbf{x}_i)), G(\mathbf{T}_r(\mathbf{x}_i))) = \frac{1}{n} \left(\sum_{i=1}^n |\mathbf{T}_{\hat{\mu}}(\mathbf{x}_i) - \mathbf{T}_r(\mathbf{x}_i)| \right) \quad , \quad (5.5)$$

where $\mathbf{T}_r(\mathbf{x}_i)$ is the rigid transformation results from the point-based registration and n is number of points in the set $G(\mathbf{x}_i)$.

We also quantify the non-rigid component of a part of the liver by simulating 3D ultrasound volumes at two typical positions for liver ultrasound imaging in the intervention, i.e. sub-xiphoidal and inter-costal (see Figure 5.2). For each volume, we extract a similar grid of points inside the simulated ultrasound volume (see Figure 5.3). The non-rigid component of each partial liver deformation is quantified using the same technique mentioned above.

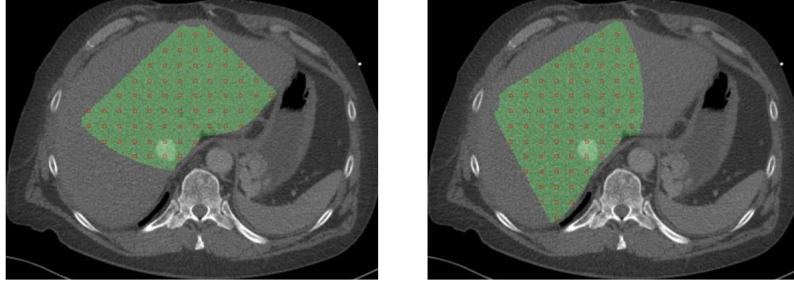


Figure 5.3. 2D viewers of grids of points at sub-xiphoidal region (left) and inter-costal region (right).

5.3 Experiments and results

5.3.1 Image data

Abdominal diagnostic and intra-operative anonymized CT scans of 39 patients were randomly selected from patients that underwent abdominal CT scanning and CT-guided RF ablation in the Erasmus MC between 2010 and 2015. Of those, 24 cases were involved in our previous study [131]. From the diagnostic images, the contrast enhanced images were selected for the study. All images have an in-plane pixel size of 0.56 mm x 0.56 mm to 0.92 mm x 0.92 mm, 3-5 mm slice spacing, 1-2 mm slice thickness, 512x512 pixels per slice, and 36-71 slices. Image acquisition was performed according to the standard clinical protocol: 60 seconds after the injection of 120 cc intravenous contrast agent. Both the intra-operative images and diagnostic images were acquired with a tube voltage of 80-100 KV and a tube current of 172 - 288 mAs. Of the intra-operative images, 18 are non-contrast enhanced images and 21 are contrast enhanced with 80-120 cc intravenously administered contrast agent. The main reason for using the contrast enhanced images was to obtain accurate information on the tumor location. Furthermore, in 14 out of the 39 cases, the patient was rotated (30-100 degrees) w.r.t. a supine position on the CT table, to provide access to the needle introduction site. For those cases, the images were manually rotated along the z-axis prior to registration such that the spines on both images have approximately the same orientation. All of the 39 pre-operative images are in exhale state and with breath-hold. The intra-operative images are in free breathing state (as patients are sedated), and six cases are in deep inhale state. In general, the field of view of the 3D abdominal images is larger than the region of interest i.e. the liver.

A 3D ultrasound volume was acquired with a Philips iU22 xMATRIX US system using X6-1 PureWave xMATRIX transducer. The 3D ultrasound volumes resolution was set to values typically used during interventions, yielding images containing 192x246x117 voxels with voxel size of 1.144x0.594x1.193 mm.

5.3.2 Registration software and parameter settings

We used *Elastix*, an open source registration software package developed by Klein and Staring, which is available at elastix.isi.uu.nl. The initial alignment (translation) of registration is based on the center of mass of the liver mask. The five resolutions of the B-spline grid are set to [160 80 40 20 10] mm. An adaptive stochastic gradient descent optimizer [116] is used to solve the minimization problem in 5.1, in which 2000 samples are randomly selected to compute the derivative of the cost function. The number of iterations for each resolution is set to 500 to ensure sufficient number of iterations for convergence. The weight factor for bending energy λ is set at 200 (similar to our previous study). After some pilot experiments with the four cases in the second step (see Section 5.2.1), *kappa* metric weight w is chosen as 50. The registration is performed on an AMD Opteron 2378-core, 2.8GHz, 64 GB RAM on a Linux cluster.

5.3.3 Registration verification

As mentioned in section 5.3.1, 18 out of 39 cases are non-contrast enhanced CT, hence landmark based evaluation is not feasible for those scans. In this study, we used Dice metric to verify the accuracy of the registration algorithm for all the cases. The Dice metric is an overlap measure between the transformed liver segmentation L^{SM} of the pre-operative image and the liver segmentation L^{SF} of the intra-operative image. For this purpose, manual segmentations of the liver were made by experts. Mathematically, Dice similarity coefficient (DSC) is formulated as:

$$\text{DSC}(L^{SF}, L^{SM}) = 2 \frac{|L^{SF} \cap L^{SM}|}{|L^{SF}| + |L^{SM}|}, \quad (5.6)$$

where $|\cdot|$ denotes the number of voxels inside the segmentation.

In total, 31 out of 39 cases were successfully registered in the first step, with a Dice larger than 90%, and with visually no large errors observable. Four cases were correctly registered after the second step, i.e. the registration using the *kappa* term with the liver segmentations, with Dice also larger than 90%. We were unable to successfully register four cases because of the large rotation angle of intervention image combined with deep inhalation, leading to very large deformations of the liver which could not be compensated by the registration method. In the end, 35 out of the 39 cases were successfully registered with Dice of $92.7 \pm 1.8\%$ on average. In addition, the average Dice overlap value of the 35 cases using rigid registration method is $84.5 \pm 6.9\%$, which is statistically significantly smaller than the result of non-rigid registration method.

5.3.4 Quantification results

Using the method described in section 5.2.2 we computed the non-rigid components of the liver deformation. For further analysis, we divided the dataset into two groups: one group contains all cases which do not have either rotation or deep inhalation (normal cases), and the other contains those having rotation and/or deep inhalation.

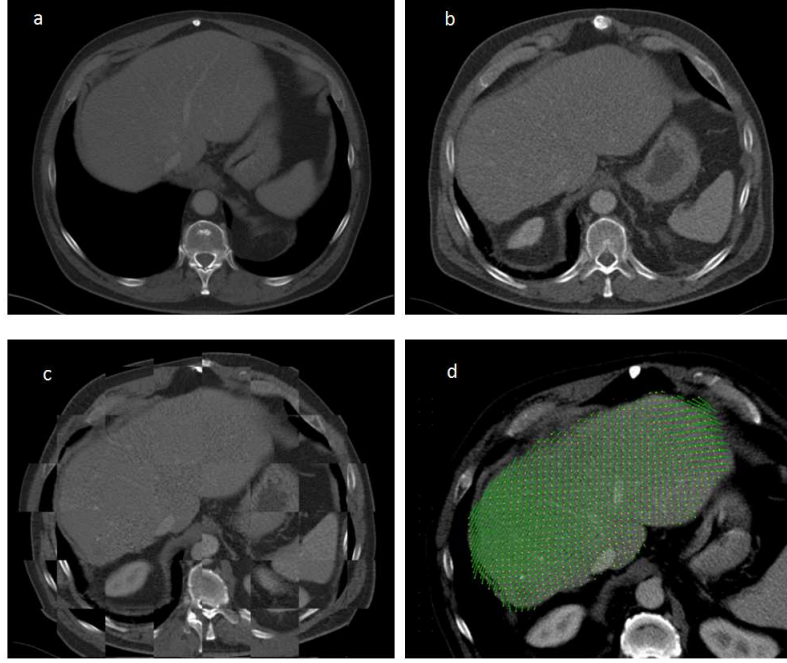


Figure 5.4. Fig.4: An example of successfully registered case: a) pre-operative image; b) intra-operative image; c) checker board view of the registered image; d) the deformation field shows the direction of liver transformation from pre-operative image to the intra-operative image.

We, hence, quantified the non-rigid components of nine groups: complete livers on all the cases (CA), complete livers on the normal cases (CN), complete livers on the cases having rotation and deep inhalation (CRI), the inter-costal regions on all the cases (IA), the inter-costal regions on the normal cases (IN), the inter-costal regions on having rotation and/or deep inhalation (IRI), the sub-xiphoidal regions on all the cases (SA), the sub-xiphoidal regions on normal cases (SN), the sub-xiphoidal regions on having rotation and/or deep inhalation (SRI). On average, the non-rigid deformation components respectively are 5.9 ± 1.6 mm, 5.1 ± 1.1 mm and 7.2 ± 1.4 mm for group CA, group CN and group CRI. For inter-costal regions, average of the non-rigid components of group IA, group IN and group IRI respectively are 4.6 ± 1.2 mm, 4.1 ± 0.9 mm and 5.4 ± 1.2 mm. For sub-xiphoidal regions, on average, group SA, group SN and group SRI contain the non-rigid component of 4.8 ± 1.5 mm, 4.0 ± 0.9 mm and 6.1 ± 1.5 mm correspondingly. All of the non-rigid components are illustrated in Figure 5.7 and Figure 5.8.

Furthermore, we performed T-tests for the non-rigid deformation quantification between the non-rotation group and the rotation/inhale group. The p -values for respectively the full liver, inter-costal and sub-xiphoidal non-rigid components are 0.005, 0.022 and 0.004, showing that rotation and inhaled breathing statistically significantly

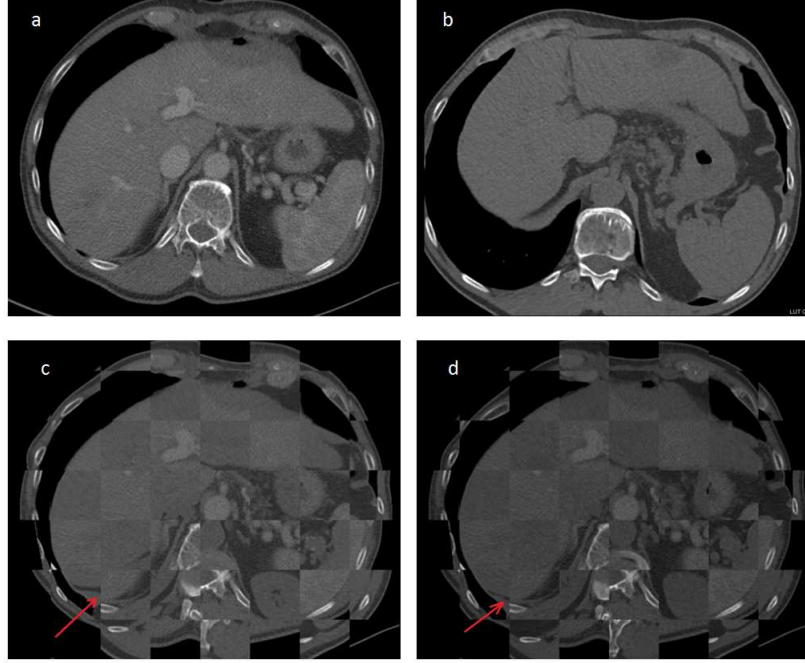


Figure 5.5. An example of case with deep inspiration and non-contrast enhancement involves in the refined registration step: a) pre-operative image; b) intra-operative image; c) fused image without *kappa* term (DICE of 88%); d) fused image with *kappa* term (DICE of 93%). The arrows point to the position where the registration is improved.

increase liver deformation.

5.4 Discussion

This study quantifies the non-rigid component of the deformation between the pre- and intra-operative situation in liver interventions by using image based registration on CT data. Results were obtained for the full liver, and relevant regions of interest in case of ultrasound guided intervention. For the latter, the sub-xiphoidal region and the inter-costal region were extracted by simulating 3D ultrasound volume at the corresponding positions. The non-rigid components of the liver deformation were quantified by comparing corresponding components transformed by the transformation that results from the non-rigid intensity-based registration and by the point-based rigid registration method.

Out of 39 cases included in our study, 31 cases could directly be registered successfully, four cases required an additional optimization term based on a liver segmentation (coined *kappa* metric), and four cases could not be successfully registered. All of the successful cases have a Dice overlap larger than 90%. The non-rigid components

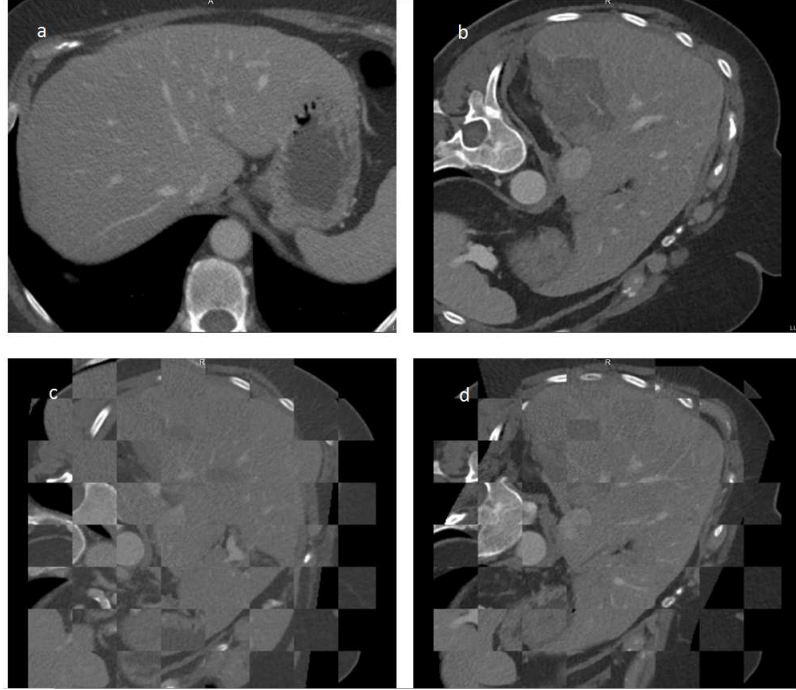


Figure 5.6. A case with large liver deformation caused by rotation (~ 100 degree): a) pre-operative image; b) intra-operative image; c) registration without *kappa* metric (DICE of 83%); d) registration with *kappa* metric term (DICE of 92%).

of completed liver, the sub-xiphoidal region and the inter-costal region respectively are 5.9 ± 1.6 mm, 4.8 ± 1.5 mm and 4.6 ± 1.2 mm on average. These numbers provide an estimation of the remaining error when using rigid registration to align the pre-operative image to the intra-operative images, which is common practice in many current guidance systems. These errors should either be taken into account, or non-rigid motion compensation methods should be applied.

When inspecting the cause of the deformation component, rotation of the patient between imaging sessions and differences in breathing states significantly increase the magnitude of liver deformation. With small rotation, the non-rigid components of completed liver, the sub-xiphoidal region and the inter-costal region respectively were 5.1 ± 1.1 mm, 4.1 ± 0.9 mm and 4.0 ± 0.9 mm, whereas the other cases have errors which were 1-2 mm larger (see Figure 5.8); these differences were statistically significant. This implies that efforts to limit differences in patient's pose and breathing state may be relevant for ablation procedures although perhaps not feasible to achieve. These errors also confirm that the range of the safety margin of 1 cm that is generally used in ablation of liver lesions to ensure a successful treatment [118].

Our study obtained comparable results compared to other studies on liver deformation. Osorio *et. al* [126] used a non-rigid registration method to register three cases of pre-operative MRI images and intervention CT images. A range of liver

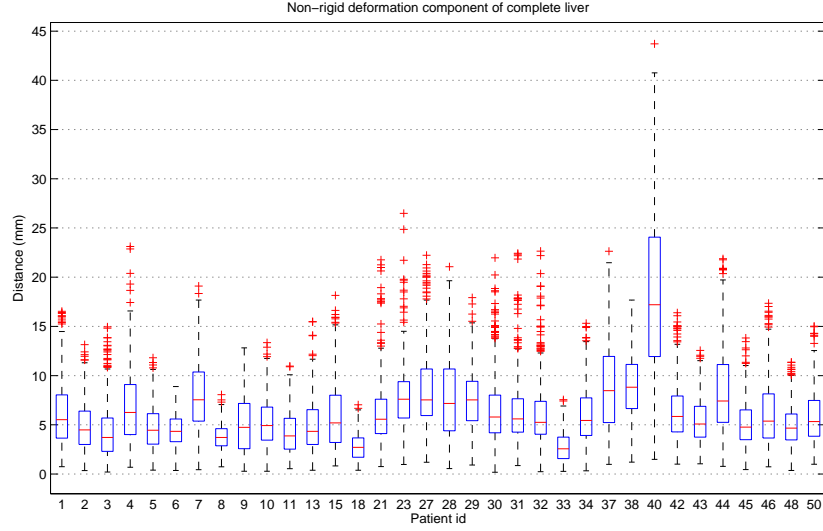


Figure 5.7. Boxplot of non-rigid component of the complete liver deformation of 35 successful cases.

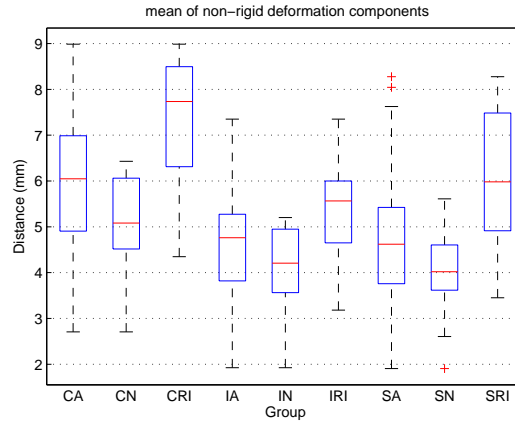


Figure 5.8. Boxplot shows averages of non-rigid components excluding an outlier (patient 40).

deformation between 3 mm to 10 mm for the whole liver was reported while in our study, 95% of liver deformation was from 2.5 mm to 9 mm (see Figure 5.8). In the work of Heizmann *et. al* [130], non-rigid deformation of the liver segments right lobe non rigid component of less than 5 mm was reported. In our study, in cases of no

rotation and deep inspiration, the non-rigid deformation component of the whole liver and sub-xiphoidal region were 5.1 ± 1.1 mm and 4.0 ± 0.9 mm. Note that, in our data, pre-operative images and intra-operative images were acquired in different acquisition sessions and that sub-xiphoidal region contains segments in both the left lobe and the right lobe. Rohlfing *et. al* [129] reported non-rigid liver deformation on the liver surface of 10 mm on average; however their quantification metric is different from our metric, which mainly concerns inside of the liver.

The main limitation of our study is its dependency on an accurate registration. This method was not able to adequately align four cases, which suggests that for difficult cases the non-rigid component may even be larger. By having visual inspection of the registration results by radiologists, as well as by having a second stage registration for less accurate cases, we can confirm that the results are valid. In addition, this is also verified by the comparison to other studies.

5.5 Conclusion

In conclusion, we have developed an approach to determine the non-rigid component in liver deformation between the pre- and intra-operative situation in liver interventions. We computed it for the whole liver, as well as to the inter-costal and the sub-xiphoidal regions-typically images with US during procedures. This study confirms that in the liver region of interest, a substantial part of the deformation is non-rigid, and this should be accounted for when using rigid registration approaches. Patient positioning and breathing control may help in reducing the non-rigid deformation. Also, methods to compensate for non-rigid deformation should be pursued.

An automatic registration method for pre- and post-interventional CT images for assessing treatment success in liver RFA treatment

Abstract — In image-guided radiofrequency ablation for liver cancer treatment, pre- and post-interventional CT images are typically used to verify the treatment success of the therapy. In current clinical practice, the tumor zone in the diagnostic, pre-interventional images are mentally or manually mapped to the ablation zone in the post-interventional images to decide success of the treatment. However, liver deformation and differences in image quality as well as in texture of the ablation zone and the tumor area make the mental or manual registration a challenging task. Purpose of this chapter is to develop an automatic framework to register the pre-interventional image to the post-interventional image.

We propose a registration approach enabling a non-rigid deformation of the tumor to the ablation zone, while keeping locally rigid deformation of the tumor area. The method was evaluated on CT images of 38 patient datasets from Erasmus MC. The evaluation is based on Dice coefficients of the liver segmentation on both the pre-interventional and post-interventional images, and mean distances between the liver segmentations. Additionally, residual distances after registration between corresponding landmarks in the images were computed.

The results show that rigid registration gives a Dice coefficient of 87.9%, a mean distance of the liver surfaces of 5.53 mm, and a landmark error of 5.38 mm, while non-rigid registration with local rigid deformation has a Dice coefficient of 92.2%, a mean distance between the liver segmentation boundaries near the tumor area of 3.83 mm and a landmark error of 2.91 mm, where a part of this error can be attributed to the slice spacing in our CT images.

This method is thus a promising tool to assess the success of RFA liver cancer treatment.

6.1 Introduction

Radiofrequency ablation (RFA) is an image-guided intervention for the treatment of liver cancer which has become popular in recent years [46, 138, 139]. During the intervention, radiofrequency are applied via an ablator to locally heat and destroy the tumor cells. In practice, radiologists typically compare the tumor region from pre-interventional images to the ablation zone in post-interventional CT images to assess treatment success [91, 94, 140]. They mentally compare shape, size, and position of the tumor and the treated zone. For this evaluation, the treatment is considered successful if the tumor is completely enclosed by the ablation zone with a safety margin of 5 mm or larger. This safety margin is narrow to minimize collateral damage to healthy liver tissue. If any residual tumor tissue is detected outside the thermally destroyed region, the treatment is considered unsuccessful [141]. To better assess the relation between the tumor area and the ablated region, an accurate spatial alignment of the pre- and post-interventional images is required. This facilitates a retrospective quantitative study to determine requirements of the ablation zone, to optimize future therapy. It possibly also supports earlier assessment of treatment success. Purpose of our work thus is to develop and evaluate a method for accurately registering pre- and post-operative CT images of the liver.

The challenges in registering the pre and post-interventional CT images are liver deformation due to patient breathing and differences in texture between the tumor area and the ablation zone. To address these challenges, we utilize non-rigid deformations to account for deformations, while considering the transformation to be rigid at the tumor area to prevent incorrect deformation of the tumor area to the ablation zone.

Several groups have previously investigated registration of CT liver images. These studies can be categorized into those using rigid and non-rigid registration. For most of the studies the registration accuracy was determined by measuring the residual registration error in corresponding anatomical landmarks such as vessel bifurcations or locations at the surface of the liver. Heizmann et al. [130] concluded that rigid registration of liver segments of pre- and intra-operative images is feasible with an accuracy of 5 mm. Rieder et al. [102] reported on a rigid registration method using the ROI of the tumor in the pre-interventional CT image and that of ablation zone in post-interventional CT image which achieved mean registration accuracy of 5-6mm. Lange et al. [103] registered pre- and post-operative liver CT images using manually placed corresponding landmarks with an accuracy of 2 mm. To assess the tumor response to RFA treatment on CT images, Niculescu et al. [142] described a non-rigid registration framework based on a finite element method to model the deformation. There was no quantitative evaluation reported in the study. Xie et al. [141] worked on liver registration in CT with a consideration of lung motion. The non-rigid registration contains two steps: first, scale invariant feature transformation was used to extract controls points and subsequently a bi-thin plate spline method was used to compute the deformation. Kim et al. [97] investigated a non-rigid registration method for aligning pre- and post-interventional CT images for RFA treatment. The accuracy of the registration by using corresponding landmark reached accuracy up to 1.3 mm. However, details on the registration method were not reported in the study.

In this chapter, we build on these previous studies, and develop and evaluate an automatic non-rigid registration method for the alignment of pre- and post-interventional liver images. Our contribution is an automatic method, an extensive parameter optimization and an evaluation on a large set of clinical CT images.

This chapter is organized as follows: in the next section, we introduce our method: Section 6.3 presents our experimental setup and the evaluation frame work, as well as the results of our experiments. In Section 6.4, these results are discussed, and conclusions are drawn in Section 6.5.

6.2 Methods

Image registration is a frequently used technique in the field of medical image processing [114, 143]. The image registration task is, given a fixed image $I_F(\mathbf{x})$ and a moving image $I_M(\mathbf{x})$, to find a transformation $T(\mathbf{x}) = \mathbf{x} + u(\mathbf{x})$ that spatially aligns $I_M(T(\mathbf{x}))$ to $I_F(\mathbf{x})$. The deformation field $u(\mathbf{x})$ that represents the transformation after registration is either rigid or non-rigid. In rigid registration, the moving image $I_M(\mathbf{x})$ is translated and/or rotated to best match the fixed image $I_F(\mathbf{x})$. In non-rigid registration, the moving image $I_M(\mathbf{x})$ can deform freely to yield the best match to the fixed image $I_F(\mathbf{x})$. The optimal alignment is generally determined by optimizing a similarity metric $S(T; I_F, I_M)$. Commonly used similarity metrics are the sum of squared differences (SSD), mutual information (MI) and normalized cross correlation (NCC). In this study, we chose NCC because the images are from the same modality (contrast enhanced CT) satisfying the assumption underlying NCC that there is a linear relation between the intensity values of the fixed and moving images. This assumption is not correct at the ablation zone, which is why we utilize a local penalty on the deformation field to prevent large deformations near the tumor. Formally, Normalized Cross Correlation, which measures the similarity of the intensity between the two images based on their intensity variances, is defined as:

$$\text{NCC}(T; I_F, I_M) = \sum_{\mathbf{x}_i \in \Omega_F} \frac{(I_F(\mathbf{x}_i) - \bar{I}_F)(I_M(T(\mathbf{x}_i)) - \bar{I}_M)}{\sigma_F \sigma_M} \quad , \quad (6.1)$$

where Ω_F is the domain of the fixed image $I_F(\mathbf{x})$; \bar{I}_F, \bar{I}_M are the mean intensity of $I_F(\mathbf{x})$ and $I_M(T(\mathbf{x}))$; and σ_F, σ_M are standard deviation of intensity of $I_F(\mathbf{x})$ and $I_M(T(\mathbf{x}))$.

6.2.1 Non-rigid registration algorithm

Targets of our registration task are the liver, the tumor and the ablation zone. Because imaging is done at different time points, and because of differences in breathing state, the liver may have moved and deformed [127, 130], therefore a rigid transformation is often insufficient for an accurate registration. Hence, a non-rigid registration approach to align the pre- and the post-images is taken.

Conventionally, the registration problem is formulated as an optimization problem which minimizes a cost function $\mathcal{C}(T; I_F, I_M)$ with respect to the transform T :

$$\hat{T} = \arg \min_T \mathcal{C}(T; I_F, I_M) \quad , \quad (6.2)$$

with

$$\mathcal{C}(T; I_F, I_M) = -\mathcal{S}(T; I_F, I_M) + \alpha \mathcal{P}(T) \quad , \quad (6.3)$$

where $\mathcal{P}(T)$ is a regularization term which constrains non-rigid deformation and α is a weighting factor which balances the similarity metric $\mathcal{S}(T; I_F, I_M)$ and the regularization term $\mathcal{P}(T)$ [103].

We model the non-rigid transform T with a B-Spline deformation field, where parameter μ models the transformation T . Finding the optimal transformation \hat{T} in our case therefore is an optimization problem, determining the parameter μ that minimizes the cost function $\mathcal{C}(\mu; I_F, I_M)$:

$$\hat{T}_\mu = \arg \min_T \mathcal{C}(T_\mu; I_F, I_M) \quad , \quad (6.4)$$

or

$$\hat{\mu} = \arg \min_T \mathcal{C}(\mu; I_F, I_M) \quad , \quad (6.5)$$

We employ an iterative stochastic gradient descent optimizer for equation (6.5). In every iteration k , the current parameter μ_k is updated by adding a small step in direction of the derivative of the cost function $\partial \mathcal{C} / \partial \mu$:

$$\mu_{k+1} = \mu_k - a_k \frac{\partial \mathcal{C}}{\partial \mu} \quad , \quad (6.6)$$

where $a_k > 0$ is the size of the step which changes in every iteration. Klein et al. [116] proved that using a decay of a_k according to $a_k = a / (k + A)^\gamma$, where $a > 0, A \geq 1$, and $0 \leq \gamma \leq 1$ are user-predefined constants, the convergence rate significantly reduces computation time without affecting final result. Based on this result, we used the stochastic gradient descent in our study.

Finally, as we are interested in registering the liver only, the similarity metric is only evaluated over liver area defined by liver mask (see Section 6.3.2).

6.2.2 Local rigid registration

The standard non-rigid registration not only deforms to align global structures in the images but also locally minimizes the differences, e.g. at the tumor area and ablation zone. This may cause an incorrect registration because the texture and the intensity of the tumor area and the ablation zone are different (see Fig. 6.1). A global regularization term $\mathcal{P}(T)$ in equation (6.3) can limit the transformation freedom in this area, but it may also affect the transformation of others structures and thus lead to globally incorrect registration. Therefore we propose a registration method which deforms the tumor rigidly while allowing the other structures to deform more freely.

The idea of using local rigid registration was first introduced by Staring (2007) [107] in lung tumor follow-up diagnosis. The fixed regularization term $\mathcal{P}(T)$ was replaced by a rigidity penalty term $\mathcal{P}^{rigid}(T; I_M)$ which is defined as follow:

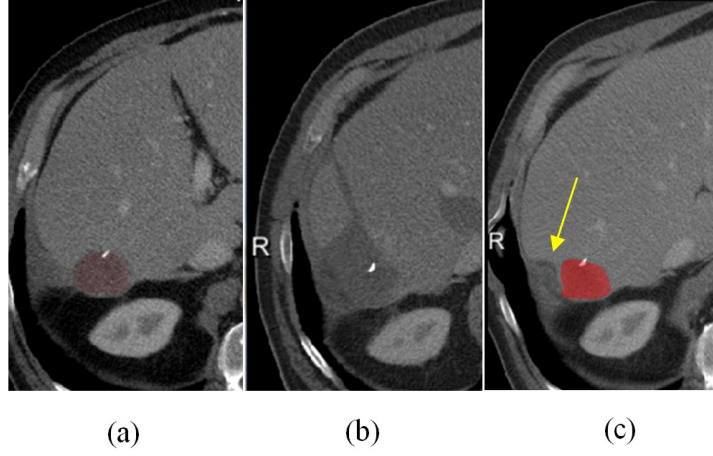


Figure 6.1. Example of incorrect deformation around tumor area: a) a pre-interventional RFA image with a tumor area; b) a post-interventional RFA image with ablation zone; c) the registered the pre-image with an arrow to indicate the incorrect transformation in the corresponding ablation zone.

$$\mathcal{P}^{rigid}(T; I_M) = \frac{1}{\sum_{\mathbf{x}} c(T(\mathbf{x}))} \times \sum_{\mathbf{x}} c(T(\mathbf{x})) \times \left\{ c_{AC} \sum_{k,i,j} AC_{kij}(\mathbf{x})^2 + c_{OC} \sum_{i,j} OC_{kij}(\mathbf{x})^2 + c_{PC} PC(\mathbf{x})^2 \right\}, \quad (6.7)$$

where the weights c_{AC}, c_{OC} and c_{PC} balance the three terms: affine term $AC_{kij}(\mathbf{x})$, orthonormality term $OC_{kij}(\mathbf{x})$ and properness term $PC(\mathbf{x})$; and $c(\mathbf{x}) \in [0, 1]$ is a user-predefined coefficient (mask), so that the part inside the mask is restricted to rigid movement while the other parts may deform less strictly. The value of $c(\mathbf{x})$ is defined as:

$$c(\mathbf{x}) = \begin{cases} 1 & \text{if } \mathbf{x} \in \Omega_R \\ 1 - \frac{1}{1 + e^{\frac{D(\mathbf{x}) - \beta}{\alpha}}} & \text{else} \end{cases}, \quad (6.8)$$

where α and β are pre-defined parameters; $D(\mathbf{x})$ is the Euclidean distance transform of the mask image with zero distance at the tumor boundary, and Ω_R is the liver tumor area. Parameter α regulates the slope of the threshold and β acts as an offset of the distance transform function $D(\mathbf{x})$. This ensures that the transformation $T(\mathbf{x})$ is rigid inside, almost rigid around and non-rigid outside the tumor area.

From the simulation of coefficient image $c(\mathbf{x})$ w.r.t α and β in Fig. 6.2 we can see that the curves with $\alpha = 2$ and $\beta \geq 5$ mm have smooth transition bands between the constrained area and the unconstrained area. We therefore chose these values of α and β as the parameters to create the image $c(\mathbf{x})$.

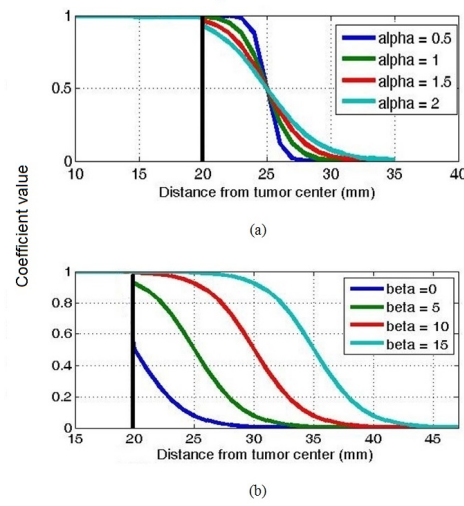


Figure 6.2. Simulation of profile of the coefficient image $c(\mathbf{x})$ with tumor radius of 20 mm and several values of α and β . The top figure is a plot of $c(\mathbf{x})$ when $\beta=5$ mm. The bottom figure is a plot of $c(\mathbf{x})$ when $\alpha = 2$.

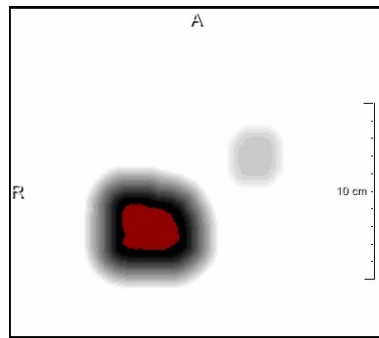


Figure 6.3. The coefficient image $c(\mathbf{x})$: the dark areas present a high constraint of rigid deformation. The coefficient image containing two tumors has two dark areas.

6.3 Experiments and results

6.3.1 Image data

We retrospectively obtained 38 anonymized abdominal multiphase Contrast Enhanced CT datasets that were acquired on a Siemens CT Scanner in the Erasmus MC, University Medical Center Rotterdam from 2010 to 2013. The post-CT is a follow-up scan, 4-6 weeks after the intervention. This ensures minimal ablation zone shrinkage and minimal liver growth. The portal-venous phase images from the multiphase abdominal CT-scans were selected for the study, and none of the CT datasets obtained was excluded from this study. 32 % of the patients have lesion with diameters up to 3 cm. The images have resolution of 0.74 mm x 0.74 mm to 0.84 mm x 0.84 mm, 2-5 mm slice spacing (1 dataset has a slice spacing of 2 mm; 8 datasets of 3 mm; 29 datasets of 5 mm), 1-2 mm slice thickness, 72-180 axial slices and 512 x 512 pixels per slice. Image acquisitions were performed according to the standard clinical protocol: 60 seconds after the injection of 100 cc intravenous contrast agent. In general, the field of view of the 3D abdominal images is larger than the region of interest i.e. the liver. Hence, to reduce processing time for image registration, we manually cropped the images to fit the liver.

6.3.2 Manual segmentation for registration

A clinician manually outlined the tumor in the pre-interventional image. The coefficient image, then, was created based on the tumor segmentation image using equation (6.8). The registration requires a liver mask to determine a region of interest. The liver mask does not need to be an accurate liver segmentation. It was created by interpolating 10 manually annotated contours around the liver, such that all the contours encompass the liver. An existing liver segmentation approach [83] would probably do as well.

6.3.3 Registration software and parameters

For the registration, we use Elastix registration software developed by Klein and Staring [105], which can be downloaded from Elastix website. Initialization of the registration is based on alignment of center of mass of the liver mask. A multi-resolution B-spline-based registration is achieved with Elastix. In this multi-resolution registration approach, smoothed versions of the image at different scales are determined by convolution with a Gaussian kernel. One of the most important parameters in Elastix is the grid size of the control points of the B-spline model. In this study, we used 4 resolutions as suggested in Staring [107]. The grid space of the B-spline is set to [8 4 2 1] times a physical unit (in mm) which is tuned in a training stage. In the course level of multi-resolution registration, we set the grid size high to allow the registration match large structures and skip small structures. The final resolution uses a small grid size to ensure that the detailed structures in the livers can be matched. The weight parameters for rigidity are set as (RigidityPenaltyWeight 0.1 0.1 0.1 4.0), (LinearityConditionWeight 100.0), (OrthonormalityConditionWeight

1.0), (PropernessConditionWeight 2.0). The complete parameters setting file can be found in the elastix database of parameter setting files.

6.3.4 Evaluation metrics

In this study, we used four metrics to evaluate the registration algorithm. The first metric is an overlap measure between the transformed liver segmentation of the pre-image and the liver segmentation of the post-image. To this end, a manual segmentation of the liver was made by an expert. Note that this segmentation was for the evaluation purposes only, and was not used during the registration procedure. For the overlap we used the Dice similarity coefficient (DSC), which is given by:

$$\text{DSC}(X, Y) = 2 \frac{|X \cap Y|}{|X| + |Y|} \quad , \quad (6.9)$$

where X and Y present the two segmentations, and $|\cdot|$ denotes the number of voxels inside the segmentation.

Additionally, we used mean surface distance in 3D (MSD) as the second evaluation metric. In formula, MSD is defined as:

$$\text{MSD}(X, Y) = \frac{1}{(n_X + n_Y)} \left(\sum_{i=1}^{n_X} d_i + \sum_{j=1}^{n_Y} d_j \right) \quad , \quad (6.10)$$

where n_X and n_Y represent the number of voxels on the two segmentation surfaces correspondingly, and d_i , d_j are the closest distances from each voxel on the surface to the other surface. An MSD of 0 implies that the boundaries of the two segmentations perfectly match.

Both Dice and MSD, though commonly used for evaluation of registration, do not quantify the actual registration accuracy inside the liver. Therefore, we additionally used landmark distances at vessels and vessel bifurcations as a third evaluation criterion of the registration accuracy. For each image pair, three experts annotated 15-20 sets of corresponding landmarks. After registration, the mean corresponding distance (MCD) between transformed points to the pre-interventional image and the corresponding points in the same image is calculated as follows:

$$\text{MCD}(A, B) = \frac{1}{n} \left(\sum_{i=1}^n |a_i - T(b_i)| \right) \quad , \quad (6.11)$$

where n is number of pairs of landmarks; a_i and b_i denote corresponding landmarks in the pre-interventional image A and post-interventional image B ; T represents the transformation from image B to image A [144]. Note that in our registration, the image A deforms to align on the image B but the landmarks in the post-image space (the fixed image B) transform into the pre-image space (the moving image A).

In order to evaluate the registration accuracy around the tumor area, we dilate the transformed tumor with a kernel of $[30 \ 30 \ 1]$ times the voxel size to create a local region of interest R . Because in most cases, there are insufficient anatomical landmarks close to the tumor, we propose to use local MSD (LMSD) to evaluate registration accuracy near the tumor. The intersection of the region of interest R



Figure 6.4. Manual liver segmentation and the landmarks inside the liver are used in DICE, MCD, MSD and LMSD evaluation. The overlaid tumor (pink) on the post-image is dilated to determine the local region of interest R (yellow).

with the liver boundary segmentation is subsequently used to determine the local MSD (see Fig. 6.4).

6.3.5 Training stage

The aim of the training stage is to determine the optimal grid size for the B-spline control points in elastix. In this stage, ten out of the 38 datasets were randomly selected. The registration was trained with varying grid size. We used Dice coefficient as the evaluation criteria to measure the accuracy of the registration.

From the boxplot in Fig. 6.5a, it can be seen that the optimal grid size range is from 5 mm to 12 mm. To determine the best grid size, we in this range computed Jacobian determinant of the transformation within the tumor areas. For the local rigid area, the Jacobian determinant should be 1 inside the area. Based on this analysis, we selected a grid size of 5 mm as the optimal setting because the Jacobian determinant of the transformation at tumor area is close to 1 (1.03 ± 0.05), indicating that the deformation is almost volume preservation with this setting.

We investigate the effect of changing the value of α and β in Equation 6.8 on registration accuracy using the local MSD metric. From Fig. 6.6 we can see that the local mean surface distance does not depend on α while changing slightly w.r.t the value of β . The optimal value range of β is around 10, thus we chose $\beta = 10$ mm as a setting in the evaluation section.

Fig. 6.7 illustrates the effect of local rigidity term on the transformation. It is clear that the deformation field is non-rigid inside and near the tumor area in the non-regularized case (left). In contrast, the deformation field is almost rigid inside and near the tumor area while far from it, the deformation field is non-uniform in the constrained case (right).

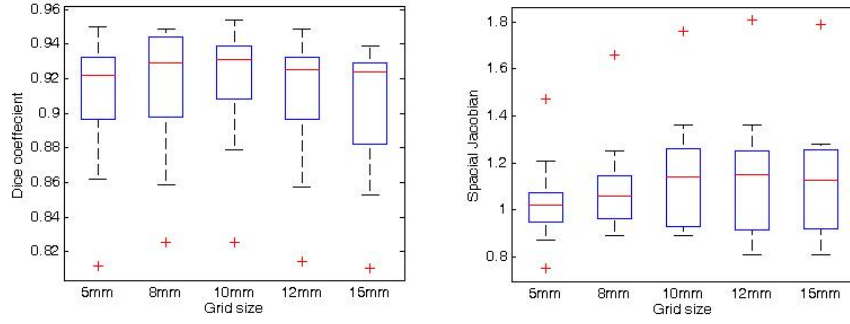


Figure 6.5. Box plots of Dice (left) and determinant of the Jacobian of the transformation (right) at the tumor area with respect to various grid sizes.

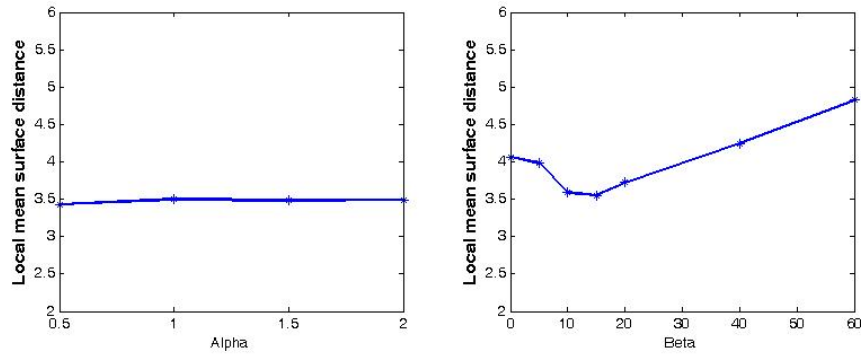


Figure 6.6. Accuracy of registration for various values of α and β .

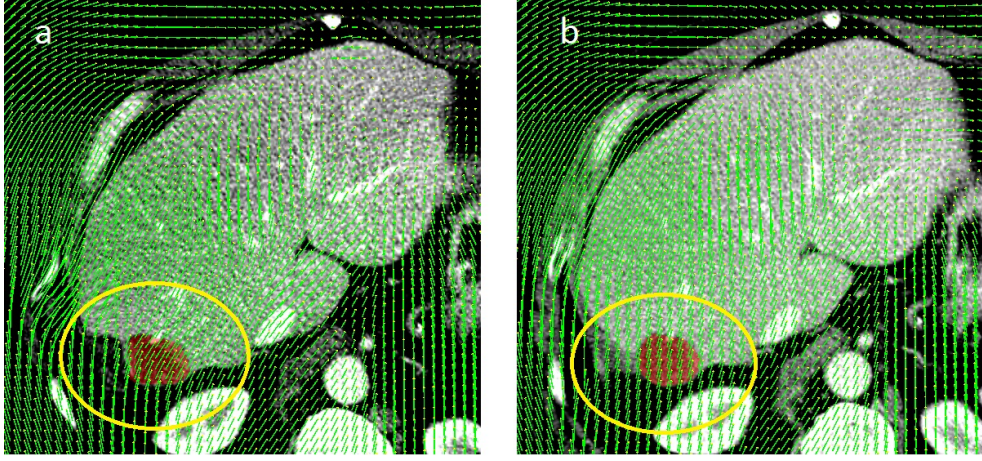


Figure 6.7. Non-rigid deformation fields and the tumor area overlaid on a transformed pre-interventional image. The left image shows the deformation field when not using the local rigid term (the determinant of the Jacobian of the deformation near the tumor deviates from 0.40 to 2.66); the right image shows the deformation field when using the local rigid term (the determinant of the Jacobian of the deformation near the tumor deviates from 0.92 to 1.12)

6.3.6 Results on test datasets

Using an initial B-spline grid size of 5 mm, $\alpha = 2$, $\beta = 10$ mm for the method described in section 6.2.2, we evaluate the registration method on the remaining 28 test datasets. Fig. 6.8 plots the result for each of the four metrics described in section 6.3.4

The rigid registration achieved a Dice coefficient of 87.9%, a mean distance of the liver surfaces of 5.53 mm, and a landmark error of 5.38 mm, while non-rigid registration with local rigid deformation resulted in a Dice coefficient of 92.2%, a mean distance between the liver segmentation boundaries of 2.54 mm and a landmark error of 2.91 mm. In addition, we also performed paired T-test to compare the accuracy of the rigid method and the proposed method. The p -values are smaller than 0.001 in all of the three evaluation metrics, indicating that the proposed method significantly improves the registration accuracy compared to rigid registration. The determinant of the Jacobian of the deformation at the tumor area is (1.03 ± 0.06) , indicating that only small volume shrinkage/expansion occurs.

The traditional non-rigid registration method without using the local rigidity term achieved an error of 4.57 mm for local MSD while the proposed registration method results in a local MSD of 3.83 mm. A paired T-test showed that this improvement is statistically significant ($p < 0.01$). The registration accuracy is also compared to other studies in the Discussion section 6.4.

Moreover, to investigate inter-observer agreement, we performed paired T-tests between the registrations accuracies using each observers landmarks. In our study, p -values of each pair of observers were 0.54, 0.62 and 0.69, suggesting that there is no significant difference between the observers.

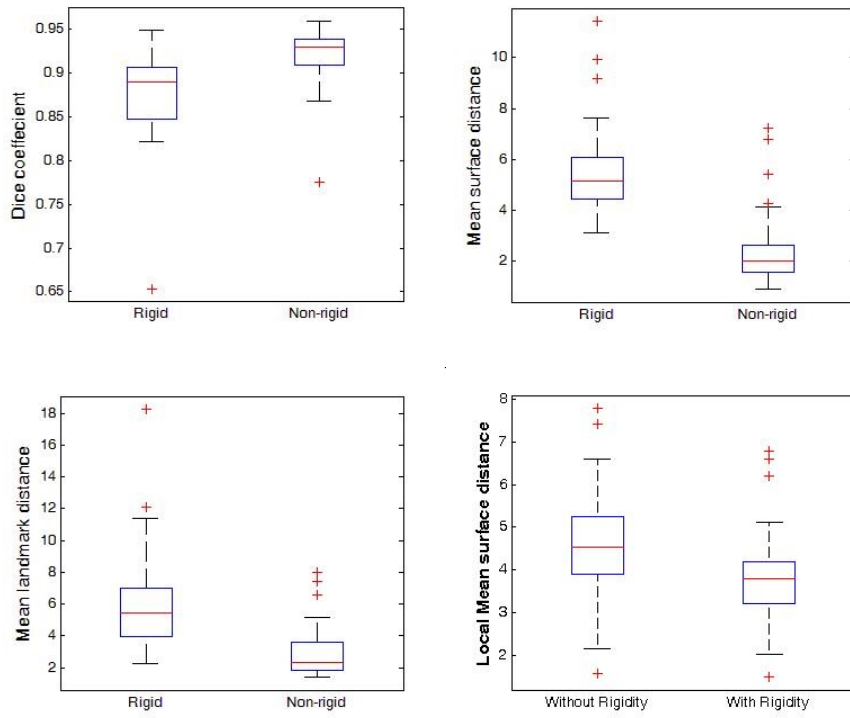


Figure 6.8. Boxplots of registration results, for rigid and non-rigid transformations: Dice of liver mask (top-left), mean surface distance of liver borders in mm (top-right), mean landmarks errors in mm (bottom-left), local mean surface distance in mm ((bottom-right)).

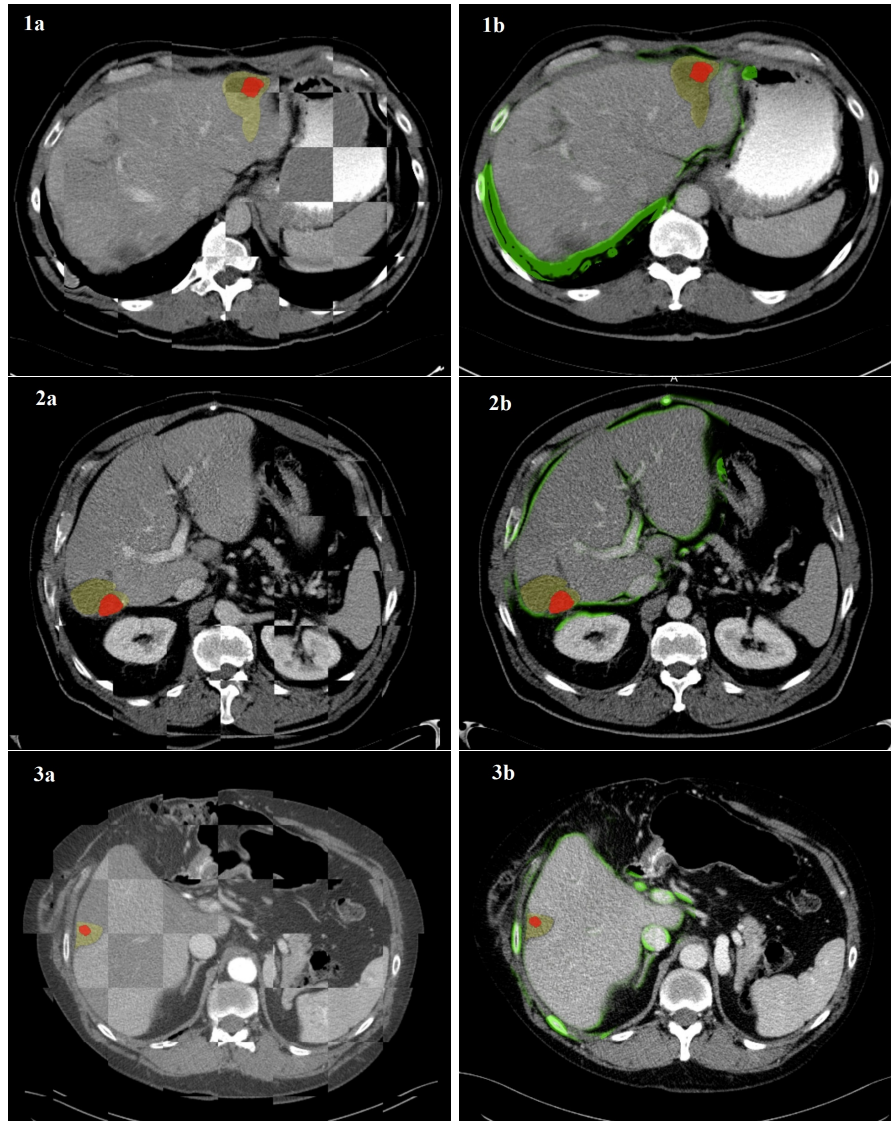


Figure 6.9. Three examples of the liver registration result. The left column contains checker board views of the aligned images. The right column shows overlays of edges of the transformed liver on the fixed image.

6.4 Discussion

In this work, we investigated a non-rigid registration method with pre-defined local rigid structure around the tumor for CT images of the liver for RFA interventions. The local rigid structure is constructed based on sigmoid function to ensure that the deformation field is rigid within, almost rigid nearby and non-rigid far from the tumor areas. The grid size of control point of B-spline was determined in the training stage using 10 datasets. From the training stage, we conclude that Dice coefficient is not affected much by the grid size and the Jacobian determinant of the deformation field changes significantly with changes in the grid size. Respecting Dice and volume conservation, we choose 5 mm as the initial grid size used for the evaluation.

Based on the result on the training datasets (see Fig. 6.6) we can conclude that registration accuracy is not sensitive to the value of α and β . However when the value of β is too low, the local rigid area is narrowed leading to more freedom in deformation nearby the tumor area while registration with the too high value of β makes the deformation become globally rigid-like registration in a large areas.

The method was evaluated on the remaining 28 clinical datasets using four different metrics: Dice, mean surface distance, distance between corresponding landmarks and local mean surface distance. The result is compared with rigid registration method and traditional nonrigid registration method (see Fig. 6.8). All of the cases were successfully registered based on visual assessment within running-time from 4 to 5 minutes. The results show that the proposed method achieved better registration accuracy compared to rigid registration and traditional nonrigid registration, while not deforming the tumor areas.

Registration accuracy, as evaluated with our method, depends on voxel size and slice spacing. As the CT data is anisotropic, we further investigated the effect of large slice spacing on our evaluation metric using landmark distances. Datasets with 2 - 3 mm spacing resulted in an accuracy in the range of 1.2 - 3.8 mm while datasets with 5 mm spacing resulted in an accuracy in the range of 2.7 - 8.2 mm, and 28% of the datasets have errors larger than 5 mm. The increase in registration error is caused by two factors: the discretization of the manual annotation (landmarks are annotated on a slice) and the loss information of the image in the space. As the common safety margin for RFA treatment is 5 mm [140], accurate quantification for assessing treatment success requires datasets with high spatial resolution, and slice spacing less than 5 mm.

From the result of registration accuracy using local MSD, i.e. 3.86 mm with using rigidity term and 4.57 mm without using rigidity term, we conclude that nearby the tumor area and ablation zone, the registration archived less accuracy than other areas. Apparently, the combination of intensity and some shape changes around the tumor region are harder to align than the other regions. In addition, the the accuracy of manual liver segmentation at ablation zones may also affect the registration evaluation result because the liver boundary at ablation zones is generally less clear than in other regions. (see Fig 6.1).

In general, our work performs equally or better than other studies reported in the literature: Xie et al (2011) used bi-Thin Plate Spline to register six datasets and achieved a Dice of 93.6% and a mean surface distance of 2.5 mm while we obtained

a Dice of 92.3% and a mean surface distance is 2.54 mm. Note that our images have lower resolution than the datasets used in this study. Rieder et al (2012) performed a rigid registration method on 41 dataset with some manual interactions and achieved a mean surface distance of 2.29 mm. Without using landmarks, the accuracy is 5.46 mm which is less than the accuracy that we obtained (2.91 mm). To the best of our knowledge, the highest achieved accuracy of corresponding landmarks is 1.3 mm as reported in Kim (2011). However, the method in the study is not mentioned in detail, and thus these results are hard to reproduce.

There are some limitations to our study. First, we did not yet evaluate the success of the treatment based on quantifications using the pre- and post-image alignment and compare these to long-term outcomes. However, this study being focused on the development of a method for aligning these pre- and post-interventional images, paves the way for performing such studies; our method enables clinicians to investigate whether quantifications based on accurate alignment of the tumor and the ablation zone are predictive for short- and long-term outcome. Second, we only use data from a single hospital center with limited number of CT scanners. We are, however, confident that similar results will be obtained for other vendors, as CT image acquisition is well protocolized, and Hounsfield units present physical properties. Third, because there are no landmarks available within the tumor areas in the post-image, it is not possible to directly evaluate the accuracy of the alignments of the tumors.

In the future, we intend to assess the value of registering pre- and post-images and quantifying overlap of tumor and ablation zone, and distances between tumor border and ablation zone border, for determining RFA treatment success.

6.5 Conclusion

In conclusion, we have developed and evaluated an automatic registration approach for the alignment of pre- and post-interventional liver images. It is able to non-rigidly align the images while keeping the tumor as a local rigid deformation. The registration approach was evaluated and the accuracy obtained is sufficient for use in future studies investigating factors of RFA treatment success.

Summary and Future Perspectives

7.1 Summary

This thesis addressed image analysis of liver CT images, focused on improving guidance in minimally invasive liver procedures. We developed and evaluated approaches to improve image quality, and to perform fusion of pre-operative CT images to intra-operative CT images as well as post-operative CT images. This chapter summarizes the main contributions of our work and provides future perspectives.

In chapter 2, we developed a liver vessel segmentation method for contrast enhanced CT images acquired in the portal venous phase, and evaluated six well-known vesselness and diffusion filters using their impact on liver vessel segmentation as evaluation criterion. The liver vessel segmentation method is based on a region growing approach which is commonly used for vessel segmentation tasks. The results of the experiments demonstrated that a hybrid diffusion filter with continuous switch (HDGS) performs the best as a preprocessing for this liver vessel segmentation method. However, the performance of the filters depends on the size of the vessels. Diffusion filters work best for large vessels with high contrast while vesselness filters are better suited for small vessels with low contrast.

Integration of pre-operative information in interventions can be used to improve image guidance. Therefore, we investigated methods to align pre-operative CT images to intra-operative CT images, and we investigated to what extent such an alignment requires non-rigid deformations. In chapter 3, a two-stage registration approach was introduced for the alignment task. First, we non-rigidly registered the pre-operative image to the intra-operative image using a conventional registration method. For the cases with large liver deformation caused by patient rotation and deep inspiration, we developed a refined registration method in which a local rigidity term was used to eliminate unrealistic deformations. Second, the pre-operative image was registered to the current intra-operative image utilizing the initialization from the first step as well as the initialization from the rigid registration between the intra-operative images. With this approach, 87% of the cases were successfully registered with a DICE overlap of 90% and a mean distance between corresponding points (MCD) of 4.5 mm.

In chapter 4, we extended the method described in chapter 3 with a semi-automatic procedure to improve the registration between the pre-operative image and the intra-operative images. In this method a novel energy term was added to minimize the

misalignment at the liver edges. This was achieved by segmenting the liver in the pre-operative image, and annotating points on the liver border in the intra-operative image. The energy term to be optimized in the registration minimizes the Euclidean distance between the transformed annotated points and the liver border. This can be performed very efficiently by pre-computing a distance transform on the liver border of the pre-operative image. The results showed that all of the cases were successfully registered with a clear improvement in the accuracy, i.e. 92% in DICE and 2.5 mm in average surface distances (ASD) vs 91% in DICE and 4.6 mm in ASD.

Whereas our registration approach for pre-operative to intra-operative images uses a non-rigid deformation, multimodal image fusion systems used in percutaneous liver interventions (e.g. CT-ultrasound registration) often use rigid registration. To assess whether a non-rigid approach would be relevant for such systems, in chapter 5 we quantified the non-rigid components of the deformation from the pre-operative image to the intra-operative image. For these experiments, we used images acquired during ablation procedures, and registered the pre-operative image to the intra-operative image by using the registration method described in chapter 3. Subsequently, the non-rigid component of the liver deformations was computed. This was done for the whole liver, as well as for representative 3D US volumes, acquired inter-costally and sub-xiphoidally. We found that the non-rigid component could amount to 5-6 mm, with larger errors occurring when there were large differences in breathing state, or when the patient was rotated during the intervention.

In chapter 6 we investigated a registration method for aligning the pre-operative image and the post-operative image of the liver to support the quantitative assessment of ablation success in radiofrequency ablation (RFA). In this work, we non-rigidly registered the pre-operative image with the tumor segmentations to the post operative image with the ablation zones using a local rigidity term. The latter term prevents unreliable deformations nearby the tumors caused by intensity differences in the tumor region owing to the ablation procedure. Experiments showed that this term indeed resulted in significant accuracy improvement, by comparing to the case without the rigidity term. The method can potentially be used in studies investigating the relationship between tumor-ablation zone overlap and clinical outcome, as well as in quantitative evaluation of ablation success in clinical practice.

7.2 Future Perspectives

In chapter 3 and chapter 4, we mainly focused on developing registration methods for aligning the pre-operative CT image with the intra-operative CT image of the liver in order to improve image guidance during liver interventions. Though the current tool is already planned to be evaluated in a clinical study, there are still several directions for further work:

First, the computational time for the registration is currently several minutes, which may slightly prolong the procedure, as the clinician needs to wait for the registration to be finalized. Further speeding up the registration is relevant. A parallel programming version of *Elastix* was released recently, and that improves the registration speed on multi-core computers, which may lead to reduce computation times to

a few minutes. A registration algorithm implemented to run on the GPU may further reduce the overall computational time less than a minute.

Second, an important step towards clinical acceptance will be confirmation of the hypothesis that the fusion of the pre-operative CT with the intra-operative images by a computer is better than a radiologist. This could be investigated further, e.g. by comparing the mental mapping capabilities of an interventional radiologist with the results of a mapping computed from a registration algorithm.

Chapter 6 presented a tool for assessment of success of the liver RFA using the pre-operative image and post-operative image. The method was evaluated based on technical criteria on a limited dataset without clinical evaluation criteria. Evaluation on a larger set of images, and also relating various scores on the overlap between the tumor and ablation zone with outcome and recurrences of the tumor may reveal whether ablation is performed correctly, and whether there is room for improved ablations. In case there is a strong relation between overlap as computed with our approach and patient outcome, this tool may be used for early assessment of treatment success and decide on re-treatment in case of incomplete ablations.

The use of real-time ultrasound for guidance in minimally invasive percutaneous ablations is preferred over guidance with CT. As not all tumors show sufficient contrast in ultrasound images, image fusion approaches, integrating pre-operative CT to ultrasound, have been proposed. Current systems are tracker-based, using optical or EM tracking. This generally leads to inaccurate fusion of images. Image-based fusion, provided that it is fast enough, may provide better guidance. However, CT to ultrasound registration is a notably hard problem. The method for liver vessel segmentation described in chapter 2 can be used for image-based alignment registration of CT and US during the intervention. There are several reports on vessel-based alignment, but this is not a solved problem yet. A vessel-based registration of 3D US and 3D CT images may become an adequate solution for accurate CT-US fusion in minimally invasive liver interventions. Several deep learning approaches have been published for liver segmentation and liver tumor segmentation recently. In our framework, we have not developed such a method for liver segmentation. With the large database of CT image of the liver that we have, deep learning could be a promising approach for liver and liver tumor segmentation. This would be a valuable tool for our framework, e.g. for liver mask creation.

In summary, this thesis presented and evaluated methods for alignment pre-operative CT images with intra-operative and post-operative images for improving guidance in minimally invasive liver interventions. In addition, non-rigid liver deformation was quantified to assess errors in fusion imaging where a rigid alignment model was used. The approaches are ready for use in clinical practice, enabling studies on the added clinical value of these methods.

Bibliography

- [1] C. Couinaud, "The paracaval segments of the liver," *Journal of Hepato-Biliary-Pancreatic Surgery*, vol. 1, no. 2, pp. 145–151, Apr. 1994.
- [2] S. R. Z. Abdel-Misih and M. Bloomston, "Liver Anatomy," *The Surgical clinics of North America*, vol. 90, no. 4, pp. 643–653, Aug. 2010.
- [3] J. E. Skandalakis, L. J. Skandalakis, P. N. Skandalakis, and P. Mirilas, "Hepatic surgical anatomy," *Surgical Clinics of North America*, vol. 84, no. 2, pp. 413–435, Apr. 2004.
- [4] S. Favelier, T. Germain, P. Y. Genson, J. P. Cercueil, A. Denys, D. Kraus, and B. Guiu, "Anatomy of liver arteries for interventional radiology," *Diagnostic and Interventional Imaging*, vol. 96, no. 6, pp. 537–546, Jun. 2015.
- [5] G. J. Tortora and B. H. Derrickson, *Principles of Anatomy and Physiology*, 12th ed. Wiley, Apr. 2008.
- [6] D. Bliss, "Liver and nearby organs," 2001. [Online]. Available: https://commons.wikimedia.org/wiki/File:Liver_and_nearby_organs.jpg
- [7] DBCLS, "Liver segment classification by Couinaud." Nov. 2015. [Online]. Available: https://commons.wikimedia.org/wiki/File:Liver_04_Couinaud_classification_posterior_view.png
- [8] GBD 2013 Mortality and Causes of Death Collaborators, "Global, regional, and national age-sex specific all-cause and cause-specific mortality for 240 causes of death, 1990-2013: a systematic analysis for the Global Burden of Disease Study 2013," *Lancet (London, England)*, vol. 385, no. 9963, pp. 117–171, Jan. 2015.
- [9] W. Zhang and B. Sun, "Impact of age on the survival of patients with liver cancer: an analysis of 27,255 patients in the SEER database," *Oncotarget*, vol. 6, no. 2, pp. 633–641, Jan. 2015.
- [10] J. Ferlay, I. Soerjomataram, R. Dikshit, S. Eser, C. Mathers, M. Rebelo, D. M. Parkin, D. Forman, and F. Bray, "Cancer incidence and mortality worldwide: Sources, methods and major patterns in GLOBOCAN 2012," *International Journal of Cancer*, vol. 136, no. 5, pp. E359–E386, Mar. 2015.
- [11] "WHO | Cancer country profiles 2014." [Online]. Available: <http://www.who.int/cancer/country-profiles/en/>
- [12] "SOMATOM Definition Flash." [Online]. Available: <https://www.healthcare.siemens.com/computed-tomography/dual-source-ct/somatom-definition-flash>
- [13] R. W. Cootney, "Ultrasound Imaging: Principles and Applications in Rodent Research," *ILAR Journal*, vol. 42, no. 3, pp. 233–247, Jan. 2001.
- [14] E. K. Outwater, "Imaging of the liver for hepatocellular cancer," *Cancer Control: Journal of the Moffitt Cancer Center*, vol. 17, no. 2, pp. 72–82, Apr. 2010.
- [15] E. Quaia, F. Calliada, M. Bertolotto, S. Rossi, L. Garioni, L. Rosa, and R. Pozzi-Mucelli, "Characterization of Focal Liver Lesions with Contrast-specific US Modes and a Sulfur Hexafluoride-filled Microbubble Contrast Agent: Diagnostic Performance and Confidence," *Radiology*, vol. 232, no. 2, pp. 420–430, Aug. 2004.
- [16] M. Postema and O. H. Gilja, "Contrast-enhanced and targeted ultrasound," *World Journal of Gastroenterology : WJG*, vol. 17, no. 1, pp. 28–41, Jan. 2011.

- [17] N. Dilmen, "Medical ultrasound image." 2010. [Online]. Available: https://commons.wikimedia.org/wiki/File:Ultrasound_Scan_ND_1230124453_1251190.png
- [18] M. R. Oliva and S. Saini, "Liver cancer imaging: role of CT, MRI, US and PET," *Cancer Imaging*, vol. 4, no. Spec No A, pp. S42–S46, Apr. 2004.
- [19] H. Fang, Y.-L. Song, X.-S. Li, Y.-M. Bi, P. Wang, H.-X. Fan, L. M. Meng, and H.-X. Hu, "Right arm injection of contrast medium reduces venous artifacts in head and neck multislice spiral computed tomography angiography," *European Review for Medical and Pharmacological Sciences*, vol. 19, no. 24, pp. 4698–4702, Dec. 2015.
- [20] H. Lusic and M. W. Grinstaff, "X-Ray Computed Tomography Contrast Agents," *Chemical reviews*, vol. 113, no. 3, Mar. 2013.
- [21] T. Murakami, M. Okada, and T. Hyodo, "CT versus MR Imaging of Hepatocellular Carcinoma: Toward Improved Treatment Decisions," *Magnetic Resonance in Medical Sciences*, vol. 11, no. 2, pp. 75–81, 2012.
- [22] N. Albiin, "MRI of Focal Liver Lesions," *Current Medical Imaging Reviews*, vol. 8, no. 2, pp. 107–116, May 2012.
- [23] B. Blechacz and G. J. Gores, "PET scan for a hepatic Mass," *Hepatology (Baltimore, Md.)*, vol. 52, no. 6, pp. 2186–2191, Dec. 2010.
- [24] M. Tsurusaki, M. Okada, H. Kuroda, M. Matsuki, K. Ishii, and T. Murakami, "Clinical application of 18f-fluorodeoxyglucose positron emission tomography for assessment and evaluation after therapy for malignant hepatic tumor," *Journal of Gastroenterology*, vol. 49, no. 1, pp. 46–56, 2014.
- [25] F. Pons, M. Varela, and J. M. Llovet, "Staging systems in hepatocellular carcinoma," *HPB : The Official Journal of the International Hepato Pancreato Biliary Association*, vol. 7, no. 1, pp. 35–41, 2005.
- [26] L. Jianyong, Y. Lunan, W. Wentao, Z. Yong, L. Bo, W. Tianfu, X. Mingqing, and Y. Jiaying, "Barcelona Clinic Liver Cancer Stage B Hepatocellular Carcinoma," *Medicine*, vol. 93, no. 26, Dec. 2014.
- [27] J. M. Llovet, J. Fuster, and J. Bruix, "The Barcelona approach: Diagnosis, staging, and treatment of hepatocellular carcinoma," *Liver Transplantation*, vol. 10, no. S2, pp. S115–S120, Feb. 2004.
- [28] N. Nagasue, H. Yukaya, Y. Ogawa, H. Kohno, and T. Nakamura, "Human liver regeneration after major hepatic resection. A study of normal liver and livers with chronic hepatitis and cirrhosis," *Annals of Surgery*, vol. 206, no. 1, pp. 30–39, Jul. 1987.
- [29] S. A. Curley, P. Marra, K. Beaty, L. M. Ellis, J. N. Vauthey, E. K. Abdalla, C. Scaife, C. Raut, R. Wolff, H. Choi, E. Loyer, P. Vallone, F. Fiore, F. Scordino, V. De Rosa, R. Orlando, S. Pignata, B. Daniele, and F. Izzo, "Early and Late Complications After Radiofrequency Ablation of Malignant Liver Tumors in 608 Patients," *Annals of Surgery*, vol. 239, no. 4, pp. 450–458, Apr. 2004.
- [30] M. G. Lubner, C. L. Brace, T. J. Ziemlewicz, J. L. Hinshaw, and F. T. Lee, "Microwave Ablation of Hepatic Malignancy," *Seminars in Interventional Radiology*, vol. 30, no. 1, pp. 56–66, Mar. 2013.
- [31] L.-Z. Niu, J.-L. Li, and K.-C. Xu, "Percutaneous Cryoablation for Liver Cancer," *Journal of Clinical and Translational Hepatology*, vol. 2, no. 3, pp. 182–188, Sep. 2014.
- [32] "MIYABI Angio-CT." [Online]. Available: <https://www.healthcare.siemens.com/angio/artis-interventional-angiography-systems/miyabi>
- [33] P. M. Barman and G. L. Su, "Limitations of the barcelona clinic liver cancer staging system with a focus on transarterial chemoembolization as a key modality for treatment of hepatocellular carcinoma," *Clinical Liver Disease*, vol. 7, no. 2, pp. 32–35, Feb. 2016.
- [34] J. R. McCarley and M. C. Soulen, "Percutaneous Ablation of Hepatic Tumors," *Seminars in Interventional Radiology*, vol. 27, no. 3, pp. 255–260, Sep. 2010.

- [35] N. Najmaei, K. Mostafavi, S. Shahbazi, and M. Azizian, "Image-guided techniques in renal and hepatic interventions," *The International Journal of Medical Robotics and Computer Assisted Surgery*, vol. 9, no. 4, pp. 379–395, Dec. 2013.
- [36] J. Banerjee, C. Klink, E. D. Peters, W. J. Niessen, A. Moelker, and T. van Walsum, "Fast and robust 3d ultrasound registration Block and game theoretic matching," *Medical Image Analysis*, vol. 20, no. 1, pp. 173–183, Feb. 2015.
- [37] H. Ishizaka, S. Awata, H. Arai, S. Hirasawa, and A. Shimizu, "CT-guided radiofrequency liver tumour ablation: use of a two-step coaxial system with a fine guide needle wire unit for high-risk cases," *The British Journal of Radiology*, vol. 83, no. 996, pp. 1077–1079, Dec. 2010.
- [38] "Artis zee biplane eco." [Online]. Available: <https://www.healthcare.siemens.com/refurbished-systems-medical-imaging-and-therapy/ecoline-refurbished-systems/angiography-ecoline/artis-zee-biplane-eco>
- [39] P. Ambrosini, D. Ruijters, W. J. Niessen, A. Moelker, and T. van Walsum, "Continuous roadmapping in liver TACE procedures using 2d3d catheter-based registration," *International Journal of Computer Assisted Radiology and Surgery*, vol. 10, no. 9, pp. 1357–1370, 2015.
- [40] B. Selby, S. Walter, G. Sakas, D. Wikler, W. Groch, and U. Stilla, "Full Automatic X-Ray based Patient Positioning and Setup Verification in Practice: Accomplishments and Limitations," 2010, p. 36.
- [41] D. Sahani, A. Mehta, M. Blake, S. Prasad, G. Harris, and S. Saini, "Preoperative hepatic vascular evaluation with CT and MR angiography: implications for surgery," *Radiographics: a review publication of the Radiological Society of North America, Inc*, vol. 24, no. 5, pp. 1367–1380, Oct. 2004.
- [42] W.-K. Lee, S. D. Chang, V. A. Duddalwar, J. M. Comin, W. Perera, W.-F. E. Lau, E. K. Bekhit, and O. F. Hennessy, "Imaging assessment of congenital and acquired abnormalities of the portal venous system," *Radiographics: a review publication of the Radiological Society of North America, Inc*, vol. 31, no. 4, pp. 905–926, Aug. 2011.
- [43] I. K. Tesdal, T. Filser, C. Weiss, E. Holm, C. Dueber, and W. Jaschke, "Transjugular Intrahepatic Portosystemic Shunts: Adjunctive Embolotherapy of Gastroesophageal Collateral Vessels in the Prevention of Variceal Rebleeding1," *Radiology*, vol. 236, no. 1, pp. 360–367, Jan. 2005.
- [44] S. Miyayama, O. Matsui, M. Yamashiro, Y. Ryu, H. Takata, T. Takeda, H. Aburano, and N. Shigenari, "Visualization of hepatic lymphatic vessels during transcatheter arterial chemoembolization for hepatocellular carcinoma," *Journal of Vascular and Interventional Radiology: JVIR*, vol. 18, no. 9, pp. 1111–1117, Sep. 2007.
- [45] C. Welp, S. Siebers, H. Ermert, and J. Werner, "Investigation of the influence of blood flow rate on large vessel cooling in hepatic radiofrequency ablation," *Biomedizinische Technik. Biomedical engineering*, vol. 51, no. 5-6, pp. 337–346, Dec. 2006.
- [46] H.-W. Huang, "Influence of blood vessel on the thermal lesion formation during radiofrequency ablation for liver tumors," *Medical Physics*, vol. 40, no. 7, p. 073303, Jul. 2013.
- [47] T. Lange, N. Papenberg, S. Heldmann, J. Modersitzki, B. Fischer, H. Lamecker, and P. M. Schlag, "3d ultrasound-CT registration of the liver using combined landmark-intensity information," *International Journal of Computer Assisted Radiology and Surgery*, vol. 4, no. 1, pp. 79–88, Jan. 2009.
- [48] M. Freiman, L. Joskowicz, and J. Sosna, "A variational method for vessels segmentation: algorithm and application to liver vessels visualization," in *SPIE*, vol. 7261, Feb. 2009, pp. 1–8.
- [49] S. Saini and D. Sahani, "Contrast techniques for hepatic multidetector CT angiography," *Applied Radiology*, vol. 32, no. 12, Dec. 2003.
- [50] P. Makowski and C. Sergio, "Review of vessel segmentation methods applied to liver volume images," in *Minimally invasive technologies and nanosystems for diagnosis and therapies*. Italy: Ist. Fisiologia Clinica, 2008, pp. 103–112.

- [51] D. Lesage, E. D. Angelini, I. Bloch, and G. Funka-Lea, "A review of 3d vessel lumen segmentation techniques: models, features and extraction schemes," *Medical Image Analysis*, vol. 13, no. 6, pp. 819–845, Dec. 2009.
- [52] D. Selle, B. Preim, A. Schenk, and H. O. Peitgen, "Analysis of vasculature for liver surgical planning," *IEEE Transactions on Medical Imaging*, vol. 21, no. 11, pp. 1344–1357, 2002.
- [53] B. Frericks, F. Caldarone, B. Nashan, D. Savellano, G. Stamm, T. Kirchhoff, H.-O. Shin, A. Schenk, D. Selle, W. Spindler, J. Klempnauer, H.-O. Peitgen, and M. Galanski, "3d CT modeling of hepatic vessel architecture and volume calculation in living donated liver transplantation," *European Radiology*, vol. 14, no. 2, pp. 326–333, Feb. 2004.
- [54] Q. Shang, L. Clements, R. L. Galloway, W. C. Chapman, and B. M. Dawant, "Adaptive directional region growing segmentation of the hepatic vasculature," in *SPIE*, vol. 6914, Mar. 2008, pp. 1–10.
- [55] O. Friman, M. Hindennach, C. Khnel, and H.-O. Peitgen, "Multiple hypothesis template tracking of small 3d vessel structures," *Medical image analysis*, vol. 14, no. 2, pp. 160–171, Apr. 2010.
- [56] A. Sboarina, R. I. Foroni, A. Minicozzi, L. Antiga, F. Lupidi, M. Longhi, M. Ganau, A. Nicolato, G. K. Ricciardi, A. Fenzi, M. Gerosa, A. De Simone, G. Fracastoro, A. Guglielmi, and C. Cordiano, "Software for hepatic vessel classification: feasibility study for virtual surgery," *International Journal of Computer Assisted Radiology and Surgery*, vol. 5, no. 1, pp. 39–48, Jan. 2010.
- [57] A. H. Foruzan, Y.-W. Chen, R. A. Zoroofi, and M. Kaibori, "Analysis of CT Images of Liver for Surgical Planning," *American Journal of Biomedical Engineering*, vol. 2, no. 2, pp. 23–28, Aug. 2012.
- [58] Y. Wang, B. Fang, J. Pi, L. Wu, P. S. P. Wang, and H. Wang, "Automatic Multi-Scale Segmentation of Intrahepatic Vessel in CT Images for Liver Surgery Planning," *International Journal of Pattern Recognition and Artificial Intelligence*, vol. 27, no. 01, p. 1357001, Jan. 2013.
- [59] Y. Shang, R. Deklerck, E. Nyssen, A. Markova, J. de Mey, X. Yang, and K. Sun, "Vascular Active Contour for Vessel Tree Segmentation," *IEEE Transactions on Biomedical Engineering*, vol. 58, no. 4, pp. 1023–1032, 2011.
- [60] M. Erdt, M. Raspe, and M. Suehling, "Automatic Hepatic Vessel Segmentation Using Graphics Hardware," in *Medical Imaging and Augmented Reality*, ser. Lecture Notes in Computer Science, T. Dohi, I. Sakuma, and H. Liao, Eds. Springer Berlin Heidelberg, Jan. 2008, no. 5128, pp. 403–412.
- [61] J. N. Kaftan, H. Tek, and T. Aach, "A two-stage approach for fully automatic segmentation of venous vascular structures in liver CT images," in *SPIE*, vol. 7259, Feb. 2009, pp. 1–12.
- [62] C. Bauer, T. Pock, E. Sorantin, H. Bischof, and R. Beichel, "Segmentation of interwoven 3d tubular tree structures utilizing shape priors and graph cuts," *Medical image analysis*, vol. 14, no. 2, pp. 172–184, Apr. 2010.
- [63] S. Esneault, C. Lafon, and J.-L. Dillenseger, "Liver vessels segmentation using a hybrid geometrical moments/graph cuts method," *IEEE Transactions on Bio-Medical Engineering*, vol. 57, no. 2, pp. 276–283, Feb. 2010.
- [64] V. Pamulapati, A. Venkatesan, B. J. Wood, and M. G. Linguraru, "Liver Segmental Anatomy and Analysis from Vessel and Tumor Segmentation via Optimized Graph Cuts," in *Abdominal Imaging. Computational and Clinical Applications*, ser. Lecture Notes in Computer Science, H. Yoshida, G. Sakas, and M. G. Linguraru, Eds. Springer Berlin Heidelberg, Jan. 2012, no. 7029, pp. 189–197.
- [65] P. Dokldal, C. Lohou, L. Perroton, and G. Bertrand, "Liver Blood Vessels Extraction by a 3-D Topological Approach," in *Medical Image Computing and Computer-Assisted Intervention MICCAI99*, ser. Lecture Notes in Computer Science, C. Taylor and A. Colchester, Eds. Springer Berlin Heidelberg, Jan. 1999, no. 1679, pp. 98–105.

- [66] L. Soler, H. Delingette, G. Malandain, J. Montagnat, N. Ayache, C. Koehl, O. Dourthe, B. Malassagne, M. Smith, D. Mutter, and J. Marescaux, "Fully automatic anatomical, pathological, and functional segmentation from CT scans for hepatic surgery," *Computer aided surgery: official journal of the International Society for Computer Aided Surgery*, vol. 6, no. 3, pp. 131–142, 2001.
- [67] R. Beichela, C. Jankoa, R. Zottera, B. Reitingera, E. Bornika, K. Palgyib, E. Sorantinc, G. Werkgartnerd, and H. Bischofa, "Liver Segment Approximation in CT Data for Surgical Resection Planning," in *SPIE*, vol. 5370, 2004, pp. 1–12.
- [68] S. Kawajiri, X. Zhou, X. Zhang, T. Hara, H. Fujita, R. Yokoyama, H. Kondo, M. Kanematsu, and H. Hoshi, "Automated segmentation of hepatic vessels in non-contrast X-ray CT images," *Radiological Physics and Technology*, vol. 1, no. 2, pp. 214–222, Jul. 2008.
- [69] J.-J. Seo and J.-W. Park, "Automatic Segmentation of Hepatic Vessels in Abdominal MDCT Image," in *Fourth International Conference on Computer Sciences and Convergence Information Technology, 2009. ICCIT '09*, 2009, pp. 420–424.
- [70] P. Bruyninckx, D. Loeckx, D. Vandermeulen, and P. Suetens, "Segmentation of liver portal veins by global optimization," in *SPIE*, Mar. 2010, pp. 1–12.
- [71] N. Shevchenko, B. Seidl, J. Schwaiger, M. Markert, and T. C. Lueth, "MiMed liver: a planning system for liver surgery," *Conference proceedings: Annual International Conference of the IEEE Engineering in Medicine and Biology Society. IEEE Engineering in Medicine and Biology Society. Conference*, vol. 2010, pp. 1882–1885, 2010.
- [72] C. J. Goch, X. Wang, H.-P. Meinzer, and I. Wegner, "Liver Vessel Segmentation Using Gradient Vector Flow," in *Bildverarbeitung fr die Medizin 2011*, ser. Informatik aktuell, H. Handels, J. Ehrhardt, T. M. Deserno, H.-P. Meinzer, and T. Tolxdorff, Eds. Springer Berlin Heidelberg, Jan. 2011, pp. 104–108.
- [73] D. A. Oliveira, R. Q. Feitosa, and M. M. Correia, "Segmentation of liver, its vessels and lesions from CT images for surgical planning," *BioMedical Engineering OnLine*, vol. 10, no. 1, p. 30, Apr. 2011.
- [74] K. Drechsler and C. Laura, "Comparison of vesselness functions for multiscale analysis of the liver vasculature," in *2010 10th IEEE International Conference on Information Technology and Applications in Biomedicine (ITAB)*, 2010, pp. 1–5.
- [75] H. M. Luu, A. Moelker, C. Klink, A. Mendrik, W. Niessen, and T. v. Walsum, "Evaluation of Diffusion Filters for 3d CTA Liver Vessel Enhancement," in *Abdominal Imaging. Computational and Clinical Applications*, ser. Lecture Notes in Computer Science, H. Yoshida, D. Hawkes, and M. W. Vannier, Eds. Springer Berlin Heidelberg, Jan. 2012, no. 7601, pp. 168–177.
- [76] P. Perona and J. Malik, "Scale-space and edge detection using anisotropic diffusion," *IEEE Transactions on Pattern Analysis and Machine Intelligence*, vol. 12, no. 7, pp. 629–639, 1990.
- [77] R. Manniesing, M. A. Viergever, and W. J. Niessen, "Vessel enhancing diffusion: A scale space representation of vessel structures," *Medical Image Analysis*, vol. 10, no. 6, pp. 815–825, Dec. 2006.
- [78] A. M. Mendrik, E.-J. Vonken, A. Rutten, M. A. Viergever, and B. van Ginneken, "Noise reduction in computed tomography scans using 3-d anisotropic hybrid diffusion with continuous switch," *IEEE transactions on medical imaging*, vol. 28, no. 10, pp. 1585–1594, Oct. 2009.
- [79] A. F. Frangi, W. J. Niessen, K. L. Vincken, and M. A. Viergever, "Multiscale vessel enhancement filtering," in *Medical Image Computing and Computer-Assisted Intervention MICCAI98*, ser. Lecture Notes in Computer Science, W. M. Wells, A. Colchester, and S. Delp, Eds. Springer Berlin Heidelberg, Jan. 1998, no. 1496, pp. 130–137.
- [80] Y. Sato, S. Nakajima, N. Shiraga, H. Atsumi, S. Yoshida, T. Koller, G. Gerig, and R. Kikinis, "Three-dimensional multi-scale line filter for segmentation and visualization of curvilinear structures in medical images," *Medical Image Analysis*, vol. 2, no. 2, pp. 143–168, Jun. 1998.
- [81] J. Weickert, *Anisotropic Diffusion in Image Processing*, ser. ECMI. Germany: B. G. Teubner (Stuttgart), 1998.

- [82] F. Catt, P.-L. Lions, J.-M. Morel, and T. Coll, "Image Selective Smoothing and Edge Detection by Nonlinear Diffusion," *Siam Journal on Numerical Analysis*, vol. 29, no. 1, 1992.
- [83] T. Heimann, B. van Ginneken, M. A. Styner, Y. Arzhaeva, V. Aurich, C. Bauer, A. Beck, C. Becker, R. Beichel, G. Bekes, F. Bello, G. Binnig, H. Bischof, A. Bornik, P. M. M. Cashman, Y. Chi, A. Cordova, B. M. Dawant, M. Fidrich, J. D. Furst, D. Furukawa, L. Grenacher, J. Hornegger, D. Kainmiller, R. I. Kitney, H. Kobatake, H. Lamecker, T. Lange, J. Lee, B. Lennon, R. Li, S. Li, H.-P. Meinzer, G. Nemeth, D. S. Raicu, A.-M. Rau, E. M. van Rikxoort, M. Rousson, L. Rusko, K. A. Saddi, G. Schmidt, D. Seghers, A. Shimizu, P. Slagmolen, E. Sorantin, G. Soza, R. Susomboon, J. M. Waite, A. Wimmer, and I. Wolf, "Comparison and evaluation of methods for liver segmentation from CT datasets," *IEEE Transactions on Medical Imaging*, vol. 28, no. 8, pp. 1251–1265, Aug. 2009.
- [84] R. Adams and L. Bischof, "Seeded region growing," *IEEE Transactions on Pattern Analysis and Machine Intelligence*, vol. 16, no. 6, pp. 641–647, 1994.
- [85] A. Enquobahrie, L. Ibanez, E. Bullitt, and S. Aylward, *Vessel Enhancing Diffusion Filter*, 2007.
- [86] A. Enquobahrie, H. Yang, and S. Aylward, *Implementation of local structure tensor and enhancement anisotropic diffusion filters in ITK*, Aug. 2010.
- [87] L. Antiga, *Generalizing vesselness with respect to dimensionality and shape*, Mar. 2007.
- [88] K. Hameeteman, M. Zuluaga, M. Freiman, L. Joskowicz, O. Cuisenaire, L. F. Valencia, M. Glsn, K. Krissian, J. Mille, W. Wong, M. Orkisz, H. Tek, M. H. Hoyos, F. Benmansour, A. Chung, S. Rozie, M. van Gils, L. van den Borne, J. Sosna, P. Berman, N. Cohen, P. Douek, I. Snchez, M. Aissat, M. Schaap, C. Metz, G. Krestin, A. van der Lugt, W. Niessen, and T. van Walsum, "Evaluation framework for carotid bifurcation lumen segmentation and stenosis grading," *Medical Image Analysis*, vol. 15, no. 4, pp. 477–488, Aug. 2011.
- [89] H. Kirisli, M. Schaap, C. Metz, A. Dharampal, W. Meijboom, S. Papadopoulou, A. Dedic, K. Nieman, M. de Graaf, M. Meijs, M. Cramer, A. Broersen, S. Cetin, A. Eslami, L. Flrez-Valencia, K. Lor, B. Matuszewski, I. Melki, B. Mohr, I. ksz, R. Shahzad, C. Wang, P. Kitslaar, G. Unal, A. Katouzian, M. Orkisz, C. Chen, F. Precioso, L. Najman, S. Masood, D. nay, L. van Vliet, R. Moreno, R. Goldenberg, E. Vuini, G. Krestin, W. Niessen, and T. van Walsum, "Standardized evaluation framework for evaluating coronary artery stenosis detection, stenosis quantification and lumen segmentation algorithms in computed tomography angiography," *Medical Image Analysis*, vol. 17, no. 8, pp. 859–876, Dec. 2013.
- [90] T. Alhonnoro, M. Pollari, M. Lilja, R. Flanagan, B. Kainz, J. Muehl, U. Mayrhauser, H. Portugaller, P. Stiegler, and K. Tscheliessnigg, "Vessel Segmentation for Ablation Treatment Planning and Simulation," in *Medical Image Computing and Computer-Assisted Intervention MICCAI 2010*, ser. Lecture Notes in Computer Science, T. Jiang, N. Navab, J. P. W. Pluim, and M. A. Viergever, Eds. Springer Berlin Heidelberg, Jan. 2010, no. 6361, pp. 45–52.
- [91] P. L. Pereira, "Actual role of radiofrequency ablation of liver metastases," *European Radiology*, vol. 17, no. 8, pp. 2062–2070, Aug. 2007.
- [92] S. F. Altekruse, K. A. McGlynn, and M. E. Reichman, "Hepatocellular carcinoma incidence, mortality, and survival trends in the United States from 1975 to 2005," *Journal of Clinical Oncology: Official Journal of the American Society of Clinical Oncology*, vol. 27, no. 9, pp. 1485–1491, Mar. 2009.
- [93] J. M. Llovet, "Updated treatment approach to hepatocellular carcinoma," *Journal of Gastroenterology*, vol. 40, no. 3, pp. 225–235, Mar. 2005.
- [94] S. Garrean, J. Hering, A. Saied, W. S. Helton, and N. J. Espat, "Radiofrequency ablation of primary and metastatic liver tumors: a critical review of the literature," *American Journal of Surgery*, vol. 195, no. 4, pp. 508–520, Apr. 2008.
- [95] H. Elhawary, S. Oguro, K. Tuncali, P. R. Morrison, S. Tatli, P. B. Shyn, S. G. Silverman, and N. Hata, "Multimodality non-rigid image registration for planning, targeting and monitoring during CT-guided percutaneous liver tumor cryoablation," *Academic Radiology*, vol. 17, no. 11, pp. 1334–1344, Nov. 2010.

- [96] A. Weihusen, F. Ritter, T. Krger, T. Preusser, S. Zidowitz, and H.-O. Peitgen, "Workflow oriented software support for image guided radiofrequency ablation of focal liver malignancies," vol. 6509, 2007, pp. 650 919–650 919–9.
- [97] K. W. Kim, J. M. Lee, E. Klotz, S. J. Kim, S. H. Kim, J. Y. Kim, J. K. Han, and B. I. Choi, "Safety margin assessment after radiofrequency ablation of the liver using registration of preprocedure and postprocedure CT images," *AJR. American journal of roentgenology*, vol. 196, no. 5, pp. W565–572, May 2011.
- [98] C. Rieder, A. Weihusen, C. Schumann, S. Zidowitz, and H.-O. Peitgen, "Visual Support for Interactive Post-Interventional Assessment of Radiofrequency Ablation Therapy," *Computer Graphics Forum*, vol. 29, no. 3, pp. 1093–1102, Jun. 2010.
- [99] N. Archip, S. Tatli, P. Morrison, F. Jolesz, S. K. Warfield, and S. Silverman, "Non-rigid registration of pre-procedural MR images with intra-procedural unenhanced CT images for improved targeting of tumors during liver radiofrequency ablations," *Medical image computing and computer-assisted intervention: MICCAI ... International Conference on Medical Image Computing and Computer-Assisted Intervention*, vol. 10, no. Pt 2, pp. 969–977, 2007.
- [100] D. Mattes, D. R. Haynor, H. Vesselle, T. K. Lewellen, and W. Eubank, "PET-CT image registration in the chest using free-form deformations," *IEEE transactions on medical imaging*, vol. 22, no. 1, pp. 120–128, Jan. 2003.
- [101] D. Rueckert, L. I. Sonoda, C. Hayes, D. L. Hill, M. O. Leach, and D. J. Hawkes, "Nonrigid registration using free-form deformations: application to breast MR images," *IEEE transactions on medical imaging*, vol. 18, no. 8, pp. 712–721, Aug. 1999.
- [102] C. Rieder, S. Wirtz, J. Strehlow, S. Zidowitz, P. Bruners, P. Isfort, A. H. Mahnken, and H.-O. Peitgen, "Automatic alignment of pre- and post-interventional liver CT images for assessment of radiofrequency ablation," vol. 8316, 2012, pp. 83 163E–83 163E–8.
- [103] T. Lange, S. Wrz, K. Rohr, and P. M. Schlag, "Experimental comparison of landmark-based methods for 3d elastic registration of pre- and postoperative liver CT data," vol. 7261, 2009, pp. 72 610M–72 610M–8.
- [104] Y. Xie, M. Chao, and G. Xiong, "Deformable image registration of liver with consideration of lung sliding motion," *Medical Physics*, vol. 38, no. 10, pp. 5351–5361, Oct. 2011.
- [105] S. Klein, M. Staring, K. Murphy, M. A. Viergever, and J. P. W. Pluim, "elastix: A Toolbox for Intensity-Based Medical Image Registration," *IEEE Transactions on Medical Imaging*, vol. 29, no. 1, pp. 196–205, Jan. 2010.
- [106] S. Klein, M. Staring, and J. P. W. Pluim, "Evaluation of optimization methods for nonrigid medical image registration using mutual information and B-splines," *IEEE transactions on image processing: a publication of the IEEE Signal Processing Society*, vol. 16, no. 12, pp. 2879–2890, Dec. 2007.
- [107] M. Staring, S. Klein, and J. P. W. Pluim, "A rigidity penalty term for nonrigid registration," *Medical Physics*, vol. 34, no. 11, pp. 4098–4108, Nov. 2007.
- [108] H. M. Luu, C. Klink, W. Niessen, A. Moelker, T. van Walsum, C. Klink, and A. Moelker, "An automatic registration method for pre- and post-interventional CT images for assessing treatment success in liver RFA treatment," *Medical Physics*, vol. 42, no. 9, pp. 5559–5567, Sep. 2015.
- [109] Y. Zhou, Y. Zhao, B. Li, D. Xu, Z. Yin, F. Xie, and J. Yang, "Meta-analysis of radiofrequency ablation versus hepatic resection for small hepatocellular carcinoma," *BMC Gastroenterology*, vol. 10, p. 78, 2010.
- [110] S. N. Goldberg, C. J. Grassi, J. F. Cardella, J. W. Charboneau, G. D. Dodd, D. E. Dupuy, D. A. Gervais, A. R. Gillams, R. A. Kane, F. T. Lee, T. Livraghi, J. McGahan, D. A. Phillips, H. Rhim, S. G. Silverman, L. Solbiati, T. J. Vogl, B. J. Wood, S. Vedantham, and D. Sacks, "Image-guided Tumor Ablation: Standardization of Terminology and Reporting Criteria," *Radiology*, vol. 235, no. 3, pp. 728–739, Jun. 2005.
- [111] K. Passera, S. Selvaggi, D. Scaramuzza, F. Garbagnati, D. Vergnaghi, and L. Mainardi, "Radiofrequency ablation of liver tumors: quantitative assessment of tumor coverage through CT image processing," *BMC medical imaging*, vol. 13, p. 3, Jan. 2013.

- [112] P. Thvenaz and M. Unser, "Optimization of mutual information for multiresolution image registration," *IEEE transactions on image processing: a publication of the IEEE Signal Processing Society*, vol. 9, no. 12, pp. 2083–2099, 2000.
- [113] P. F. Felzenszwalb and D. P. Huttenlocher, "Distance Transforms of Sampled Functions," *Theory of Computing*, vol. 8, pp. 415–428, Sep. 2012.
- [114] D. P. Shamonin, E. E. Bron, B. P. F. Lelieveldt, M. Smits, S. Klein, M. Staring, and Alzheimer's Disease Neuroimaging Initiative, "Fast parallel image registration on CPU and GPU for diagnostic classification of Alzheimer's disease," *Frontiers in Neuroinformatics*, vol. 7, p. 50, 2013.
- [115] H. Lester and S. R. Arridge, "A survey of hierarchical non-linear medical image registration," *Pattern Recognition*, vol. 32, no. 1, pp. 129–149, Jan. 1999.
- [116] S. Klein, J. P. W. Pluim, M. Staring, and M. A. Viergever, "Adaptive Stochastic Gradient Descent Optimisation for Image Registration," *International Journal of Computer Vision*, vol. 81, no. 3, p. 227, Mar. 2009.
- [117] M. Unser, A. Aldroubi, and M. Eden, "B-spline signal processing. I. Theory," *IEEE Transactions on Signal Processing*, vol. 41, no. 2, pp. 821–833, Feb. 1993.
- [118] K. Mori, K. Fukuda, H. Asaoka, T. Ueda, A. Kunimatsu, Y. Okamoto, K. Nasu, K. Fukunaga, Y. Morishita, and M. Minami, "Radiofrequency Ablation of the Liver: Determination of Ablative Margin at MR Imaging with Impaired Clearance of Ferucarbotran Feasibility Study," *Radiology*, vol. 251, no. 2, pp. 557–565, May 2009.
- [119] T. Livraghi, L. Solbiati, M. F. Meloni, G. S. Gazelle, E. F. Halpern, and S. N. Goldberg, "Treatment of Focal Liver Tumors with Percutaneous Radio-frequency Ablation: Complications Encountered in a Multicenter Study," *Radiology*, vol. 226, no. 2, pp. 441–451, Feb. 2003.
- [120] L. Solbiati, T. Ierace, M. Tonolini, and L. Cova, "Guidance and monitoring of radiofrequency liver tumor ablation with contrast-enhanced ultrasound," *European Journal of Radiology*, vol. 51 Suppl, pp. S19–23, Jun. 2004.
- [121] L. Crocetti, R. Lencioni, S. Debeni, T. C. See, C. D. Pina, and C. Bartolozzi, "Targeting liver lesions for radiofrequency ablation: an experimental feasibility study using a CT-US fusion imaging system," *Investigative Radiology*, vol. 43, no. 1, pp. 33–39, Jan. 2008.
- [122] G. Mauri, L. Cova, S. D. Beni, T. Ierace, T. Tondolo, A. Cerri, S. N. Goldberg, and L. Solbiati, "Real-Time US-CT/MRI Image Fusion for Guidance of Thermal Ablation of Liver Tumors Undetectable with US: Results in 295 Cases," *CardioVascular and Interventional Radiology*, vol. 38, no. 1, pp. 143–151, Feb. 2015.
- [123] W. H. Nam, D.-G. Kang, D. Lee, J. Y. Lee, and J. B. Ra, "Automatic registration between 3d intra-operative ultrasound and pre-operative CT images of the liver based on robust edge matching," *Physics in Medicine and Biology*, vol. 57, no. 1, p. 69, 2012.
- [124] D. Lee, W. H. Nam, J. Y. Lee, and J. B. Ra, "Non-rigid registration between 3d ultrasound and CT images of the liver based on intensity and gradient information," *Physics in Medicine and Biology*, vol. 56, no. 1, p. 117, 2011.
- [125] W. Wein, S. Brunke, A. Khamene, M. R. Callstrom, and N. Navab, "Automatic CT-ultrasound registration for diagnostic imaging and image-guided intervention," *Medical Image Analysis*, vol. 12, no. 5, pp. 577–585, Oct. 2008.
- [126] E. M. V. Osorio, M. S. Hoogeman, A. M. Romero, P. Wielopolski, A. Zolnay, and B. J. M. Heijmen, "Accurate CT/MR vessel-guided nonrigid registration of largely deformed livers," *Medical Physics*, vol. 39, no. 5, pp. 2463–2477, May 2012.
- [127] S. Vijayan, S. Klein, E. F. Hofstad, F. Lindseth, B. Ystgaard, and T. Lang, "Motion tracking in the liver: validation of a method based on 4d ultrasound using a nonrigid registration technique," *Medical Physics*, vol. 41, no. 8, p. 082903, Aug. 2014.
- [128] M. v. Siebenthal, G. Szekely, A. J. Lomax, and P. C. Cattin, "Systematic errors in respiratory gating due to intrafraction deformations of the liver," *Medical Physics*, vol. 34, no. 9, pp. 3620–3629, Sep. 2007.

- [129] T. Rohlfing, C. R. Maurer, W. G. O'Dell, and J. Zhong, "Modeling liver motion and deformation during the respiratory cycle using intensity-based nonrigid registration of gated MR images," *Medical Physics*, vol. 31, no. 3, pp. 427–432, Mar. 2004.
- [130] O. Heizmann, S. Zidowitz, H. Bourquain, S. Potthast, H.-O. Peitgen, D. Oertli, and C. Kettelhack, "Assessment of intraoperative liver deformation during hepatic resection: prospective clinical study," *World Journal of Surgery*, vol. 34, no. 8, pp. 1887–1893, Aug. 2010.
- [131] H. M. Luu, C. Klink, W. Niessen, A. Moelker, and T. v. Walsum, "Non-Rigid Registration of Liver CT Images for CT-Guided Ablation of Liver Tumors," *PLOS ONE*, vol. 11, no. 9, p. e0161600, Sep. 2016.
- [132] A. P. Zijdenbos, B. M. Dawant, R. A. Margolin, and A. C. Palmer, "Morphometric analysis of white matter lesions in MR images: method and validation," *IEEE transactions on medical imaging*, vol. 13, no. 4, pp. 716–724, 1994.
- [133] D. Mattes, D. R. Haynor, H. Vesselle, T. K. Lewellen, and W. Eubank, "PET-CT image registration in the chest using free-form deformations," *IEEE transactions on medical imaging*, vol. 22, no. 1, pp. 120–128, Jan. 2003.
- [134] P. Viola and W. M. Wells III, "Alignment by Maximization of Mutual Information," *International Journal of Computer Vision*, vol. 24, no. 2, pp. 137–154, Sep. 1997.
- [135] B. Fischer and J. Modersitzki, "A unified approach to fast image registration and a new curvature based registration technique," *Linear Algebra and its Applications*, vol. 380, pp. 107–124, Mar. 2004.
- [136] A. Sotiras, C. Davatzikos, and N. Paragios, "Deformable medical image registration: a survey," *IEEE transactions on medical imaging*, vol. 32, no. 7, pp. 1153–1190, Jul. 2013.
- [137] K. S. Arun, T. S. Huang, and S. D. Blostein, "Least-Squares Fitting of Two 3-D Point Sets," *IEEE Transactions on Pattern Analysis and Machine Intelligence*, vol. PAMI-9, no. 5, pp. 698–700, Sep. 1987.
- [138] R. Loffroy, "Interventional radiology for hepatocellular carcinoma," *Minerva Gastroenterologica E Dietologica*, vol. 57, no. 3, pp. 299–309, Sep. 2011.
- [139] G. G. Di Costanzo, R. Tortora, G. D'Adamo, M. De Luca, F. Lampasi, L. Addario, A. Galeota Lanza, F. P. Picciotto, M. T. Tartaglione, G. Cordone, M. Imparato, S. Mattera, and C. M. Pacella, "Radiofrequency ablation versus laser ablation for the treatment of small hepatocellular carcinoma in cirrhosis: a randomized trial," *Journal of Gastroenterology and Hepatology*, vol. 30, no. 3, pp. 559–565, Mar. 2015.
- [140] B. A. Seinstra, O. M. van Delden, K. J. van Erpecum, R. van Hillegersberg, W. P. T. M. Mali, and M. A. A. J. van den Bosch, "Minimally invasive image-guided therapy for inoperable hepatocellular carcinoma: What is the evidence today?" *Insights into Imaging*, vol. 1, no. 3, pp. 167–181, Jun. 2010.
- [141] Y. Xie, M. Chao, and G. Xiong, "Deformable image registration of liver with consideration of lung sliding motion," *Medical Physics*, vol. 38, no. 10, pp. 5351–5361, Oct. 2011.
- [142] G. Niculescu, D. J. Foran, and J. Noshier, "Non-rigid registration of the liver in consecutive CT studies for assessment of tumor response to radiofrequency ablation," *Conference proceedings: Annual International Conference of the IEEE Engineering in Medicine and Biology Society. IEEE Engineering in Medicine and Biology Society. Annual Conference*, vol. 2007, pp. 856–859, 2007.
- [143] P. Markelj, D. Tomaev, B. Likar, and F. Pernu, "A review of 3d/2d registration methods for image-guided interventions," *Medical Image Analysis*, vol. 16, no. 3, pp. 642–661, Apr. 2012.
- [144] K. Murphy, B. v. Ginneken, J. P. W. Pluim, S. Klein, and M. Staring, "Semi-automatic Reference Standard Construction for Quantitative Evaluation of Lung CT Registration," in *Medical Image Computing and Computer-Assisted Intervention MICCAI 2008*, ser. Lecture Notes in Computer Science, D. Metaxas, L. Axel, G. Fichtinger, and G. Szekely, Eds. Springer Berlin Heidelberg, Sep. 2008, pp. 1006–1013, doi: 10.1007/978-3-540-85990-1_121.

Samenvatting en toekomstperspectief

Samenvatting

Dit proefschrift beschrijft beeldverwerkingsmethoden voor CT beelden van de lever, gericht op het verbeteren van beeldgeleiding bij minimal invasieve lever interventies. We hebben methoden om de beeldkwaliteit te verbeteren ontwikkeld en gevalueerd, en methoden om pre-operatieve beelden te fuseren met intra-operatieve CT beelden en post-operatieve CT beelden. Dit hoofdstuk vat de belangrijkste bijdragen van ons werk samen en geeft een toekomstperspectief.

In hoofdstuk 2 hebben we een levervatsegmentatie method voor CT beelden met contrast middel ontwikkeld, en zes bekende filters voor vaten gevalueerd, waarbij we keken naar hun impact op de levervatsegmentatie. De levervatsegmentatie methode is gebaseerd op een gebiedsgroei aanpak die vaak gebruikt wordt voor vaatsegmentaties. De resultaten van de experimenten laten zien dat een hydride diffusie filter met continue schakel (HDCS) het beste presteert als voorbereiding voor levervatsegmentatie. Echter, het resultaat hangt af van de grootte van de vaten. Filters gebaseerd op diffusie werken het best voor grote vaten met veel contrast, terwijl filters voor vaten beter geschikt zijn voor kleine vaten met weinig contrast.

Integratie van pre-operatieve informatie tijdens interventies zou de beeldgeleiding kunnen verbeteren. Daarom hebben we methoden onderzocht die pre-operatieve CT beelden kunnen fuseren met intra-operatieve CT beelden, en we hebben onderzocht in hoeverre voor zon fusie niet-rigide vervormingen nodig zijn. In hoofdstuk 3 introduceerden we een twee-staps registratie methode voor de fusie. Eerst registreren we het pre-operatieve beeld naar het intra-operatieve beeld met een conventionele registratiemethode met niet-rigide vervormingen. Voor de gevallen met een grote vervorming van de lever, veroorzaakt doordat de patiënt gedraaid ligt of diep ademhaalt, hebben we een methode voor de verfijning van de registratie ontwikkeld, waarbij een onrealistische vervormingen werden voorkomen door het gebruik van een extra term die locale rigiditeit van het deformatieveld bevordert. Vervolgens wordt het pre-operatieve beeld geregistreerd aan het huidige intra-operatieve beeld, waarbij een combinatie van het resultaat van de eerste stap en een rigid registratie tussen de twee intra-operatieve beelden gebruikt wordt als startpunt van de registratie. Met deze methode kon 87% van de gevallen succesvol geregistreerd worden met een Dice overlap van 90% en een gemiddelde afstand tussen corresponderende punten van 4.5

mm.

In hoofdstuk 4 hebben we de method van hoofdstuk 3 uitgebreid met een semi-automatische method om de registratie te verbeteren. In deze method wordt een nieuwe energieterm toegevoegd die misregistratie op de rand van de lever kan minimaliseren. Dit werd bereikt door de lever in het pre-operatieve beeld te segmenteren, en punten op de rand van de lever aan te geven in het intra-operatieve beeld. Deze energieterm zorgt ervoor dat de Euclidische afstand tussen de aangegeven punten en de rand van de lever. Dit kan heel efficiënt gebeuren door van te voren een afstandstransformatie op de rand van de lever in het pre-operatieve beeld te bepalen. De resultaten laten zien dat alle gevallen met succes geregistreerd konden worden met een duidelijke verbetering in nauwkeurigheid, nl 92% in Dice en 2.5 mm in gemiddelde afstand tussen de oppervlakken tegenover 91% in Dice en 4.6 mm gemiddelde afstand tussen de oppervlakken.

Terwijl onze method voor registratie van pre-operatieve beelden naar intra-operatieve beelden een niet-rigide vervorming gebruikt, gebruiken de meeste multimodale beeldfusiesystemen voor percutane lever interventies (bijv. CT-echografie registratie) meestal een rigide transformatie. Om te bepalen of een niet-rigide aanpak relevant zou zijn voor zulke systemen, bepalen we in hoofdstuk 5 de mate van niet-rigide componenten in de deformatie van het pre-operatieve beeld naar het intra-operatieve beeld. Voor deze experimenten hebben we beelden gebruikt die verkregen zijn tijdens ablatie procedures, en hebben de pre-operatieve beelden geregistreerd naar de intra-operatieve beelden met de method van hoofdstuk 3. Vervolgens hebben we de niet-rigide component in deze deformaties bepaald, zowel voor de hele lever als voor representatieve 3D echografie beelden, die inter-costaal of sub-xiphoidaal opgenomen zijn. We vonden dat de niet-rigide component 5-6 mm kon bedragen, waarbij grotere componenten voorkwamen als er grote verschillen in de ademhaling waren, of als de patiënt gedraaid lag tijdens de interventie.

In hoofdstuk 6 hebben we een registratie method voor de fusie van pre-operatieve beelden en post-operatieve beelden onderzocht. Zo'n method zou gebruikt kunnen worden als kwantiatieve maat voor het success van een ablatie procedure. In dit hoofdstuk registreren we het pre-operatieve beeld, waar de tumor is aangegeven, en het post-operatieve beeld met het ablatiegebied. Om onbetrouwbare vervormingen rond de tumor te voorkomen, die veroorzaakt zouden kunnen worden door de verschillen in intensiteit, wordt gebruikt gemaakt van een term die lokale rigide transformaties bewerkstelligt. De method heeft potentie om gebruikt te worden om de relatie tussen overlap van tumor en ablatiegebied en het klinisch resultaat te onderzoeken, en vervolgens ook om ablatiesucces te kwantificeren.

Toekomstperspectief

In hoofdstuk 3 en 4 hebben we ons met name gericht op het ontwikkelen van registratiemethoden voor pre-operatieve CT beelden en intra-operatieve CT beelden, met als doel de beeldgeleiding bij lever interventies te verbeteren. De huidige technieken zullen binnenkort in een klinische studie gevalueerd worden, maar er zijn nog voldoende richtingen voor verder onderzoek:

Allereerst is de rekentijd voor de registratie momenteel een aantal minuten, wat in de praktijk de procedure zou kunnen verlengen, omdat er gewacht moet worden op het gereedkomen van de registratie. Een verdere versnelling van de registratie is dus relevant. Onlangs is er een versie van *Elastix* verschenen die parallelle berekeningen ondersteunt, en dat zou de rekentijd kunnen verminderen op computers met meerdere rekenkernen. De implementatie van een registratie algoritme op de grafische kaart zou de totale rekentijd verder kunnen reduceren tot minder dan een minuut.

Ten tweede, een belangrijke stap richting klinische acceptatie van onze methoden zou de bevestiging zijn van de hypothese dat de computer beter is dan een radioloog in de fusie van pre-operatieve CT beelden met intra-operatieve CT beelden. Dit zou onderzocht kunnen worden, bijv. door het bepalen hoe goed een radioloog die fusie kan doen, en dit te vergelijken met het resultaat van een registratie algoritme.

Hoofdstuk 6 presenteerde een gereedschap om het succes van ablaties in de lever te evalueren op basis van de registratie van pre-operatieve en post-operatieve beelden. De evaluatie van de methode was gebaseerd op technische criteria, op een beperkt aantal beelden. Evaluatie op een groter aantal beelden, en ook het relateren van verschillende maten voor overlap van de tumor en het ablatiegebied met de uitkomst voor de patiënt, en het terugkeren van de tumor, zou kunnen laten zien of een ablatie goed is uitgevoerd, en of er ruimte is om ablaties te verbeteren. Als er een sterke relatie bestaat tussen de overlap zoals die met de gepresenteerde methode wordt berekend, en uitkomst voor de patiënt, dan zou de methode gebruikt kunnen worden om snel inzicht te krijgen in het resultaat van de behandeling, en evt. snel over te gaan tot een nieuwe ablatie als de vorige incompleet was.

Het gebruik van real-time echografie voor beeldgeleiding in minimal invasieve percutane ablaties heeft de voorkeur over beeldgeleiding met CT. Omdat niet alle tumoren voldoende zichtbaar zijn in echografie beelden, zijn er systemen ontwikkeld die pre-operatieve CT beelden kunnen fuseren met real-time ultrasound beelden. De huidige systemen zijn meestal gebaseerd op het gebruik van positievolgsystemen, optisch of electro-magnetisch. Deze aanpak leidt in het algemeen tot onnauwkeurige fusie. Beeldgebaseerde fusie, als het snel genoeg is, zou betere beeldgeleiding kunnen geven. De registratie van CT beelden en echografie beelden, die nodig is voor de fusie, is echter een bekend, moeilijk op te lossen probleem. De methode voor levervatsegmentatie beschreven in hoofdstuk twee kan gebruikt worden voor beeldgebaseerde registratie van CT en echografiebeelden tijdens de interventie. Er zijn verschillende artikelen over vaatgebaseerde fusie. Een registratie gebaseerd op de vaten in de 3D echografie en 3D CT beelden zou een adequate oplossing kunnen zijn voor een nauwkeurige fusie van CT en echografie beelden in minimaal invasieve lever interventies.

Verskillende methoden voor lever en tumore segmentatie gebaseerd op neurale netwerken zijn onlangs gepubliceerd. In onze aanpak hebben we zulke methoden niet gebruikt. Met de grote aantal CT beelden van de lever die we gebruikt hebben, zouden dit soort technieken een veelbelovende aanpak kunnen zijn om de lever en de tumor te segmenteren. Dat zou een waardevolle aanvulling op ons werk zijn.

Samenvattend, hebben we methoden ontwikkeld en geëvalueerd voor de fusie van pre-operatieve CT beelden met intra-operatieve en post-operatieve beelden met als doel de beeldgeleiding bij minimaal invasieve lever interventies te verbeteren. Daar-

naast hebben we de niet-rigide vervorming van de lever gekwantificeerd, om te kunnen bepalen hoe groot de fouten kunnen zijn in een fusiesysteem wat gebaseerd is op rigide deformaties. De beschreven methoden zijn gereed voor gebruik in de klinische praktijk, en maken verder onderzoek naar de klinische toegevoegde waarde mogelijk.

PhD Portfolio

Research:

- PhD period: 2011-2016
- Departments of Radiology and Medical Informatics.
- ASCI research school.

In-Depth Courses:

- Frontend Vision and Multiscale Image Analysis, ASCI, 2011.
- Advanced Pattern Recognition, ASCI, 2012.
- Presentation course, Erasmus MC, 2012.
- Knowledge driven image segmentation, ASCI, 2012.
- Biomedical English Writing Course, Erasmus MC, 2013.
- C++ programming, BGR, 2014.
- A Programmer's Guide for Modern High- Performance Computing, ASCI, 2015.
- Research Integrity, Erasmus MC, 2015.

Summer schools:

- 10th IEEE EMBS International Summer School on Biomedical Imaging, Rennes (France), 2012.
- Modalities, Methodologies and Clinical Research, Biomedical Imaging Summer School, Paris (France), 2013

Conferences and workshops (attendance/presentation):

- Medical Image Computing and Computer-Assisted Intervention MICCAI, Nice, France, 2012, Workshop (Presentation).
- Dutch Biomedical Engineering conference (BME), Netherlands, 2013 and 2015 (Attendance).
- Medical Imaging Symposium for PhD students (MISP), Netherlands, 2011-2015 (Attendance).

Others:

- Presentations (3x) at the department seminar of the Biomedical Imaging Group Rotterdam, 2011-2014.
- Presentations (2x) at the Medical Informatics Research Lunch 2011-2015.
- Teaching: Bio-medical Image Processing course, Erasmus MC, 2013.
- Anatomy session, Erasmus MC, 2013.
- Attendance at Erasmus MC PhD Day 2012-2014.
- Reviewing for IEEE Transactions on Medical Imaging (TMI), International Journal of Computer Assisted Radiology and Surgery (IJCARS) and for Physica Medica: European Journal of Medical Physics (EJMP).

Publications

Publications in International Journals:

- **H.M. Luu**, C.S. Klink, A. Moelker, W.J. Niessen, and T van Walsum, "Quantitative evaluation of noise reduction and vesselness filters for liver vessel segmentation on abdominal CTA images", *Phys Med Biol*, vol. 60, no. 10, pp. 3905-26, Apr. 2015.
- **H.M. Luu**, C.S. Klink, W.J. Niessen and T. van Walsum, "An automatic registration method for Pre- and Post-Interventional CT images for assessing treatment success in liver RFA treatment", *Med Phys*, vol. 42, no. 9, pp. 5559-5567, Aug. 2015.
- **H.M. Luu**, C.S. Klink, W.J. Niessen, A. Moelker and T. van Walsum, "Non-rigid registration of liver CT images for CT-guided ablation of liver tumors", *Plos ONE*, vol 11, no 09, pp e0161600, Sep. 2016.
- **H.M. Luu**, A. Moelker, S. Klein, W.J. Niessen and T. van Walsum, "Quantification of non-rigid liver deformation in radiofrequency ablation interventions using image registration", submitted.

Publications in International Conference Proceedings:

- **H.M. Luu**, C.S. Klink, A. Moelker, W.J. Niessen and T. van Walsum, "Evaluation of Diffusion Filters for 3D CTA Liver Vessel Enhancement", *Abdominal Imaging. Computational and Clinical Applications. MICCAI 2012 workshop proceedings*, Oct. 2012.
- G. Gunay, **H.M. Luu**, W.J. Niessen, T. van Walsum and S. Klein, "Semi-automated registration of pre- and intra-operative liver CT for image-guided interventions", *proceeding of conference SPIE*, vol. 9784, no. 1 pp. 97841N-8, Mar. 2016.

Conference Abstracts:

- G. Gunay, **H.M. Luu**, T. van Walsum and S. Klein. "Semi-automated registration of pre- and intra-operative liver CT for image-guided interventions", *NVPHBV Fall meeting*, 2015.

Acknowledgments

First of all, I would like to thank my parents who endlessly support me for my whole study life. My father always encourages me to learn more and more. In addition, during my study in Netherlands, my parents helped me a lot to take care of my wife and my little daughter.

I would like to deeply thank my promoter and my supervisor Prof.Dr. Wiro Niessen and Dr. Theo van Walsum. Prof.Dr. Wiro Niessen did show to me many important ideas which significantly improved my work quality. Besides, he is not only active in academic but also is a friendly, sporty person as well as a businessman, guiding me how to be a balance person. I really admire you with all of my heart.

Dr. Theo van Walsum is one of the most important persons in my life. He not only supervised me how to do research, but also was my teacher in the daily life. He has helped me with all of the things since I set my first step in the Netherlands without any friend. Moreover, he always encourages me whenever I was lacking motivation during the long trip of study. I have best regards for you.

I would like to thank Dr. Adriaan Moelker for being my co-supervisor. I learnt a lot of medical knowledge from you which was very crucial for my work. I wish you success and happiness in your life.

I specially thank Dr. Stefan Klein for your instructions. Whenever I got stuck with *Elastix*, you were the person willing to explain all of the things in detail for me. I would like to thank Camiel for working with me. You are one of the most talented people that I ever worked with. Your knowledge in the medical field and programing are really impressive. Thank you Pierre for being my colleague, you helped me a lot with technical stuff and programming. Thanks Jyotirmoy for being a friendly colleague all the time, especially thanks for the meals. Thank you Nora, Roman, Guillaume, Valerio, Gerardo, Wei, Erwin, Coert, Hui, Hua, Edit, Cecile, who are IGI members. Thank you Dr. Adriënne Mendrik, and Gokhan for working with me. Thank you Jean-Marie, Wyke, Carolyn, Emilie, Rahil, Andres, Annegreet, Diego, Anna, Esben and other BIGR members, we really had a memorable time working together.

I would like to thank Petra and Desiree for your administrative support. Thank all of colleagues in Medical Informatics and Radiology, for the PhD dinner, lunches, parties and outing.

I would like to thank Vietnam Ministry of Education and Training (MOET), and Information Technology for European Advancement (ITEA) for supporting and funding for my research. Special thanks to Prof.Dr. Nguyen Phu Thuy, my former

supervisor in Vietnam, who died of liver cancer.

Most importantly, I would like to thank my wife Ram and my daughter Suri Hai Thu who are besides me and make my life wonderful and happy.

Luu Manh Ha
Rotterdam, December 2016

Curriculum Vitae

Luu Manh Ha was born in Hanoi in 1985. He completed his Bachelor program in Faculty of Electronics and Telecommunications, Vietnam National University, Hanoi in 2007. His final project is about signal processing of a navigation system. After that, he continued the work as a researcher and he received a MSc degree in Electronic Engineering from Vietnam National University, Hanoi in 2010

After the master study, he worked partly for an industrial company. His project mainly concerned signal processing and communication via GSM/GPRS network for a street lighting control and management system.

He worked from 2011 to 2016 as a Ph.D. student at the Biomedical Imaging Group Rotterdam, involved in the Image Guidance in Interventions research line. His study is to develop segmentation, registration and quantification methods to improve image guidance in interventions and assessment of liver cancer treatments.

